UC San Diego

UC San Diego Electronic Theses and Dissertations

Title

Design of Enabling Technologies for Soft Minimally Invasive Surgical Robots

Permalink

https://escholarship.org/uc/item/0m81w8h6

Author

Giri, Ayush

Publication Date

2024

Peer reviewed|Thesis/dissertation

eScholarship.org Powered by the California Digital Library
University of California

UNIVERSITY OF CALIFORNIA SAN DIEGO

Design of Enabling Technologies for Soft Minimally Invasive Surgical Robots

A dissertation submitted in partial satisfaction of the
requirements for the degree Doctor of Philosophy

in

Engineering Sciences (Mechanical Engineering)

by

Ayush Giri

Committee in charge:

Professor Tania K. Morimoto, Chair
Professor Shengqiang Cai
Professor Michael T. Tolley
Professor Michael Yip

2024

Copyright

Ayush Giri, 2024

All rights reserved.

The Dissertation of Ayush Giri is approved, and it is acceptable in quality and form for publication on microfilm and electronically.

University of California San Diego

2024

DEDICATION

Dedicated to Mummy, Buwa, and Aama

TABLE OF CONTENTS

Dissertation Approval Page iii

Dedication iv

Table of Contents v

List of Figures viii

List of Tables xi

Acknowledgements xii

Vita xiv

Abstract of the Dissertation xv

Chapter 1 Introduction 1
1.1 Motivation 2
1.2 Prior Work 3
1.2.1 Soft Robots for MIS 3
1.2.2 Tissue Manipulation Using Soft Robots 4
1.2.3 Simplified Control Hardware for Pneumatically Actuated Soft Robots . 5
1.2.4 Intuitive Input Interfaces for Soft Robots 7
1.3 Contributions 7
1.3.1 InchIGRAB: An Inchworm-Inspired Guided Retraction and Bending Device for Vine Robots during Colonoscopy 8
1.3.2 Modeling and Design of Soft, Positive-Pressure Actuated Suction Cups for Anchoring in Minimally Invasive Surgery 8
1.3.3 PneuSIC Box: Pneumatic Sequential and Independent Control Box for Scalable Demultiplexing 9
1.3.4 Hapstick: A Soft Flexible Joystick for Stiffness Rendering via Fiber Jamming 9
1.4 Dissertation Overview 9

Chapter 2 InchIGRAB: An Inchworm-Inspired Guided Retraction and Bending Device for Vine Robots during Colonoscopy 11
2.1 Introduction 12
2.1.1 Prior Work 12
2.1.2 Vine Robots 14
2.1.3 Contributions 15
2.2 Working Principle 15
2.2.1 Steering 16
2.2.2 Retraction 17

2.3 Design and Fabrication 18
2.3.1 Design Requirements 18
2.3.2 Bending/Elongating Module 19
2.3.3 Anchoring Module 22
2.3.4 Fabrication 23
2.3.5 InchIGRAB Assembly 24
2.3.6 Vine Robot 25
2.3.7 Pneumatic Control System 26
2.4 Device Characterization 27
2.4.1 Validation of the Bending/Elongating Model 27
2.4.2 Anchoring Module Characterization 27
2.4.3 Durability Characterization 30
2.5 Motion Characterization 31
2.5.1 Motion Characterization Setup and Procedure 31
2.5.2 Forward Motion 33
2.5.3 Retraction 35
2.6 Demonstration 36
2.7 Discussion 38
2.8 Acknowledgements 39

Chapter 3 Design of Soft, Positive-Pressure Actuated Suction Cups for Anchoring in Minimally Invasive Surgery 40
3.1 Introduction 41
3.1.1 Background 41
3.1.2 Previous Work 41
3.1.3 Contributions 43
3.2 Materials and Methods 43
3.2.1 Operating Mechanism 43
3.2.2 FEA Modeling 45
3.2.3 Design Parameters and Optimization Study 46
3.2.4 Fabrication 48
3.3 Results 49
3.3.1 Optimization Results 49
3.3.2 Model Validation on Rigid and Soft Substrates 51
3.3.3 Performance Evaluation With External Loads 54
3.3.4 In-Vivo Demonstration 55
3.4 Discussion 57
3.5 Acknowledgments 58

Chapter 4 PneuSIC Box: Pneumatic Sequential and Independent Control Box for Scalable Pneumatic Demultiplexing 59
4.1 Introduction 60
4.1.1 Background 60
4.1.2 Contributions 60

4.2 Working Principle 61
4.3 Design 63
4.4 FEA Model of Kink Valves 65
4.5 Experiments 67
4.5.1 Model Validation 67
4.5.2 Actuation Time 70
4.5.3 Pneumatic Memory Retention 72
4.6 Demonstrations 73
4.6.1 Inchworm Robot 74
4.6.2 Mock Hand for American Sign Language 75
4.7 Discussion 76
4.8 Acknowledgments 77

Chapter 5 Hapstick: A Soft Flexible Joystick for Stiffness Rendering via Fiber Jamming 78
5.1 Introduction 79
5.1.1 Background 79
5.1.2 Contributions 80
5.2 System Design 81
5.2.1 Working Principle 82
5.2.2 Design and Fabrication 82
5.2.3 System Workflow 83
5.3 Device Characterization 84
5.3.1 Effects of Fiber Number 85
5.3.2 Stiffness Characterization 88
5.4 Psychophysical Study and Stiffness Perception 89
5.4.1 Participants 89
5.4.2 Methods 89
5.4.3 Results and Discussion 91
5.5 Demonstrated Tumor Identification Task and Results 93
5.5.1 Setup 93
5.5.2 Procedure and Results 94
5.6 Discussion 96
5.7 Acknowledgements 97

Chapter 6 Conclusions 98
6.1 Summary 99
6.2 Future Work 100
6.3 Broader Impact 100

Bibliography 103

LIST OF FIGURES

Figure 1.1. Challenges hindering progress of soft robots for minimally invasive surgeries (MIS) 3

Figure 1.2. Schematic illustrating the robotic systems introduced in this dissertation within the workflow of soft robots for Minimally Invasive Surgery. 8

Figure 2.1. Rendering of the proposed system, showcasing the InchIGRAB within the vine robot as it performs steering and retraction through a curved colon. . 13

Figure 2.2. Schematic of the InchIGRAB within the vine robot during steering, forward motion, and retraction. 16

Figure 2.3. The bending/elongating module shown in a bent configuration, with parameters defining its configuration. 19

Figure 2.4. Process of fabricating a bending/elongating module 23

Figure 2.5. The fabrication process used for the anchoring modules 23

Figure 2.6. A fully assembled InchIGRAB 25

Figure 2.7. A schematic of the designed pneumatic control system 26

Figure 2.8. Experimental setup and results corresponding to the model validation study 28

Figure 2.9. Setups for characterizing slippage forces of actuators in an Anchoring Module at different pressures 29

Figure 2.10. Example of force versus deflection behavior during the vine tail and body slippage, with pressure vs mean slipping force for the anchoring module's actuators 30

Figure 2.11. The experimental setup used for motion characterization of the InchIGRAB enabled vine robot 32

Figure 2.12. Tracked vine robot's tip, the InchIGRAB's tip, and the commanded pressure inside the vine robot during forward motion and retraction 34

Figure 2.13. Still-frame images show the InchIGRAB and the vine robot successfully navigating a full mock colon environment, which features a 3D section. . 37

Figure 3.1. Schematic showing the cross-section of a positive-pressure actuated suction cup on rigid and soft substrate 41

Figure 3.2. Positive-pressure actuated suction cup before and after pneumatic load is applied to the pneumatic channel 44

Figure 3.3. Top view (top) and cross-sectional view (bottom) of a suction cup with its geometric parameters that were considered as design parameters for the FEA optimization study. 45

Figure 3.4. The process for fabricating a positive-pressure actuated suction cup 49

Figure 3.5. Results showing parameter dimensions and generated attachment force for 1008 designs at the pneumatic load of 16 kPa on a rigid substrate. . . . 50

Figure 3.6. Three representative behaviors observed for the studied suction cup designs at the selected pneumatic loads. 50

Figure 3.8. Suction cup behavior predicted by FEA simulations versus experimental results for (a) rigid and (b) soft substrates. 53

Figure 3.9. Experimental setup for measurement of maximum (a) normal forces and (b) shear forces that the suction cups can resist. 54

Figure 3.10. Results showing the maximum normal and shear forces resisted during each trial, along with the mean of these maximum forces 56

Figure 3.11. Results showing (a) normal forces and (b) shear forces the suction cup resisted on porcine tissues. 57

Figure 4.1. Working principle of PneuSIC Box 61

Figure 4.2. PneuSIC box with all of its components and supporting electronics 64

Figure 4.3. Proposed workflow for using the FEA model to predict the breakthrough pressure based on the kink angle for a given kink valve 65

Figure 4.4. Experimental setup for validating the FEA model 68

Figure 4.5. The mean and standard deviation of the time required for rotating the inner cylinder to align each of its columns with the kink valves and open them. 70

Figure 4.6. Experimental setup used for measuring PneuSIC Box's memory retention capabilities 71

Figure 4.7. Demonstration of PneuSIC Box controling an inchworm-inspired robot and a mock hand with soft fingers 72

Figure 5.1. Bidirectional control of a continuum robot using Hapstick 79

Figure 5.2. Hapstick's working principle 81

Figure 5.3. Schematic showing the workflow for teleoperating a robot and rendering stiffness feedback using Hapstick 83

Figure 5.4. Setup for characterizing Hapstick's force versus deflection behavior 85

Figure 5.5. Effect of number of fibers on Hapstick's stiffness and the relationship between vacuum load and average stiffness of the Hapstick 86

Figure 5.6. Representative psychometric curves obtained for one participant for movement in both the left and right directions. 90

Figure 5.7. Colorectal cancer screening demonstration with a tendon driven robot teleoperated using Hapstick 94

Figure 5.8. A representative trajectory of the tendon-driven robot's tip over one trial . 95

LIST OF TABLES

Table 3.1. Design parameters and their corresponding dimensions considered for the FEA optimization study. 47

Table 5.1. Summary of results obtained from the performed psychophysical study for a reference stimulus of 104.63 N/m. 92

ACKNOWLEDGEMENTS

I would first like to thank my committee members, Professor Tolley, Professor Yip, and Professor Cai, for their valuable suggestions, which have significantly strengthened this dissertation.

I owe special thanks to Professor Tolley, who first introduced me to UCSD and the field of robotics, during a summer research internship in my junior year. During the internship, Professor Tolley also connected me with Professor Morimoto, who later became my Ph.D. advisor.

I cannot thank Professor Morimoto enough. I couldn't have asked for a better advisor and mentor. Although I know I wasn't the easiest Ph.D. student to advise, she ensured I had everything needed to succeed both as a researcher and a Ph.D. student. Her kindness and work ethic will continue to inspire me throughout my career.

I would also like to thank my lab mates/friends. I've been incredibly fortunate to share the lab with such smart, hard-working people who also know how to have fun (and sing). My Ph.D. would have been much more difficult without the caring and friendly environment they provided.

I also owe deep thanks to my parents. The lessons I learned early in my childhood to strive for great things, despite limited resources, will continue to drive me forward, just as they did during my Ph.D.

Lastly, I am deeply grateful to my friends and family, who have supported me throughout my Ph.D.

Chapter 2 is, in part, a reprint of material from A. Giri, C. Girerd, J. Cervera-Torralba, M.T. Tolley, and T.K. Morimoto, *"InchIGRAB: An Inchworm-Inspired Guided Retraction and Bending Device for Vine Robots during Colonoscopy."* The material has been submitted for publication. The dissertation author is the primary author of this paper.

Chapter 3 is, in part, a reprint of material from A. Giri, C.Girerd, X. Luo, R. Broderick,

and T.K. Morimoto, *"Modeling and design of soft, positive-pressure actuated suction cups for anchoring in minimally invasive surgery." In 2022 9th IEEE RAS/EMBS International Conference for Biomedical Robotics and Biomechatronics (BioRob), pp. 01-08. IEEE, 2022.* The dissertation author is the primary author of this paper.

Chapter 4 is, in part, a reprint of material from A. Giri, A.Rivas, R. Yeerella, S. Cai, and T.K. Morimoto, *"PneuSIC Box: Pneumatic Sequential and Independent Control Box for Scalable Demultiplexing"* The material has been submitted for publication. The dissertation author is the primary author of this paper.

Chapter 5 is, in part, a reprint of material from A. Giri*, R. Bloom*, and T.K. Morimoto, *"Hapstick: A Soft Flexible Joystick for Stiffness Rendering via Fiber Jamming. IEEE Robotics and Automation Letters, 8(7), 4163-4170."* The dissertation author contributed equally to this paper, alongside R. Bloom.

VITA

2015-2019	Bachelor of Science in Mechanical Engineering, Howard University, Washington D.C.
2019-2021	Master of Science in Engineering Sciences (Mechanical Engineering), University of California San Diego
2019-2024	Doctor of Philosophy, University of California San Diego

ABSTRACT OF THE DISSERTATION

Design of Enabling Technologies for Soft Minimally Invasive Surgical Robots

by

Ayush Giri

Doctor of Philosophy in Engineering Sciences (Mechanical Engineering)

University of California San Diego, 2024

Professor Tania K. Morimoto, Chair

Soft robots have rapidly evolved over the past decade due to significant advancements in sensing, actuation, control, material science, and manufacturing methods. These developments, combined with the inherent ability of soft robots to safely conform to delicate environments, have made them promising for a wide range of applications, including minimally invasive surgeries (MIS). However, to fully realize the potential of soft robots as effective systems for surgical applications, there are several remaining challenges. First, soft robots must be designed to meet the clinical needs of the specific target procedure, while simultaneously offering significant improvements in safety. However, the compliance offered by soft robots can also cause them to become unstable during surgical tasks that place significant loads on the

robot's body. Second, highly deformable soft robots are less intuitive to control than rigid robots, complicating human-in-the-loop teleoperation for surgical applications. Finally, soft robots are generally pneumatically actuated to achieve the high forces and bandwidth needed for many surgical applications. However, this actuation method requires dedicated electromechanical components, such as pressure regulators, MOSFETs, and switches, for each actuator, making the system bulky, expensive, and limiting the robot's ability to operate untethered.

This dissertation presents several new robotic systems designed to address these challenges. First we introduce the InchIGRAB, a soft robot designed for colonoscopy. The InchIGRAB sits inside a vine robot (or growing robot) and is designed to enable navigation of the entire length of the colon during both forward motion and retraction, while minimizing interaction with the delicate colon environment. We also detail the design and modeling of soft, positive-pressure actuated suction cups for anchoring flexible and continuum robots during minimally invasive surgeries. Second, to enable intuitive control of soft and continuum robots, we present Hapstick, a soft, flexible joystick that can render stiffness information to users via fiber jamming. Hapstick was demonstrated as an input interface for teleoperating a continuum robot in colorectal cancer screening tasks. Finally, we present the PneuSIC Box, a pneumatic demultiplexer that enables independent control of multiple pneumatic actuators using a single pneumatic input and a motor. We demonstrated how PneuSIC Box could be used to provide independent control of actuators in an inchworm like robot, similar to the InchIGRAB, and a soft robotic hand. Overall, this dissertation presents several new robotic systems that advance the potential of soft robots for minimally invasive surgical applications.

Chapter 1

Introduction

1.1 Motivation

Soft robots are robotic devices made using soft materials [1], allowing them to safely conform to and interact with unknown and sensitive environments. Over the past decade, the field of soft robotics has seen significant developments in sensing [2, 3], actuation [4, 5, 6], control [7, 1, 8], material science [9, 10], and manufacturing [11, 12]. These developments have enabled soft robots for a wide range of applications, including space exploration [6], ocean research [13], search and rescue operations [14, 15], rehabilitation robotics [16, 17], and minimally invasive surgeries (MIS) [18, 19].

In MIS, advancements in soft robotics can potentially enable access to anatomies that are otherwise difficult to navigate with rigid robotic tools, while enhancing safety. Despite considerable research efforts dedicated to advancing soft robots for MIS [18, 19], several challenges must still be addressed to fully realize their potential for minimally invasive applications, as summarized in Fig. 1.1. First, the unique challenges and specific requirements presented by target anatomies and procedures highlight the need for novel soft robots. Soft robots specifically designed for target procedures have the potential to enhance safety for patients without sacrificing ease of use for the surgeons. Additionally, while the compliance and deformability of soft robots provide inherent safety, these characteristics also pose challenges in tasks requiring relatively large forces, such as tissue manipulation. To address this, additional mechanisms may be needed to securely anchor and stabilize the soft robots. Similarly, although soft robots are generally lightweight and compact, the control hardware required for their actuation can be bulky, expensive, and restrict these robots from being untethered. This complexity may hinder the adoption of soft robots for MIS. Finally, the large degrees of freedom offered by soft robots can make them unintuitive to operate with traditional rigid input interfaces. Moreover, haptic feedback can be essential for conveying critical information about the surgical environment to the surgeons [20]. Therefore, user interfaces must be designed to be intuitive while also providing haptic feedback to surgeons, ensuring the safe and efficient operation of soft robots

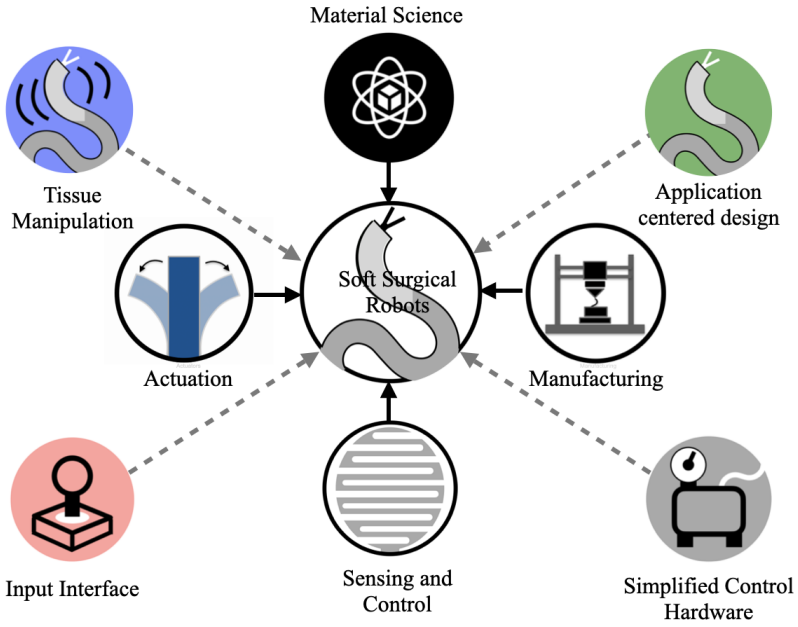


Figure 1.1. Significant advancements (solid dark arrows) in materials science, manufacturing, sensing and control, and actuation within the field of soft robotics has begun to enable the creation of soft surgical robots. However, several challenges hinder the progress of these robots for effective minimally invasive surgeries. These challenges (broken grey arrows) include 1) designing soft robots that align with anatomical and procedural needs, 2) developing simplified control hardware, 3) creating intuive input interfaces for controlling soft robots during MIS, and 4) enabling tissue manipulation with compliant robots.

during MIS.

1.2 Prior Work

1.2.1 Soft Robots for MIS

The potential of soft robots to safely interact with delicate anatomical environments has driven the development of novel soft robotic mechanisms for a wide range of surgical procedures. For instance, soft robots have been introduced for applications such as cardiothoracic endoscopy [21], organ retraction [22], breast cancer detection [23], lung cancer detection [24], neurosurgical brain retraction [25], and colonoscopy [26, 27]. However, with the rapid development of new technologies in soft robotics, and given the field's relative infancy, where soft robots have yet to be widely adopted in commercial MIS applications, there is a significant opportunity

to design systems that can further enhance patient safety and simplify use for surgeons.

For example, soft robots presented for colonoscopy [26, 27, 28, 29] have featured locomotion mechanisms and steering capabilities that take advantage of the inherent safety offered by the use of soft materials within the delicate colon environment, while minimizing interaction at the colon's curved sections. However, these soft robots have yet to address the challenge of minimizing shear forces, which can cause permanent damage to colon tissues [30], during their translation and interaction between their tethers and the surrounding environment. Additionally, significant improvements can be made to ensure higher levels of durability and reliability of soft robots [31], designed for enabling MIS applications, such as colonoscopy.

1.2.2 Tissue Manipulation Using Soft Robots

Soft robots are inherently safe to operate in surgical environments due to their compliance and deformability. However, these same properties can make them vulnerable to instability when large forces are applied at their distal end, such as during tissue manipulation tasks. To date, there have been several examples of devices that use soft structures to provide stability to surgical tools during MIS procedures [32, 33]. Soft structures offer advantages over their rigid counterparts due to their inherent safety and their ability to easily conform to the environment. Inflatable elastic balloons [34, 35] and inflatable soft linear actuators [32] are examples of soft structures that can provide stability to surgical devices in natural orifices by increasing contact area with the tubular environment when actuated. However, this method is limited to natural orifices like the esophagus and intestines. Furthermore, the delicate tissues in natural orifices cannot always endure large radial forces that are often applied using this method [36].

Soft suction cups are another example of a class of devices that can help stabilize tools during surgical procedures by anchoring to the surrounding tissue. Examples of such devices primarily operate by actively applying vacuum to the substrate through a vacuum channel [37, 38, 39]. This active suction risks the loss of CO_2 insufflation, which is commonly used in minimally invasive procedures to help expand the work-space and provide better visibility

to the surgeons [40, 41]

Soft positive pressure actuated suction cups [42], introduced by Tang et al. for their switchable climbing robots, provide advantages of no loss of insufflation, as well as no buckling problems during their actuation. This suction cup consists of a pneumatic channel embedded inside the main body and a cavity, or vacuum chamber, between the body and the substrate on which the suction cup is placed. When positive pneumatic load is applied in the channel through the air inlet, the channel inflates. The inflation causes the body of the suction cup to bend away from the substrate. The increase in volume in the vacuum chamber during the actuation results in a pressure difference in the region that leads to a suctioning effect. The mechanism exhibited by positive pressure suction cups makes it suitable for implementation in MIS procedures. However, more research is required for the design of effective suction cups that respect the needs and constraints posed by surgical applications. Moreover, there is also a need for computational models that can account for interaction of soft systems like positive pressure suction cups with not only rigid substrates, but also with soft tissues, to aid in the design process.

1.2.3 Simplified Control Hardware for Pneumatically Actuated Soft Robots

Soft robots can be actuated through various methods, including pneumatic [43], electric [44], magnetic [45], and thermal [46, 47] actuation. Despite these options, pneumatic actuation remains the preferred method due to its capability to deliver significant forces, high bandwidth, and support lightweight designs [48, 49, 50]. However, the need for a dedicated pressure regulator and associated electro-mechanical components [51] for each actuator makes the pneumatic control system bulky, expensive, and unsuitable for untethered applications. Several approaches have been proposed in the past to simplify the control hardware required for pneumatically actuated soft robots. One approach involves designing pneumatic circuits, valves, or robots that enable pre-programmed sequential control of actuators using just a single

pneumatic source. In [52], pre-programmed responses are achieved using a single pneumatic input by harnessing the viscous flow through tubes that connect the pneumatic actuators. This method requires specially designed actuators and tubing. Similarly, [53, 54, 55, 56] present electronics-free pneumatic circuits based on pneumatic ring oscillators that enable periodic actuation using a single, constant pressure source. The oscillating valves can also be combined to create control elements, such as pressure sensors and logic gates, enabling execution of a limited number of autonomous actuation sequences. Integrated electronics-free pneumatic controllers have enabled fully functioning 3D printed robotic systems in [57] and [58]. However, a common limitation across all approaches that enable pre-programmed sequential control is the inability to reprogram the soft robot during operation, which can present challenges in environments where control decisions must be made in real time.

To achieve full control of a soft robot, each of its actuators must be independently controllable at any time and at any pressure. Several fluidic demultiplexers, analogous to electrical demultiplexers, have been introduced to allow independent control of a large number of outputs using a small number of controlled inputs [59, 60, 61, 62, 63]. In [59] and [60], micro-fluidic valves are strategically arranged to enable the independent control of 2^{N-1} outputs with N controlled inputs. The primary limitations of these demultiplexers are their inability to simultaneously control multiple independent actuators, along with the restriction in flow rates due to their reliance on micro-fluidic channels and valves. In addition, in [59], actuators lose their pressurization states, if they are not being actively controlled. [63] presents a fluidic demultiplexing approach using reprogrammable intelligent metamaterial units, that also achieves control of 2^{N-1} outputs with N controlled inputs. However, achieving reprogrammable demultiplexing can require a large number of these metamaterial units, potentially compromising scalability. Alternatively, [62] introduces a fluidic matrix circuit inspired by electrical dot matrix displays, capable of controlling N^2 outputs with N controlled inputs. This fluidic matrix circuit allows actuation of any combination of outputs with considerably faster refresh rates. However, [62]

faces the same challenges due to the need for multiple controlled inputs, which increase with the number of outputs. Overall, previous pneumatic demultiplexers may still require numerous electro-mechanical components to achieve independent control of the actuators in a soft robot.

1.2.4 Intuitive Input Interfaces for Soft Robots

To date, the most common approach to control soft continuum robots, which are characterized by their long, slender and flexible structures, has been to use commercially available input devices, including gamepads, 3D mice, and 6-DOF input devices (e.g. Geomagic Touch) [64]. However, the mismatch between the kinematics of these input devices and those of soft continuum robots complicates their teleoperation [65, 66]. Recently, various input interfaces that are kinematically similar to continuum robots have started to be introduced as well. [67] presents a kinematically similar input leader device that allows intuitive shape control of multi-DOF continuum robots. Similarly, a flexible interface for teleoperating soft-growing robots is presented in [68]. The flexible device's design and structure offer "implicit" haptic feedback by rendering passive restoring spring forces to users. However, both [68] and [67] are unable to provide controllable haptic feedback, often critical for tasks such as tissue palpation and tissue identification. In [69], an impedance-type continuum input device that allows bidirectional teleoperation of continuum robots is presented. The device can provide force feedback via motors and cables to prevent users from commanding the robot to undesirable configurations. However, in order to provide feedback in multiple directions, the presented device requires a large, bulky setup with numerous motors, which increases the control complexity.

1.3 Contributions

This dissertation introduces four robotic systems and methods (summarized below and shown in Fig. 1.2) that have the potential to advance soft robots for minimally invasive surgical (MIS) applications.

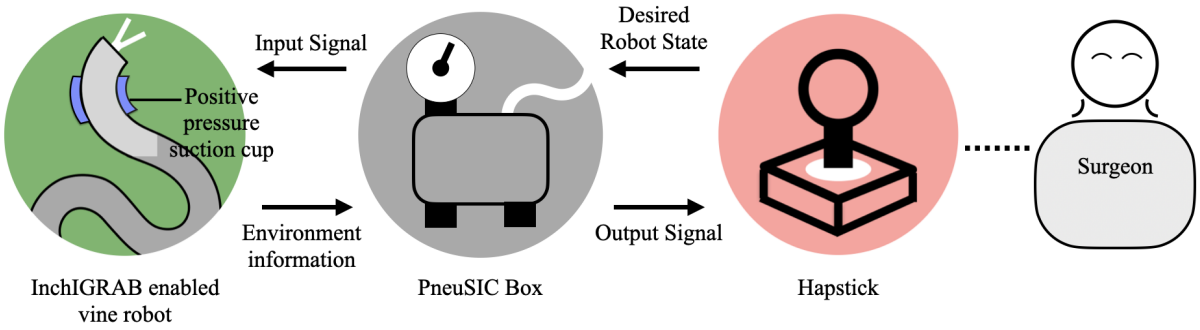


Figure 1.2. Schematic illustrating the robotic systems introduced in this dissertation in the context of a workflow for soft robots for minimally invasive surgery. Surgeons can use Hapstick to command soft and continuum robots, with feedback on the environment's stiffness provided via fiber jamming. The PneuSIC box supplies pressure signals to pneumatically driven surgical robots and/or input interfaces through a single controlled pneumatic input and motor. InchIGRAB enables vine robots for colonoscopy, minimizing their interaction with the sensitive colon environment. Lastly, positive-pressure suction cups help anchor soft continuum robots to the environment, stabilizing the robot during tissue manipulation tasks.

1.3.1 InchIGRAB: An Inchworm-Inspired Guided Retraction and Bending Device for Vine Robots during Colonoscopy

The InchIGRAB is a novel soft robot that is nested within a vine robot and allows for its localized bending, facilitating navigation around curved paths with minimal disturbance to the surrounding environment. Additionally, the InchIGRAB can translate along the vine robot's body in both straight and curved regions, enabling controlled retraction. Therefore, by enabling safe steering and retraction within the colon environment, the InchIGRAB allows vine robots, which exert minimal shear forces on their surroundings, to perform safe navigation for colonoscopies.

1.3.2 Modeling and Design of Soft, Positive-Pressure Actuated Suction Cups for Anchoring in Minimally Invasive Surgery

This work presents and experimentally validates a finite element model for simulating the behavior of positive-pressure actuated suction cups on both rigid and soft substrates. The model facilitates the design of an optimized positive-pressure suction cup capable of withstanding

large forces when attached to tissues during MIS. Consequently, these suction cup designs have the potential to anchor soft surgical tools securely to surrounding tissues during tasks such as tissue manipulation, thereby preventing instability and enhancing safety.

1.3.3 PneuSIC Box: Pneumatic Sequential and Independent Control Box for Scalable Demultiplexing

PneuSIC Box is a novel pneumatic demultiplexer inspired by the working principle of a music box. It allows independent control of a large number of actuators using just a single pneumatic input and a motor, significantly simplifying the back-end control system for pneumatic actuation. PneuSIC Box also enables simultaneous control of multiple actuators while supporting pneumatic memory retention, which allows actuators to maintain their pressurization states without additional energy.

1.3.4 Hapstick: A Soft Flexible Joystick for Stiffness Rendering via Fiber Jamming

Hapstick is the first fiber jamming-based input interface that provides tunable stiffness feedback to users. Along with the ability to deliver haptic feedback in any direction, the fiber jamming mechanism enables Hapstick to have a kinematically similar structure to continuum robots, potentially allowing for more intuitive control. Hapstick was also demonstrated to aid in the identification of tumor positions and their development stages during a mock colorectal cancer screening task. Overall, Hapstick highlights the potential of jamming-based mechanisms as novel input interfaces that offer effective haptic feedback during MIS applications.

1.4 Dissertation Overview

The dissertation is organized as follows: Chapter 1 provides an introduction, outlining the motivation for the research, a summary of existing work, and the contributions of the dissertation. Chapter 2 details the InchIGRAB, a soft robot designed to enable vine or growing

robots for safe colonoscopy. Chapter 3 focuses on the FEA modeling and design of soft suction cups used for anchoring flexible and soft robots during MIS applications. Chapter 4 introduces PneuSIC Box, a novel demultiplexer that enables control of multiple pneumatic outputs with a single pneumatic input and a motor. Chapter 5 presents an intuitive interface for controlling soft and continuum robots, demonstrating its application in colorectal cancer screening. Finally, Chapter 6 summarizes the dissertation and explores potential future work.

Chapter 2

InchIGRAB: An Inchworm-Inspired Guided Retraction and Bending Device for Vine Robots during Colonoscopy

2.1 Introduction

Flexible colonoscopy is recognized as the gold standard for screening colorectal cancer (CRC) [70], as nearly 60% of CRC-related deaths can be prevented with timely screening [70]. In the U.S. alone, millions of CRC procedures are performed annually [71], yet colonoscopy remains a highly skill-dependent procedure. Even when performed by an expert surgeon, the pushing action involved in advancing a colonoscope can induce large mechanical stresses on the delicate tissues, which can cause bleeding [72]. In some severe cases, mechanical trauma inflicted on the colon due to the colonoscope forming a loop instead of moving forward when pushed, may even result in perforations [70, 72]. In addition, the sigmoid colon has been observed to be susceptible to tissue damage or even perforations under large shear forces [30].

2.1.1 Prior Work

Sightline ColonoSight (CS) is an FDA approved colonoscope that features an alternative propulsion mechanism to a standard colonoscope. It consists of a sheath that unfurls from the tip when pressurized, to assist in propelling the colonoscope, thereby minimizing the required push-force for its advancement [73]. However, the system does not entirely eliminate the need for push forces and still results in shear forces along the colon wall, during its retraction. Double Balloon Colonoscopy (DBC) offers another alternative approach to standard colonoscopy. Balloons and overtubes in DBC can prevent the endoscope from looping by anchoring the distal section of the endoscope to the colon [74]. However, DBC requires significant training and expertise and is reserved for a small percentage of patients for whom conventional colonoscopy is not feasible [75]. Moreover, DBC also requires push forces at the base of the endoscope for its advancement, which can induce pain and discomfort in patients.

In contrast to flexible colonoscopes, wireless capsule endoscopes are commercially-available, pill-sized wireless screening tools that are passively propelled through the gastrointestinal tract by peristalsis [76]. Because they are not actively pushed through the colon, they

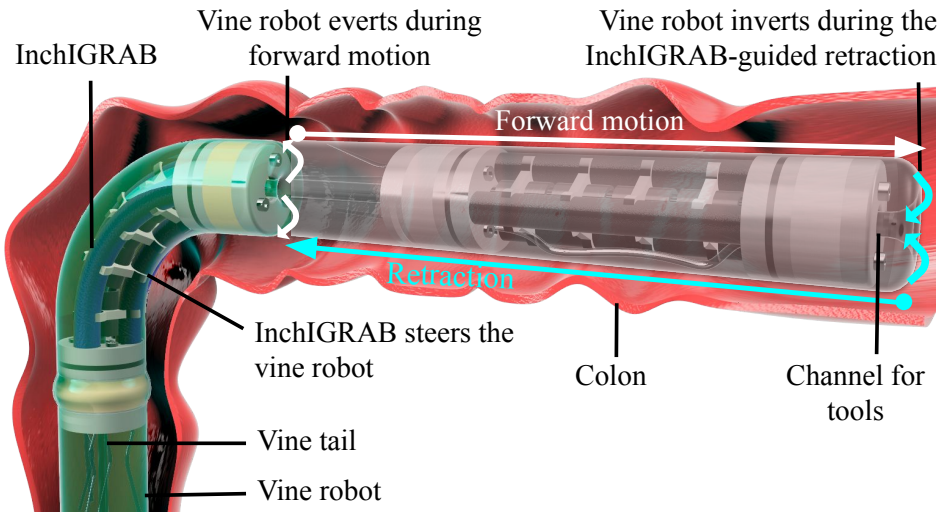


Figure 2.1. Rendering of our proposed system, which includes the InchIGRAB nested within a vine robot. The InchIGRAB facilitates steering of the vine robot through curved colon segments during forward movement and enables its controlled retraction.

pose a minimal risk of perforation. However, when using a capsule endoscope, the surgeon cannot control the position of the camera, and these procedures require a more aggressive preparation of the bowel [77]. Commercially available wireless capsule endoscopes are also unable to provide therapeutics or perform biopsies [78].

In addition to these commercial devices, there has been significant research on the development of alternative robotic colonoscopes that aim to improve controllability for surgeons and ensure safety for patients. As presented in [70], these research initiatives can broadly be categorized into three groups — electric, magnetic, and pneumatic — based on the actuation method. Both electrically driven [44] and magnetically driven [79, 80] colonoscopes exhibit impressive power-to-size ratios. However, they also have higher costs and power demands in comparison to their pneumatically driven counterparts. Pneumatically driven robots provide several major advantages for surgical applications due to their soft and lightweight body [26] that make them safe for operation in sensitive environments. Some examples of soft pneumatically driven robots for colonoscopy are presented in [26, 27].

2.1.2 Vine Robots

Vine robots, also known as growing or everting robots, are a type of soft robot that move through the environment by extending from the tip [81]. Vine robots are typically made from an inextensible, thin-walled tube, where the material from one end is inverted back inside the robot body. This inverted material, often called the "vine tail", everts out from the vine robot's tip when it is pressurized [81]. Unlike traditional push-instruments, whose entire body must translate to achieve forward motion, this method of movement results in no relative motion between the vine robot's body and the environment [81], enabling minimal shear forces. While these characteristics make vine robots well-suited for surgical applications like colonoscopy, there remain challenges with steering and retracting these robots in tortuous environments.

Active steering is important for enabling safe navigation of vine robots around tight turns to ensure that they will not get stuck or apply significant forces to the environment [82]. One method for active steering of vine robots, is to add pneumatic actuators — including series Pneumatic Artificial Muscles (sPAMs) [83], fabric Pneumatic Artificial Muscles (fPAMs) [84], or cylindrical Pneumatic Artificial Muscles (cPAMs) [85] — along the length of the robot. However, these pneumatic artificial muscles cause the entire robot body to bend with a constant curvature, which may not be desirable in sensitive environments. Although [85] presents a method using cPAMs that can offer localized steering, multiple actuators and magnetic valves are required along the entire length of the vine robot to do so. In [23], tendons are used to manipulate the vine robot. However, the large forces required to actuate the tendons from the base of the vine robot, lead to the need for incorporating an additional stiffening mechanism to prevent undesired buckling of the soft robot. Unlike other soft systems, [86] introduced a rigid joint with a motor capable of bending the local region of the vine robot around the joint. However, the presented steering mechanism cannot translate forward after acquiring a bent configuration, limiting its ability to steer the vine robot around multiple curvatures.

A vine robot must also be able to retract back in a safe and controlled manner. In [87],

a retraction method is presented in which the robot's tail is reeled at the base using a motor while maintaining some pressure inside the robot. However, such a retraction method can cause the vine robot to buckle in an uncontrollable configuration. Furthermore, a vine robot that has grown through a highly curved path faces a large capstan friction force [88] between its tail and body. Reeling the vine tail in this situation can damage the vine material or exert unintended forces on the delicate surrounding environment. Similarly, [89] proposes a retraction method involving sequentially pulling a semirigid backbone then the vine tail. The method also led to the buckling of the robot when retraction was carried out in curved states. [90] and [86] present retraction mechanisms driven by motors that can stay near the tip of the robot, preventing buckling. However, these mechanisms are difficult to scale down because of the presence of relatively large electro-mechanical components. Finally, [91] and [92] present retraction mechanisms that are fully soft, but they are designed only for retraction and would require additional actuators for steering the vine robot.

2.1.3 Contributions

We present a novel soft robotic system for colonoscopy that comprises an inchworm-inspired guided retraction and bending device, which we call the InchIGRAB, nested within a vine robot. The nested InchIGRAB provides localized bending of the vine robot, facilitating navigation around curved paths with minimal disturbance to the surrounding environment. The InchIGRAB can also translate along the body of the vine robot in both straight and curved regions, enabling controlled retraction of the vine robot. The proposed system, depicted in Fig. 2.1, has the potential to make colonoscopy procedures safer for patients and easier to perform for surgeons.

2.2 Working Principle

InchIGRAB is a tip-mounted soft robotic device that facilitates both steering and retraction of the vine robot during colonoscopy. It is pneumatically-actuated and sits inside the vine

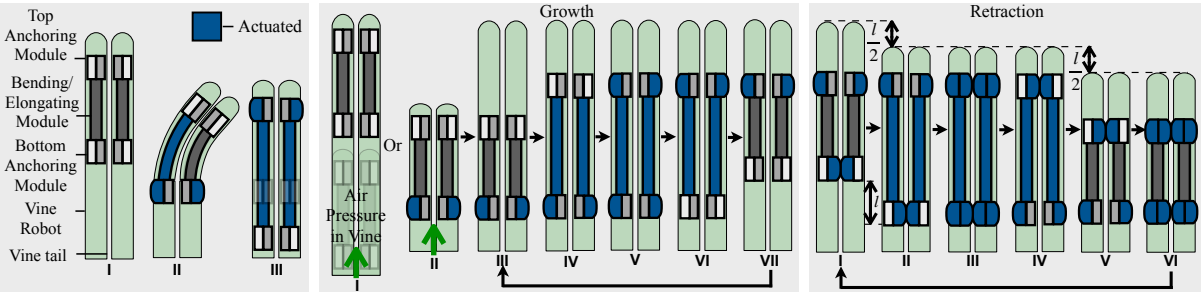


Figure 2.2. (a) Schematic of the system, which consists of the InchIGRAB positioned between the vine robot's body and the vine tail. The InchIGRAB itself has two anchoring modules and a bending/elongating module (I). The inner and the outer actuators of the anchoring modules can grasp the vine tail and vine robot's body, respectively, when actuated. The bending/elongating module comprises a set of linear actuators that enable steering when their relative pressures are controlled (II). The InchIGRAB's linear elongation is achieved when all actuators are pressurized equally (III). (b) Air pressure within the vine robot propels the InchIGRAB along with the vine robot's tip (I). Forward motion is also achieved by allowing the vine robot to evert, while the InchIGRAB performs inchworm-like motion to catch up (II-VII). (c) The InchIGRAB aids in the vine robot's retraction by pulling the vine tail backwards, while executing inchworm-like motion in the same direction.

robot, with the vine tail passing through the InchIGRAB's hollow channel (Fig. 2.2(a)-I). The InchIGRAB consists of two anchoring modules (top and bottom), which both consist of inner and outer expanding pneumatic actuators. When actuated, the inner actuator grasps the vine tail and the outer actuator grasps the vine body. Connecting the two anchoring modules is a bending/elongating module that consists of a set of three soft linear actuators. By controlling the relative pressures in these actuators, the tip-mounted InchIGRAB can steer the vine robot to a desired angle (Fig. 2.2(a)-II). Similarly, by applying equal pressures to all of the linear actuators, the InchIGRAB can linearly elongate either forwards or backwards (Fig. 2.2(a)-III). In this section, we explain the need for both active steering and retraction of the vine robot, along with the working principle of the InchIGRAB for achieving both tasks.

2.2.1 Steering

Without an active steering mechanism, a vine robot must rely on buckling due to its interaction with the environment in order to navigate around bends [82]. However, this method can lead to significant stresses on the colon wall, equal to the critical pressure required to induce

buckling in the vine robot [82]. In patients with diverticulitis, which has a reported incidence of approximately 17.5% in the general population [93], pressures exceeding 1.5 kPa on the inner colon wall can lead to permanent tissue damage [93]. Based on the equation for the critical force provided in [82], vine robots made from thermoplastic polyurethane (TPU) film (detailed in Section 2.3.6), exert stresses over 1.5 kPa when buckling at unsupported lengths shorter than 130 mm, conditions that can occur in curved colon sections. Therefore, vine robots must have the ability to steer at the tip to avoid directly pressing on the colon wall.

To move forward along curved paths, the InchIGRAB can first steer the vine robot to the required angle. Then, once the vine robot has grown around the curve, the InchIGRAB can perform inchworm-like motion by alternating elongation and anchoring actions until it reaches the vine robot's tip (Fig. 2.2(b)-III to Fig. 2.2(b)-VII). For forward motion along a straight path, sufficient pressure in the vine robot enables both itself and the InchIGRAB to move (Fig. 2.2(b)-I). The InchIGRAB translates due to the friction between the vine tail and the inside of the InchIGRAB's central hollow channel.

2.2.2 Retraction

Similarly, a vine robot must also be retracted safely and in a controlled manner during colonoscopy. Although the vine robot's tail could be spooled at the base to invert the material at the tip for retraction, in highly curved environments such as the colon, the interaction between the vine robot's tail and body can lead to significant capstan friction. Based on the analysis presented in [94], this force can cause the vine robot to buckle at the bent sections and at its base. This phenomenon was observed when retracting a standard vine robot through both a single curved section of a mock colon and along the entire mock-colon path, as seen in the supplemental video. Such buckling behavior can lead to uncontrollable retraction, excessive stress on the colon wall, and potential damage to the vine robot's material. Therefore, an alternative solution for the retraction of the vine robot is needed.

To retract the vine robot in a controlled manner without exerting shear forces on the

environment, the InchIGRAB moves backwards in an inchworm-like motion, while the inner actuators of the anchoring modules are actuated in a periodic sequence to pull the vine robot tail (Fig. 2.2(c)). During the elongation stage, the inner actuator of the bottom anchoring module grasps the vine tail, while the top anchoring module's outer actuator anchors the InchIGRAB, resulting in pulling of the vine tail in the backward direction (Fig. 2.2(c)-I and Fig. 2.2(c)-II). Subsequently, during the bending/elongating module's relaxation, the inner actuator of the top anchoring module grasps the vine tail, while the bottom anchoring module's outer actuator anchors to the vine robot's body, again pulling the vine tail in the backward direction (Fig. 2.2(c)-V). Because the vine tail moves twice as fast as the robot's tip [81], pulling the vine tail twice by a length l, retracts the tip by l. We note that the InchIGRAB's compliance allows it to adapt to the configuration of the surrounding vine robot, ensuring effective retraction in both straight and curved paths.

2.3 Design and Fabrication

In this section, we discuss the design and fabrication processes for creating all components of the presented robotic system, including the bending/elongating module, the anchoring modules, the vine robot, and the pneumatic control system.

2.3.1 Design Requirements

For an average adult, the smallest diameter of the human colon averages around 26 mm [95]. Therefore, to ensure successful deployment along the entire colon length, the InchIGRAB should not exceed 26 mm in diameter. In addition, a robotic colonoscope should be able to articulate or conform around acute bends, where the colon's centerline forms angles smaller than 90° [95], to ensure minimal interaction with the environment. The InchIGRAB should therefore be capable of obtaining an angle, shown as θ in Fig. 2.3, smaller than 90°.

2.3.2 Bending/Elongating Module

The bending/elongating module serves two purposes: (1) steering the vine robot and (2) translating the InchIGRAB, during both forward motion and retraction. The linear actuators in this module should therefore be capable of large length changes in order to facilitate both small angles for steering and more efficient translation. In addition, the linear actuators must provide a force greater than the force required for retraction, where $F_r = 0.5 P_{vine} A_{vine} + F_l$ [90]. P_{vine} and A_{vine} are the pressure inside the vine robot and the vine robot's cross sectional area, respectively. Similarly, F_l is the additional force required required to deform the material at the tip.

Inverse Pneumatic Artificial Muscles (IPAMs) are selected as the actuators for the bending/elongating module. IPAMs are soft, linear actuators that can achieve significant elongations even at small scales [96]. They consist of a soft rubber tube that is radially constrained using a material with high tensile strength [96]. IPAMs can also accommodate large pressures, which enables them to exert large forces, provided they are prevented from buckling. By arranging three IPAMs in a circular pattern, spaced 120° apart, the InchIGRAB can steer the vine robot along 3-D paths, in any direction.

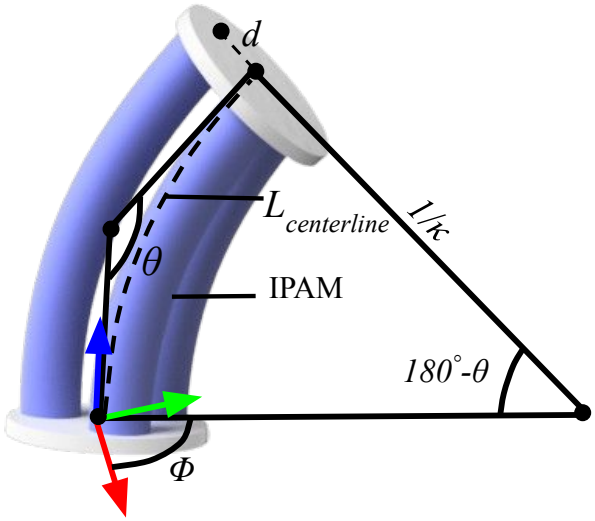


Figure 2.3. The bending/elongating module depicted in a bent configuration. θ is the angle between the perpendicular lines through the center of the IPAM bases at both ends. ϕ is the angle of the plane containing the bend.

Modeling

In [97], an analytical model is derived, using the strain energy function, to accurately predict the non-linear elongation of a hyper-elastic rubber tube that is radially constrained using a metal spring. Because an IPAM is instead radially constrained using a thin, flexible, braided fishing line, we assume here that the radial constraint has a negligible impact on the axial stiffness of an IPAM during elongation, resulting in the following modification of [97]:

$$\delta L_{\text{IPAM}} = \frac{LP\pi d_{\text{in}}^2}{4G\pi(d_{\text{out}}^2 - d_{\text{in}}^2) - P\pi(d_{\text{out}}^2 + 2d_{\text{in}}^2)}. \tag{2.1}$$

In (2.1), L is the unactuated length of the IPAM, d_{in} and d_{out} are the inner and outer diameters of the rubber tube used in the IPAM, respectively, and G is the shear stiffness of the IPAM's rubber tube. G is estimated based on its known shore hardness using the Gent equation [98].

Based on the pressures in each IPAM, the corresponding change in length can be estimated using (2.1). Then, with the elongated lengths of all three IPAMs, L_1, L_2, and L_3, the bending/elongating module length, $L_{\text{centerline}}$, is given as:

$$L_{\text{centerline}} = \frac{L_1 + L_2 + L_3}{3}. \tag{2.2}$$

The configuration angles ϕ and θ are given as in [99]:

$$\Phi = \arctan\left(\frac{\sqrt{3}(L_2 + L_3 - 2L_1)}{3(L_2 - L_3)}\right), \tag{2.3}$$

$$\theta = \pi - \kappa L_{\text{centerline}}, \tag{2.4}$$

with the module curvature κ given by:

$$\kappa = 2\frac{\sqrt{{L_1}^2 + {L_2}^2 + {L_3}^2 - L_1L_2 - L_1L_3 - L_2L_3}}{d(L_1 + L_2 + L_3)}, \tag{2.5}$$

where d is the distance between the module's center and the center of each IPAM. We ignore the effect of gravity on the module's bending and elongation due to its small mass.

When the InchIGRAB is inside a pressurized vine robot, it experiences a restoring moment, M_{R}, during steering:

$$M_{\mathrm{R}} = P_{\mathrm{vine}} \pi r_{\mathrm{vine}}^3 \tag{2.6}$$

As shown in (2.6), M_{R} is directly proportional to the pressure inside the vine robot, P_{vine}, and the cube of the vine robot's radius, r_{vine}. If the vine robot pressure is too high, M_R could prevent the InchIGRAB from attaining acute angles and could even straighten it during steering. Therefore, to eliminate the effect of M_{R}, P_{vine} is decreased to zero during steering.

Finally, if all three IPAMs are elongated simultaneously during each retraction cycle, the total number of cycles (N_{total}) needed to retract a vine robot along the entire colon length (L_{colon}) can be estimated using:

$$N_{\mathrm{total}} = \frac{L_{\mathrm{colon}}}{\delta L_{\mathrm{IPAM}}} \tag{2.7}$$

Design

A simplified relationship describing the force from an IPAM is $F_{\mathrm{IPAM}} = P_{\mathrm{IPAM}} A_{\mathrm{IPAM}} - K_{\mathrm{IPAM}} \delta L_{\mathrm{IPAM}}$, where P_{IPAM} is the pressure in the IPAM, A_{IPAM} is the IPAM's cross sectional area, K_{IPAM} is the axial stiffness of the rubber tube in the IPAM, and δL_{IPAM} is the IPAM's length change. For a given δL_{IPAM} at a known P_{IPAM}, F_{IPAM} can be maximized by either maximizing A_{IPAM} within the constraints of the application or by decreasing K_{IPAM}. In practice, because using softer rubber tubes increases the risk of ballooning between the gaps in the helically wound, radially constraining material, F_{IPAM} is maximized by maximizing A_{IPAM}.

To maximize A_{IPAM}, and consequently F_{IPAM}, we selected an off-the-shelf rubber tube with the largest diameter that kept an overall module diameter below 26 mm and a hollow channel through the center large enough for the vine tail to pass without considerable friction. The selected rubber tube had an outer diameter of 7.94 mm, an inner diameter of 6.35 mm,

and was made of latex rubber (shore hardness of 35A). Based on the model, longer IPAMs enable the InchIGRAB to achieve larger stroke lengths and smaller θ, both beneficial for the application. However, there is a trade-off, since very long IPAMs may lack sufficient axial stiffness to resist buckling or other deformations and result in a larger radius of curvature for the same θ. Therefore, the IPAMs were designed to be 65 mm long. Three IPAMs were positioned 120° apart with $d = 8.25$ mm and attached to rigid 26 mm disks with a center hole of diameter 7 mm. Based on the model estimations, the InchIGRAB can achieve a stroke length of around 18 mm and θ as small as 60° (i.e. a minimum radius of curvature of 50 mm) at the maximum IPAM pressure.

2.3.3 Anchoring Module

Each anchoring module comprises two pneumatically expanding soft actuators. The inner actuator grasps the vine tail during retraction, while the outer actuator enables the InchIGRAB to anchor itself to the vine robot body (Fig. 2.2). These actuators must be able to resist external forces since any slippage of the outer actuator reduces the InchIGRAB's efficiency during translation, and prevents it from achieving the desired configuration during steering. The maximum force that an outer actuator would need to withstand would occur when a step input in pressure is applied to the IPAMs. Therefore, to prevent slippage, $\mu_1 P_{\text{Outer}} A_{\text{Outer}} > 3 P_{\text{IPAM}} A_{\text{IPAM}}$, where μ_1 is the friction coefficient between the vine material and the outer actuator's soft expanding material. P_{Outer} and A_{Outer} denote the pressure and surface area of the expanding outer actuator, respectively. P_{IPAM} and A_{IPAM} are the maximum pressure and cross-sectional area of each IPAM, respectively.

Moreover, if the vine tail slips inside the inner actuator, InchIGRAB cannot execute the retraction task. To prevent slipping, the following must hold: $\mu_2 P_{\text{Inner}} A_{\text{Inner}} > 0.5 P_{\text{vine}} A_{\text{vine}}$. P_{Inner} and A_{Inner} denote pressure and surface area within the inner actuator, respectively, and μ_2, is the friction coefficient between the vine material and the inner actuator.

Therefore, materials of the vine robot and the expanding actuators should have large μ_1

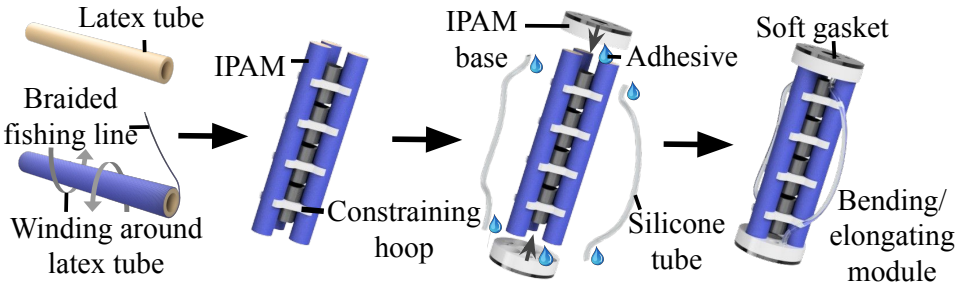


Figure 2.4. Process of fabricating a bending/elongating module includes fabricating the IPAMs and assembling them together with the IPAM bases, constraining hoops, and silicone tubes.

and μ_2, and the actuators should be designed to withstand large internal pressures to maximize P_{Inner} and P_{Outer}. Both anchoring modules were designed to be 18.5 mm long and 26 mm in diameter, with a 7 mm diameter center channel. Dragon Skin$^{\text{TM}}$ 20 was selected for the expanding material for the anchoring modules due to its sufficiently high coefficient of friction with most materials and its strength, which allows the actuators to endure large pressures without failure.

2.3.4 Fabrication

Bending/Elongating Module Fabrication

Figure 2.4 shows the fabrication process for the bending/elongating module. First, the latex tubes are cut to the required length (65 mm) and are tightly wound with 0.8 mm thick braided fishing line to form IPAMs, as outlined in [96]. Three IPAMs are then assembled together using constraining hoops to ensure they remain equidistant. These hoops are 3D printed using the Objet Connex$^{\text{TM}}$ printer and feature a soft tubular center made with Agilus 30$^{\text{TM}}$. The

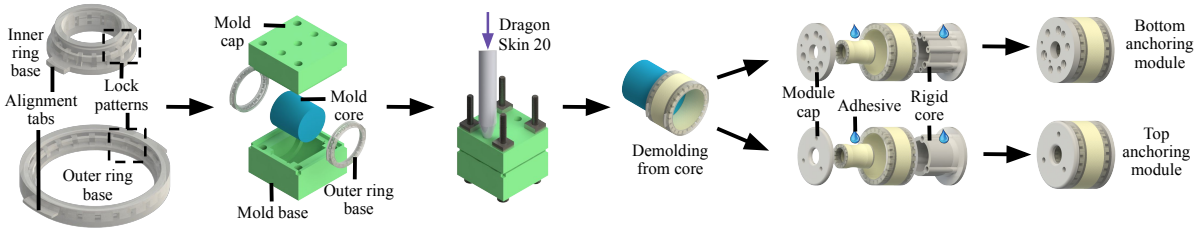


Figure 2.5. The fabrication process for the anchoring modules involves 3D printing ring bases, molding soft silicone with the ring bases, and assembling the actuator rings with rigid core and module cap.

IPAM bases, which are 3D printed with a rigid material (VeroClear^{TM}) with a soft gasket (Agilus 30^{TM}) on one face, are then attached to both ends of the IPAM assembly using cyanoacrylate adhesive. Each IPAM base also includes hollow channels to allow airflow to the IPAMs and the top anchoring module. Silicone tubes supplying air pressure to the top anchoring module are inserted into their designated channels and secured using cyanoacrylate adhesive.

Anchoring Module Fabrication

The fabrication steps for the anchoring modules, inspired by the methods in [100], are shown in Fig. 2.5. First, rigid inner ring bases and outer ring bases are 3D printed for the inner and outer actuators, respectively. The ring bases feature miniature lock patterns designed to mechanically secure the cured soft silicone, which does not otherwise adhere to other materials. A mold core is inserted between two identical ring bases, and this assembly is positioned inside a mold using alignment tabs, which ensure the ring bases are spaced appropriately. Dragon Skin^{TM} 20, in a two-part mix, is then injected at high pressure into the tightly fastened mold, ensuring that it fully permeates into the miniature lock patterns, and is cured inside a pressurized chamber at 40 psi for 4 hours. The pressurized chamber guarantees the infiltration of uncured silicone into the mechanical locking features, preventing the formation of air bubbles. The prepared actuator ring is demolded from the mold core, and the alignment tabs are broken off. Molded inner and outer actuator rings (2.4 mm and 1.8 mm thick, respectively) are then attached to the 3D printed rigid core using cyanoacrylate adhesive, and module caps are secured to the open end.

2.3.5 InchIGRAB Assembly

The final step is to insert and attach seven silicone tubes, each with an outer diameter of 1 mm, to the rigid, 3D printed base. The base is then fastened to the bottom anchoring module using screws. A fully assembled InchIGRAB has an outer diameter of 26 mm and a length of 116 mm (Fig. 5.2), and weighs 40 grams.

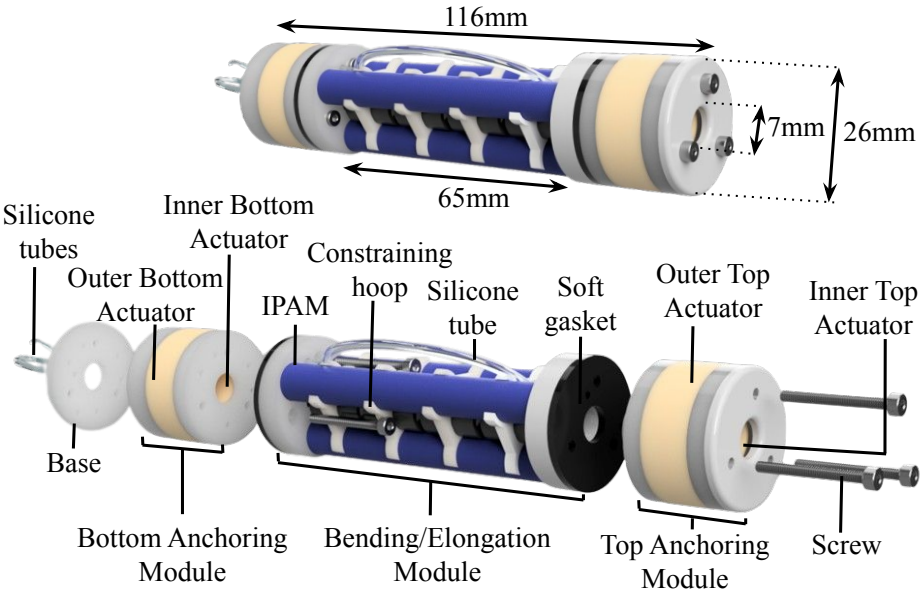


Figure 2.6. (Top) A fully assembled InchIGRAB with a center channel for passing the vine tail. (Bottom) Exploded view of the InchIGRAB showing the assembly of the bending/elongating module with the two anchoring modules and the 3D printed base holding silicone tubes.

2.3.6 Vine Robot

The surrounding vine robot is made using 0.0015" thick Stretchlon® film from Fiberglast due to the material's large tensile strength and low coefficient of friction with itself. To fabricate the vine robot (27 mm in diameter), a long rectangular mylar sheet, with a width of 42.41 mm to match the width of the flattened vine robot, is laser-cut. The mylar sheet is then placed between two Stretchlon® films and heat pressed using a Fancierstudio 16x20 BP flat heat press at 280°F for 60 seconds. The application of heat causes the films to melt and adhere to each other, except in the region where the mylar sheet is placed. After removing the mylar sheet, an enclosed and hollow rectangular section remains. Excess melted portions of the films are trimmed away. The vine robot is completed by heat sealing and then tucking one end of the thin film tube inside itself. We note that it can easily compress to the InchIGRAB's diameter of 26 mm when passing through the narrowest sections in the colon.

2.3.7 Pneumatic Control System

To execute the actuation sequences outlined in Section 4.2, the pressure in the vine robot and all individual actuators in the InchIGRAB must be independently controlled. The vine robot and the bending/elongating module's three IPAMs require analog pressure control, while the four actuators in the anchoring modules only need binary pressure control to switch between grasping and releasing. To provide analog pressure outputs, four voltage-controlled Proportional Air (QBX Series) pressure regulators, which can achieve pressures between 0 psi and 50 psi with a resolution of 0.1 psi, are used. As shown in Fig. 2.7, an Arduino Uno controls the output voltage signals to the pressure regulators through a TCA9548A i2c multiplexer connected to four MCP4725 Digital-to-Analog Converters (DAC). The DACs are used to increase the resolution of the voltage signals sent to the pressure regulators. Four NITRA solenoid valves are controlled with a four-channel MOSFET switch, powered by a 12 V DC power supply, in order to provide binary pressure outputs for the anchoring actuators.

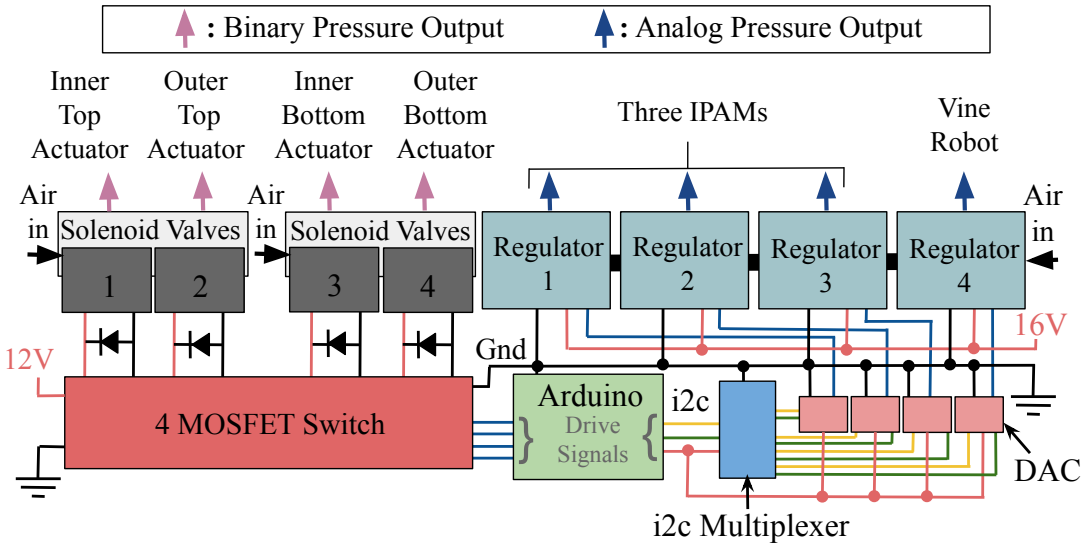


Figure 2.7. A schematic of the pneumatic control system with four analog pressure regulators and four binary solenoid valves, all controlled using an Arduino Uno. It independently regulates the pressures inside all the actuators in the InchIGRAB and the vine robot.

2.4 Device Characterization

In this section, we experimentally validate the analytical model from Section 2.3.2, the anchoring module's effectiveness in preventing slippage, and the durability of the actuators.

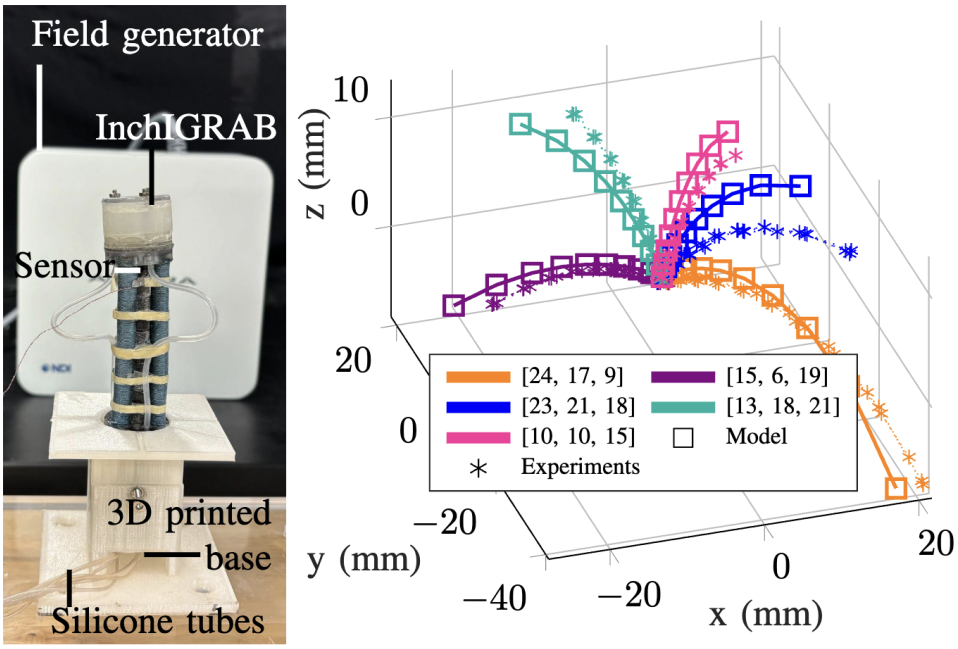
2.4.1 Validation of the Bending/Elongating Model

The experimental setup used for validating the analytical model presented in Section 2.3.2 is shown in Fig. 2.8(a). The base of the InchIGRAB is attached to a 3D printed base positioned in front of the field generator of an Aurora electromagnetic (EM) tracking system (NDI, Waterloo, Canada). The system measures 3D position of the EM sensor (0.92 mm outer diameter) that is attached under the IPAM base, at its center. Five sets of three random pressures between 0 and 25 psi (see Section 2.4.3 for details on the upper bound) are selected from a total of fifteen generated sets. The selection aims to ensure that the bending/elongating module covers a wide range of configurations (κ, ϕ, $L_{\text{centerline}}$). For each pressure set (see legend in Fig. 2.8(b)), each IPAM attains its target pressure after nine equal increments, and the InchIGRAB's position is recorded for each increment. Each set is repeated three times.

The model predicted paths and the measured paths are shown using solid lines and dashed lines, respectively, in Fig. 2.8(b). At the target pressures, the average error and standard deviation of the errors between the model estimations and the observed positions were 7.55 mm (11.62% of the IPAM's original length) and 3.79 mm (5.83% of the IPAM's original length), respectively. The errors are likely due to inaccuracies in sensor placement, inaccuracies in IPAM fabrication, and simplifying assumptions in the model. However, these results demonstrate that the model can closely predict the positions of the tip of the bending/elongating module.

2.4.2 Anchoring Module Characterization

As outlined in Section 2.3.3, both the outer and inner actuators in an anchoring module must resist slippage by enduring the maximum force, $3P_{\text{IPAM}}A_{\text{IPAM}}$, and the force required for retraction, F_{r}, respectively. At the maximum operating pressure of 25 psi, $3P_{\text{IPAM}}A_{\text{IPAM}}$ is



(a) (b)

Figure 2.8. (a) Experimental setup for validating the analytical model in Section 2.3.2. The setup includes an EM sensor mounted on the InchIGRAB, which is secured to a 3D printed base in front of an EM field generator. (b) The model closely approximates the behavior of the bending/elongating module at the studied sets of IPAM pressures. Legend entries show the sets of randomly generated IPAM pressures (given in psi) used for the model validation study.

16.38 N for the chosen IPAM design. Similarly, F_r for the chosen vine robot design is 3.95 N at 1 psi, which is the pressure used for retraction ($0.5P_{vine}A_{vine}$). The selected pressure ensures the vine robot does not buckle during retraction, while keeping the force required for retraction minimal.

We experimentally characterized the relevant slipping forces. In the first experimental setup (Fig. 2.9(a)), the vine robot's body passes over the anchoring module's outer actuator, which is held in place by a fixture. In the second setup (Fig. 2.9(b)), the vine tail passes through the inner actuator of the anchoring module that is clamped using the base clamp. We use a Mark-10 tensile tester to pull the vine robot's body and the vine tail, respectively, both clamped using the gauge clamp, with known forces. Both the outer and inner actuators are actuated at pressures from 2 psi to 30 psi in step sizes of 2 psi. At each actuation pressure, the vine is pulled until it slips. The force versus deflection behavior of each pull is recorded for a pre-set time,

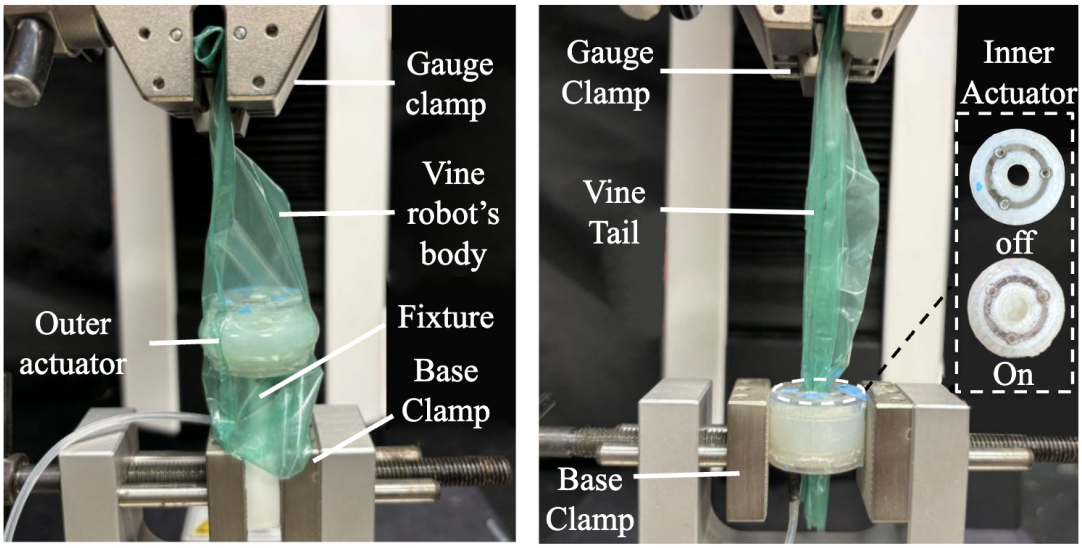
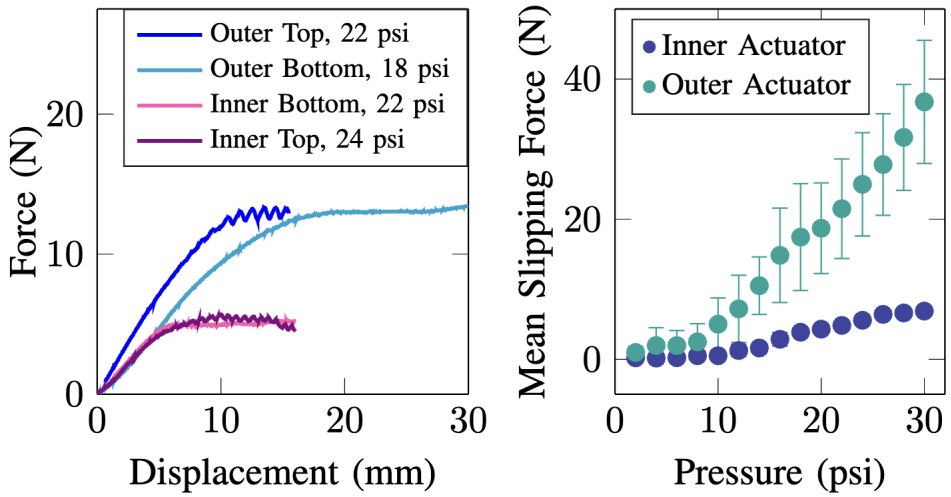


Figure 2.9. Setups for characterizing the forces required for slippage of (a) the outer actuator and (b) inner actuator at different pressures. (b) also shows the top view of an inner actuator, without the vine tail, in its "off" and "on" states.

from which the force required for slippage is extracted. The pre-set time is chosen to ensure that the force versus deflection behavior during slippage is adequately captured. This procedure is repeated for six inner actuators and six outer actuators, with three each from the top anchoring module and the bottom anchoring module.

The force versus deflection behavior of each pull was observed to have a steep linear region that plateaus as the pull displacement increases, as shown in Fig. 2.10(a). The plateauing behavior is achieved as the vine tail or body slips when pulled. For each force versus deflection plot, we defined the mean slipping force as the average of the forces recorded in the plateau region, identified manually as the segment with a significantly reduced slope compared to the preceding steep region. Fig. 2.10(b) displays all recorded mean slipping forces and their standard deviations. The standard deviations of the mean slipping forces for the outer actuators are notably larger than those for the inner actuator likely due to two main reasons. First, the magnitude of the mean slipping forces for the outer actuators are significantly higher. Second, residual cured adhesive was observed on the exterior of one of the outer actuators, which could



(a) (b)

Figure 2.10. (a) Example force versus deflection behaviors recorded while the vine tail and body are pulled through the actuated inner actuator and around the actuated outer actuator, respectively. (b) Pressure versus mean slipping force for the inner and outer actuators.

have adhered to the vine robot's body and increased the measured slipping force. Based on the obtained pressure versus mean slipping force information, P_{Inner} and P_{Outer} are both selected to be 25 psi relative to the pressure in the vine robot, which enables them to withstand the necessary forces of 3.95 N and 16.38 N, respectively.

2.4.3 Durability Characterization

To determine the maximum pressures that the system can withstand, the vine robot and each actuator in an assembled InchIGRAB were pressurized individually at increments of 1 psi until failure. IPAM failure occurred at an average of 34 psi when they expanded radially, ballooning through the gaps between the braided fishing lines. The maximum operational pressure for each IPAM was then chosen to be 25 psi relative to the vine robot pressure, giving a safety factor of 1.36. The inner and outer actuators in both anchoring modules remained operational even at 50 psi, the maximum pressure achievable by the pressure regulator. The vine robot elastically expanded until the heat pressed edges started to separate at an actuation pressure of 3.5 psi.

We then assessed the maximum number of actuation cycles that all seven actuators can endure. All actuators in an InchIGRAB (with no vine robot) were sequentially pressurized at their operational pressures in the retraction sequence for a total of 5000 cycles. The number of actuation cycles was recorded, and the status of the actuators was inspected after every 50 cycles. If an actuator failed, it was reported to withstand the number of cycles recorded during the last inspection. IPAMs and the two inner actuators survived all 5000 cycles. The outer actuators in the top and bottom anchoring modules operated for 2250 and 1750 cycles, respectively, before failing at the interfaces between their soft and rigid structures. The superior performance of the inner actuator can be attributed to its soft structure pressing against itself during actuation, resulting in lower mechanical stresses compared to its counterpart. We note that the outer actuators are expected to withstand a larger number of cycles in the presence of the vine robot, as the vine robot will restrict their expansion. Assuming no slippage, the InchIGRAB would be able to reach the end of an average colon (1.5 m) [101], and return back after only 167 actuation cycles. Hence, the actuators in the tested InchIGRAB would have endured a minimum of 13 procedures.

2.5 Motion Characterization

In this section, we characterize the motion of the InchIGRAB and the vine robot through mock colon segments at different bent angles (see supplemental videos), showcasing the strategies used for deploying the system during both forward and retraction motions.

2.5.1 Motion Characterization Setup and Procedure

The experimental setup consists of a mock colon segment (Fig. 2.11) constructed using a clear Low-Density Polyethylene (LDPE) thin-film tube connected to four evenly spaced O-rings. The O-rings provide structural support to the otherwise easily collapsible LDPE film tube, and are adhered to a test platform at only four specific points, resembling key characteristics of

the human colon. The LDPE film tube has a diameter of 48 mm, the average diameter of a human colon [102], and the differences in surface properties between LDPE and other phantom materials does not impact the presented system's performance, due to the vine robot's method of movement via tip-eversion.The test platform itself consists of a pin joint that allows the attached mock colon segment to bend at its midpoint, mimicking the configurations of various colon segments. Three different angles are considered for the motion characterization as follows: 180° to mimic the rectum and descending colon; 130° to approximate the obtuse angles of the transverse colon and the ascending colon; and 80° to mimic the acute angles of the hepatic flexure, splenic flexure, sigmoid-rectal flexure, and the sigmoid colon [103].

In the fully assembled robotic system, the InchIGRAB sits at the tip of the vine robot, and predetermined lengths of the vine tail and InchIGRAB air-pressure lines are packed behind it. These lengths allow the system to travel 300 mm within the mock colon segment, which represents 20% of the average colon length, without requiring external intervention. The vine robot's base is finally sealed after inserting a silicone tube for supplying air pressure to the vine robot.

The pneumatic control system, connected to a computer, is used to regulate the actuation

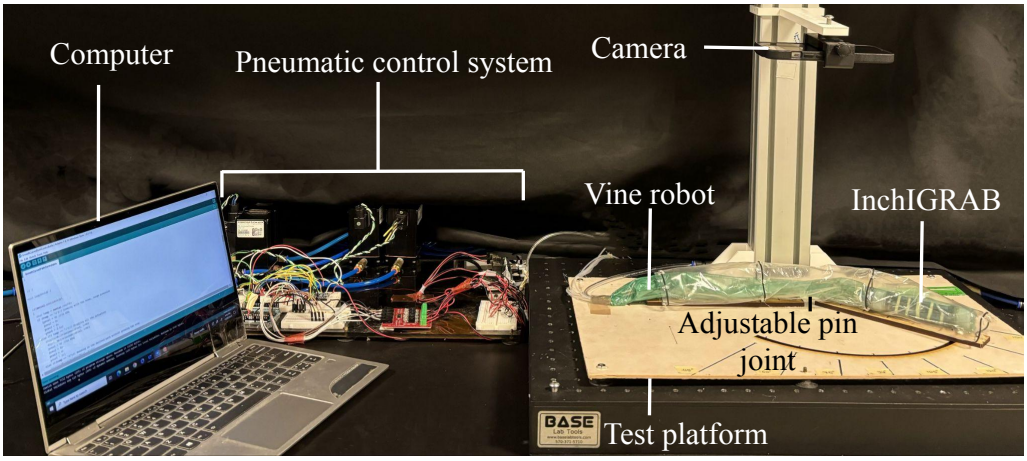


Figure 2.11. The experimental setup used for motion characterization of the InchIGRAB in the vine robot includes a mock colon segment placed on a test platform, recorded by a camera. The pneumatic control system, connected to a computer, is used to control the InchIGRAB and the vine robot.

pressures in both the InchIGRAB and the vine robot. When steering, the pressures in the IPAMs are regulated as determined by the model presented in 2.3.2, ensuring that the InchIGRAB's configuration matches that of the mock colon segment. Lastly, a camera is mounted parallel to the test platform to record the motions of the system (see Fig. 2.11), and Tracker, an open source video analysis tool, is used to track the tip of the InchIGRAB and the vine robot.

2.5.2 Forward Motion

180°

The pressure in the vine robot was set to 1.8 psi, allowing it to grow forward. The InchIGRAB, with all its actuators turned off, moved forward passively due to the friction between the vine tail and the InchIGRAB's hollow channel. The vine robot and the InchIGRAB moved the entire 300 mm distance together in just 2.5 seconds, as shown in Fig. 2.12(a). We note that this time could vary depending on the pressure set inside the vine robot.

130°

The vine robot and the InchIGRAB successfully advanced in three distinct steps. In the first step, the vine robot and the InchIGRAB moved forward together, using the strategy outlined in Section 2.5.2, until reaching the curve. In the second step, the pressure inside the vine robot was reduced to 0 psi and the IPAMs were actuated to achieve a 130° bend, based on the model estimates. Simultaneously, the bottom anchoring module's outer actuator anchored the InchIGRAB to the vine robot. The wrinkles at the vine robot's bent section helped the InchIGRAB maintain its angular configuration, even after the vine robot's eversion, by reducing the robot's structural stiffness [104]. In the final step, the InchIGRAB executed the inchworm-like motion with an average displacement of 15.36 mm per cycle to reach the vine robot's tip, as explained in Section 4.2 and observed in Fig. 2.12(b). Although forward motion through segments with minimal curvature could also be achieved using the same strategy as that used in Section 2.5.2, our approach ensures successful navigation with minimal forces applied

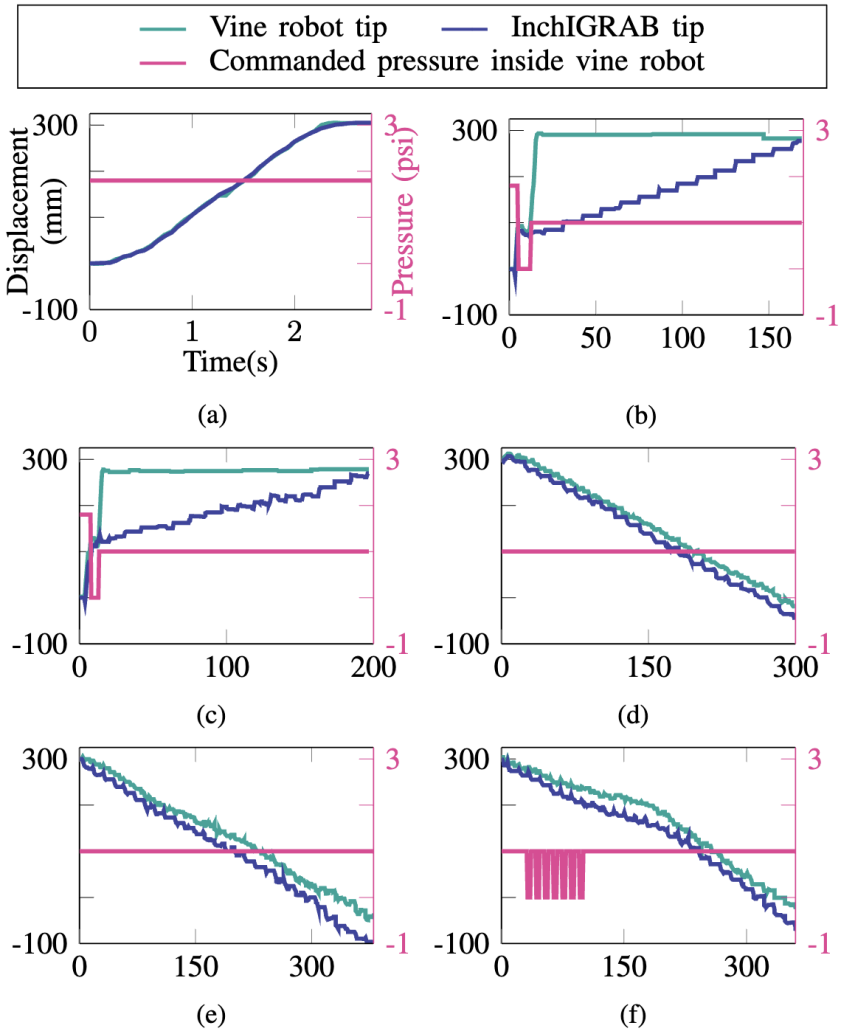


Figure 2.12. Results showing the tracked vine robot's tip, the InchIGRAB's tip, and the commanded pressure inside the vine robot during the forward motion in the (a) straight, (b) 130°, and (c) 80° mock colon segments. Similarly, the tracked vine robot's tip, the InchIGRAB's tip, and the commanded pressure inside the vine robot during the retraction tasks are shown in the (d) straight, (e) 130°, and (f) 80° mock colon segments.

to the environment.

80°

Forward motion in the segment with an 80° bend was successfully achieved using the strategy outlined in Section 2.5.2. However, increasing the pressure in the vine robot to allow growth around the curve slightly increased the InchIGRAB'S angle from its initial configuration.

This angle change is due to a small residual restoring moment, despite the wrinkles at the bent location [104], and the amount of change is limited by the surrounding environment. This sharper bend angle also resulted in lower efficiency in the InchIGRAB's translation, as seen in Fig. 2.12(c). The InchIGRAB performed the inchworm-like motion with an average displacement of 10.58 mm per cycle. This reduction in translation efficiency is likely due to the significant amount of wrinkles in the vine body at the sharp bend, which constantly unwrinkle, then rewrinkle as the InchIGRAB extends and then contracts each cycle, leading to smaller and more variable increments of movement. Despite the challenges, the InchIGRAB-guided vine robot successfully reached the targeted displacement with minimal interaction with its environment.

2.5.3 Retraction

180°

The InchIGRAB successfully retracted the vine robot by performing the inchworm-like motion in the backward direction, with an average displacement of 13.82 mm per cycle. Throughout the retraction motion, the pressure in the vine robot remained constant at 1 psi to avoid buckling of the robot body. In Fig. 2.12(d), it can be observed that the gap between the InchIGRAB's tip and the vine robot's tip increased as the InchIGRAB advanced. This increasing gap likely resulted from unwanted eversion of the scrunched vine tail, during the InchIGRAB's relaxation in the retraction sequence. Nonetheless, the InchIGRAB successfully retracted the vine robot to the target displacement.

130°

The InchIGRAB successfully retracted the vine robot in the same manner as in the straight segment. The retraction sequence was executed with an average displacement of 11.34 mm per cycle. At the end of this study, a larger gap between the InchIGRAB's tip and the vine tip was observed, as shown in Fig. 2.12(e). The increase in friction between the inside of

the InchIGRAB's hollow channel and the vine tail, at the bent region, may have caused a longer length of the vine tail to scrunch and evert.

80°

The InchIGRAB retracted the vine robot using the same process as in the other segments, until it reached the curve. At this point, due to the kink in the vine robot caused by the sharp bend, its pressure was reduced to 0 psi to enable the InchIGRAB to pass. This adjustment was synchronized with the InchIGRAB's elongation in the retraction sequence. The pressure inside the vine robot wasreset to 1 psi before the InchIGRAB's relaxation, to avoid buckling. This approach of coordinating the duty-cycling of the vine robot pressure with the InchIGRAB's retraction sequence was repeated until the bottom anchoring module successfully passed the kinked region (seen in the supplemental video). The InchIGRAB then retracted the vine robot the remainder of the way using the standard approach. As seen in Fig. 2.12(f), the retraction speed increased after the InchIGRAB passed the kinked region. The InchIGRAB completed the vine robot's retraction, averaging a displacement of 11.60 mm per cycle.

2.6 Demonstration

A mock colon environment, shown in Fig. 2.13 was created using a 1.5 m long LDPE tube, which matches the average length of a human colon [101]. The lengths of the segments within the colon model were also consistent with those of the human colon [101]. Similar to the experimental setup detailed in Section 2.5.1, the diameter was 48 mm and featured equally spaced O-rings attached to the base. Additionally, the model included a transverse colon segment with a 3-D path, as shown in Fig. 2.13, consisting of two 30° slopes.

Figure 2.13 and the supplemental video show the forward motion and retraction of the InchIGRAB-enabled vine robot along the entire colon length, using the strategies previously detailed. The tubes and vine tail were manually fed into the vine robot during the forward motion and removed during retraction. During the forward motion, the InchIGRAB steered the

vine robot around the curved colon sections. Since the configuration of the model was known, the sets of pressures in the IPAMs were pre-determined for each curvature in the colon, using the model presented in Section 2.3.2. The pneumatic control system then supplied the actuators with the required pressures. The tips of both the InchIGRAB and the vine robot reached the distal end of the colon in 24 minutes and 20 seconds. Similarly, the InchIGRAB safely retracted the vine robot for a total distance of 1.45 m in 22 minutes and 25 seconds, completing 94 retraction cycles, compared to the 81 cycles estimated using (7). The discrepancy between the estimated and observed number of retraction cycles can primarily be attributed to slippage of the anchoring modules and reduced translation efficiency at the curved sections.

We demonstrated the proposed robotic system's ability to successfully navigate the entire length of the colon during both forward motion and retraction, with minimal friction and environmental interaction. The average speeds of the InchIGRAB-enabled vine robot during forward motion and retraction in the mock colon were recorded at 1.03 mm/s and 1.12 mm/s, respectively. This makes the current version of the system slower than other robotic colonoscopes, such as those presented in [29], [79], and [80]. However, the speed of the presented system can be improved by reducing the relaxation time required for the IPAMs to return to their original lengths. Currently, this relaxation step takes approximately 7 seconds, resulting in notably long durations for translation motions, as shown in Fig. 2.12. Actively depressurizing the IPAMs with a vacuum regulator can significantly improve the completion

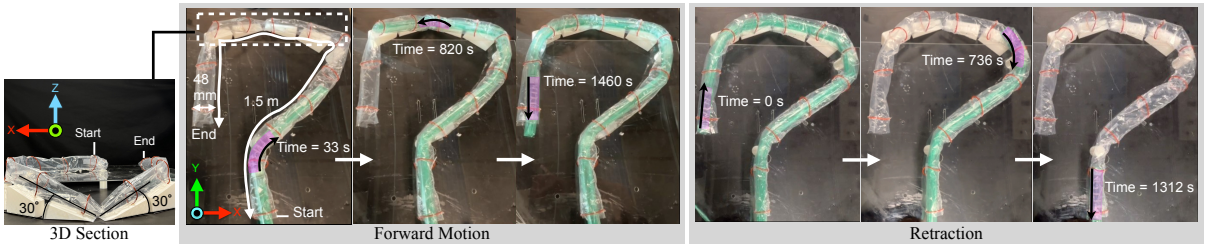


Figure 2.13. Still-frame images show the InchIGRAB (highlighted in pink for better visibility) and the vine robot successfully navigating a full mock colon environment, which features a 3D section. During forward motion, the InchIGRAB steers the vine robot around the curved sections of the colon model before the vine robot grows to the next curve. This process is repeated until both the InchIGRAB and the vine robot reach the distal end of the colon. The InchIGRAB then safely retracts the vine robot backward along the entire colon length.

time for retraction and forward motion. Additionally, the presented system's speed can be further improved by automating the management of the silicone tubes and vine tail using spooling mechanisms inside a pressurized chamber, as demonstrated in [87].

Compared to other robotic colonoscopes (such as [79], [26], [27]), InchIGRAB offers several key advantages. First, unlike highly curved cable-operated robots, where friction losses [105] can affect steering precision, the steering in InchIGRAB is unaffected by the curvatures attained by the vine robot. Second, InchIGRAB does not require large equipment or additional infrastructure like that required by magnetically driven robots [79], [80], [106]. Third, compared to retracting tethered robotic colonoscopes, which risks complications due to the potential of excessive traction and tension on the mesocolon during the pulling process [107], the InchIGRAB-enabled vine robot retracts from its tip with minimal shear forces on the environment.

2.7 Discussion

In this chapter, we presented a soft robotic system for colonoscopy that consists of the InchIGRAB nested within a vine robot. An analytical model was used to design the InchIGRAB to navigate the vine robot around tight curves, and the model was able to accurately predict the position of the bending/elongating module with an average error and standard deviation of 7.55 mm and 3.79 mm, respectively. The InchIGRAB's actuators were found to endure at least 1750 cycles, which is approximately 13 times more than what is required for the entire colonoscopy procedure, when subjected to their respective operational pressures. Furthermore, the presented robotic system successfully showcased its ability to safely traverse different segments of the colon during both forward motion and retraction.

Future work can include the design of a pressurized chamber comprising spooling mechanisms for the vine robot tail and silicone tubes. Sensors can also be integrated into the InchIGRAB to enable its closed-loop control. In addition, a camera or other tools could be

threaded through the vine tail to enable visualization or manipulation. In these scenarios, the impact of the tool on the translation of the InchIGRAB should also be studied. Furthermore, the diameter of the existing robotic system can be further reduced by designing novel actuators capable of large forces, while occupying a small footprint, for the bending/elongating module. All these improvements would further enhance the presented robotic system, bringing it closer to enabling safer robotic colonoscopy.

2.8 Acknowledgements

This chapter is, in part, a reprint of material from A. Giri, C. Girerd, J. Cervera-Torralba, M. Tolley, and T. Morimoto, *"InchIGRAB: An Inchworm-Inspired Guided Retraction and Bending Device for Vine Robots during Colonoscopy."* The source material has been submitted for publication. The dissertation author is the primary author of this paper.

Chapter 3

Design of Soft, Positive-Pressure Actuated Suction Cups for Anchoring in Minimally Invasive Surgery

3.1 Introduction

3.1.1 Background

Soft suction cups have been proposed for a wide range of applications, including for wall climbing robots [108, 109], tissue manipulators [110], and grippers [111, 112], for example. These suction cup designs can be broadly classified as active or passive based on the use or lack of actuation mechanism, respectively [113]. While passive suction cups have relatively simple designs, they require external forces to attach and detach from the substrate, making it difficult to control their adhesion states. In addition, the attachment force provided by a passive suction cup is difficult to regulate. In contrast, attachment and detachment states and attachment force can be easily controlled in active suction cups, making them more well-suited for interactions with fragile objects or in sensitive environments such as in Minimally Invasive Surgery (MIS).

3.1.2 Previous Work

Different actuation mechanisms, including dielectric elastomers [114], magnets [110], vacuum pressure [115, 112, 116], and positive pressure [42], have been explored for actuating soft suction cups.

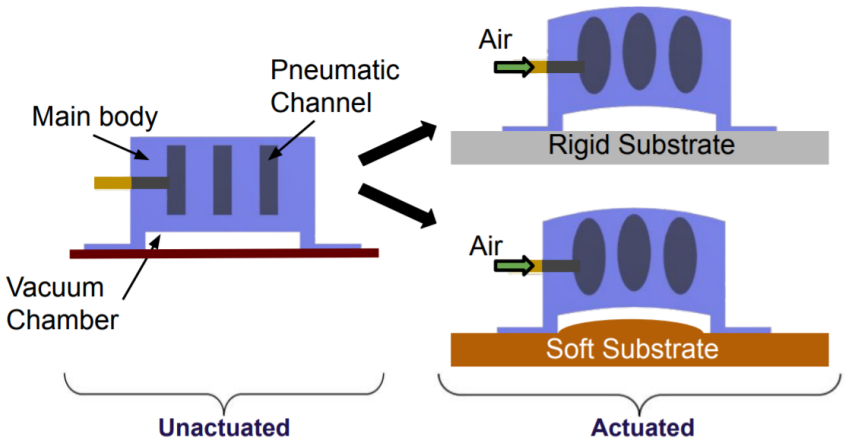


Figure 3.1. Schematic showing the cross-section of a positive-pressure actuated suction cup on rigid and soft substrate before and after positive pneumatic load is applied to the pneumatic channel.

Among the several actuation mechanisms, vacuum actuation has been the most heavily explored because these suction cups are simple in design [117] and can hold large loads [118]. However, vacuum actuated suction cups may pose a challenge for use in MIS where CO2 insufflation is commonly used to help expand the workspace and provide better visibility during procedures [40, 41], since a vacuum could result in the loss of insufflation.

In contrast, recently developed positive-pressure actuated suction cups [42] offer several potential advantages. These suction cups consist of a pneumatic channel embedded inside the main body, and a cavity, or vacuum chamber, between the body and the substrate, as shown in Fig. 3.1 and Fig. 3.2 . When positive pneumatic load is applied, the channel inflates, causing the body to bend away from the substrate. The increase in volume in the vacuum chamber results in a pressure difference that leads to a suctioning effect. Such suction cups operate without drawing in fluid or contamination from the environment and do not buckle during actuation. The switchable adhesion also allows them to easily attach and detach from the substrates [42]. These advantages make positive-pressure actuated suction cups good candidates for use in demanding applications such as surgical procedures.

In addition to recent progress in novel suction cup designs, there has also been developments in modeling their behavior [119, 120]. Finite Element Analysis (FEA) was used in [121] to model the deformation of clingfish-inspired suction cups on a rigid substrate. Similarly, a simplified analytical model was presented in [42] to model the adhesion of a positive-pressure actuated suction cup to a rigid substrate. However, the presented model requires experimental evaluation of a selected design to determine the parameters used in the model, and therefore cannot be used for large-scale optimization studies. Moreover, while suction cup designs have been presented for applications on soft substrates such as skin and tissues [111, 122], developed models are limited to attachment to rigid substrates. In order to enable systematic design of soft suction cups for many of these real-world applications, including MIS, it is therefore critical to develop models for their interaction with soft substrates.

3.1.3 Contributions

The contributions of this work are as follows. (1) We present an FEA model that enables the simulation of the behavior of positive-pressure actuated suction cups on both rigid and soft substrates. This model allows us to estimate the attachment force of the suction cups and to study the non-intuitive behavior of a wide range of designs for optimization purposes. (2) We present a case study of designing a positive-pressure actuated suction cup to anchor flexible surgical tools to surrounding tissues to help stabilize them during procedures. We identify a design that provides maximum attachment force and conduct experimental evaluations to characterize its performance. We also demonstrate the ability of the suction cup to resist external forces on rigid, soft, and live porcine substrates, thereby demonstrating the suction cup's potential as an anchoring unit for stabilizing surgical tools. The chapter is structured as follows: the FEA modeling, optimization process, and fabrication method are described in Section 3.2. The optimization results and experimental evaluations are then presented in Section 3.3, and a conclusion is provided in Section 3.4.

3.2 Materials and Methods

In this section, we develop an FEA model of the positive-pressure actuated suction cups. The developed model is used to characterize suction cup's performance and optimize its design to achieve the maximum possible attachment force for our selected case study.

3.2.1 Operating Mechanism

Positive-pressure actuated suction cups [42] consist of an embedded pneumatic channel that, when pressurized, causes the main body of the suction cup to bend away from the substrate (see Fig. 3.2). The volume of the vacuum chamber beneath the main body therefore increases by ΔV, leading to a pressure difference, ΔP, between the vacuum chamber and the environment.

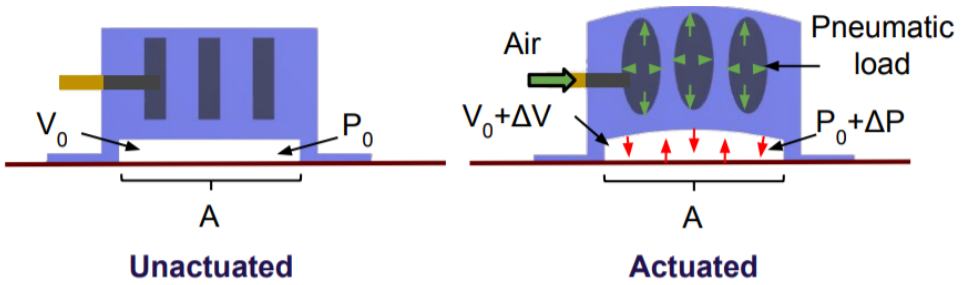


Figure 3.2. Positive-pressure actuated suction cup before and after pneumatic load is applied to the pneumatic channel. When actuated, the volume in the vacuum chamber increases from an initial value, V_0, by an amount, ΔV and pressure increases from an initial value, P_0, by an amount, ΔP. ΔP introduces load to the walls encapsulating the vacuum chamber, as shown in red. The base area of the vacuum chamber, A, is considered to remain approximately constant during actuation.

This change in pressure is given by Eq. (3.1) as stated by Boyle's law,

$$\Delta P = P_o \left(\left(\frac{V_o}{V_o + \Delta V} \right) - 1 \right), \tag{3.1}$$

where P_o is the pressure in the environment (i.e. the atmospheric pressure)and V_o is the initial volume inside the unactuated vacuum chamber. In the absence of external loads, this ΔP gives rise to an attachment force, which can be calculated as in Eq.(3.2)

$$F = \Delta P \cdot A, \tag{3.2}$$

where A is the base area of the deformed vacuum chamber. We approximate the base area of the vacuum chamber after deformation to be equal to that before deformation, which is a valid assumption provided the base of the suction cup remains attached to the substrate during actuation. We ensure that the base remains attached to the substrate by adding a thin lip at the base of the suction cup to maintain a proper seal.

It is desirable to achieve a large attachment force so that the suction cup on its own, or as a unit in an anchoring system with multiple suction cups, can resist the largest forces possible. We hypothesize that the suction cup's ability to resist external forces is directly correlated to its

attachment force in the absence of any external loads. Attachment force, F, is thus the selected metric considered for evaluating suction cup performance.

3.2.2 FEA Modeling

FEA can be accurately used to study the intrinsic nonlinear behavior exhibited by soft materials [123]. We used COMSOL Multiphysics (COMSOL, Inc., Burlington, USA) to develop an FEA model that estimates the achievable attachment force of a suction cup for a given pneumatic load. The material selected for the suction cup is Ecoflex 00-30, a soft silicone rubber, which we model using the hyperelastic Yeoh model with $C_1 = 17$ kPa, $C_2 = 0.2$ kPa, and $C_3 = 0.023$ kPa [124]. We used a Poisson's ratio of 0.49 in our simulations to mimic the incompressibility of the material [125].

For our simulation studies, we constrained the bottom surface of the suction cup to be fixed relative to the substrate, assuming that the seal is maintained and does not deform during

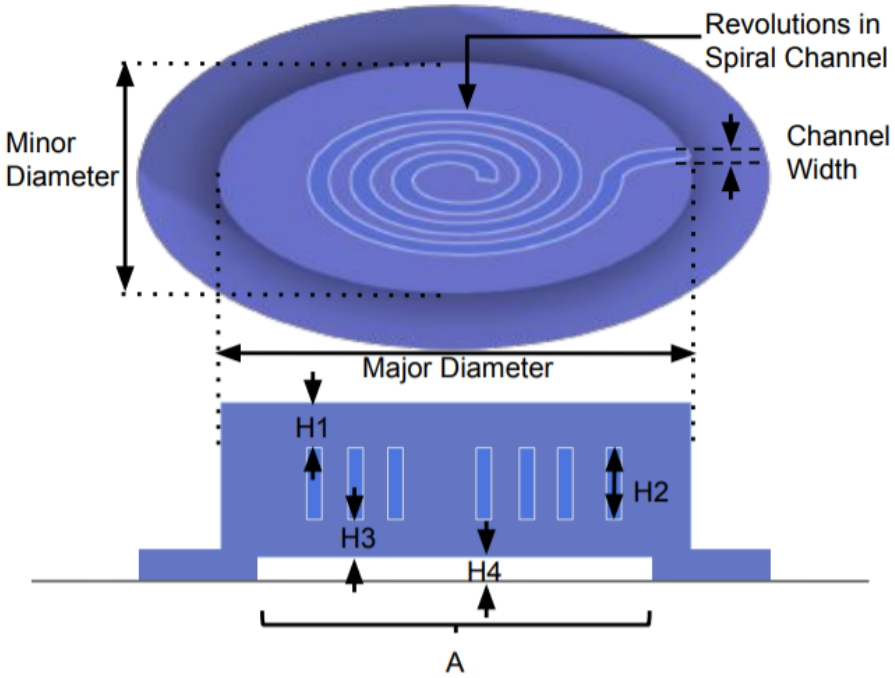


Figure 3.3. Top view (top) and cross-sectional view (bottom) of a suction cup with its geometric parameters that were considered as design parameters for the FEA optimization study.

actuation. The input pneumatic load, responsible for the bending of the suction cup, is applied to the walls of the embedded channel. ΔP generated in the vacuum chamber during actuation also results in a load on the encapsulated walls of the vacuum chamber, which is also included in our simulation.

If the substrate is soft, it is also subjected to deformation due to the load resulting from the pressure drop in the vacuum chamber. To account for the resultant deformation of the soft substrate, an accurate material model of the substrate is required. Although hyperelastic constitutive models have been developed for tissues like porcine liver [126], variances in the model parameters are large and unpredictable between different specimens. Because Ecoflex 00-30 has been found to have a similar stress distribution trend and shear modulus as published values for porcine muscle [127] and has well-known material properties [124], it is used as the soft substrate in our simulation studies and model validation. The resultant deformation of the soft substrate along with the deformation of the encapsulated walls of the vacuum chamber result in the corresponding increase in volume in the vacuum chamber, ΔV, which is different to that obtained on a rigid substrate. Eq. (3.1) and Eq.(3.2) can then be used to calculate the attachment force of the suction cup on the chosen soft substrate.

3.2.3 Design Parameters and Optimization Study

We focus here on improving the stabilization of flexible surgical tools during MIS. Large forces can often be involved at the distal end of these tools, leading to unintended bending and deflections of the surgical tool and target tissue that increase the control difficulty [128, 129]. The goal is to design a suction cup capable of providing the largest attachment force, while remaining within the necessary size constraints of the application.

Based on the selected application, which is stabilizing flexible sugical tools during MIS, we determined the associated constraints on each design parameter as follows. The area of the vacuum chamber's base was selected to be equal to that of a circle with a diameter of 25 mm and was constant for the entire design set investigated in our optimization study. This pre-selected

Table 3.1. Design parameters and their corresponding dimensions considered for the FEA optimization study.

Parameter	Min	Max	Step size
Aspect Ratio	1.00	2.50	0.50
H1 (mm)	1.00	4.00	0.50
H2 (mm)	1.00	4.00	0.50
H3 (mm)	1.00	4.00	0.50
H4 (mm)	1.00	4.00	0.50
Channel Width (mm)	1.00	1.30	0.15

area ensures that the suction cup is small enough to easily attach to the surgical tools, while being able to generate larger attachment forces than designs with smaller base area. The channel design was selected to be an Archimedean spiral with 2.75 revolutions for the entire design set. The positive pressure suction cup designs introduced in [42] also considered Archimedean spiral as the chosen channel design. For other design parameters listed in Table 3.1, a range of dimensions is considered. The optimization study is conducted by running simulations for every combination of selected dimensions for all the design parameters.

The aspect ratio, or the ratio between the major and minor diameters of the main body, was selected as a design parameter. Slender suction cups are likely to better conform inside tubular environments such as gastrointestinal tract compared to circular ones. Aspect ratios of 1, 1.5, 2, and 2.5 were selected for our study. The height of the material above the channel (H1), height of the channel (H2), height of the material below the channel (H3), and height of the vacuum chamber (H4) were also considered. The total height of the suction cup was constrained to be 7 mm to ensure the suction cup could easily fit into both ports and tight spaces in natural orifices while attached to the surgical tools. The minimum value of layer height and width was selected to be 1 mm, as anything smaller can be difficult to fabricate, and the step size was set at 0.5 mm. The constrained total height also dictated the limitations in the maximum heights for the considered parameters. Finally, channel widths of 1 mm, 1.15 mm, and 1.3 mm were

investigated. Each individual parameter's effect on the suction cup's performance was coupled with that of the others because of the constrained total height and base area.

In order to find a suction cup that can maximize the attachment force, we performed an FEA optimization study where the geometric parameters shown in Fig. 3.3 were varied over the range of dimensions listed in Table 3.1. Pneumatic loads of 2 kPa, 9 kPa, and 16 kPa were selected as representatives for small, medium, and large applied loads. Larger loads were not considered in order to prevent ballooning effects [130] caused by large strains.

A total of 1008 suction cup designs was obtained based on the combination of all design parameters under the defined constraints. The entire design set was used for an FEA optimization study on a rigid substrate at the 3 selected pneumatic loads, for a total of 3024 designs. The time required to complete the study was 61 hours on a Intel(R) Core(TM) i7-8700K CPU with 16 GB RAM.

3.2.4 Fabrication

Suction cups are fabricated using Ecoflex 00-30. The two part liquid mixture is combined with a 1:1 weight ratio, degassed using a vacuum container, and poured into 3-D printed molds, as seen in Fig. 3.4a. The liquid mixture is left to cure for 3 hours at room temperature before being removed from the molds. Mold 1 (Fig. 3.4a) consists of the spiral channel pattern, and the associated Part 1 consists of a negative spiral space (Fig. 3.4b), which will eventually act as the pneumatic channel. Mold 2 is used to fabricate the base of the suction cup, and the associated Part 2 consists of the vacuum chamber and a thin surrounding lip. The two cured parts are then attached together with a thin layer of Ecoflex 00-30 (Fig. 3.4c) and left to cure for 3 hours. Finally, a silicone tube for supplying air to the pneumatic channel is attached using a silicone adhesive (Smooth-on Sil-poxy), resulting in a final functional suction cup, as shown in Fig. 3.4d.

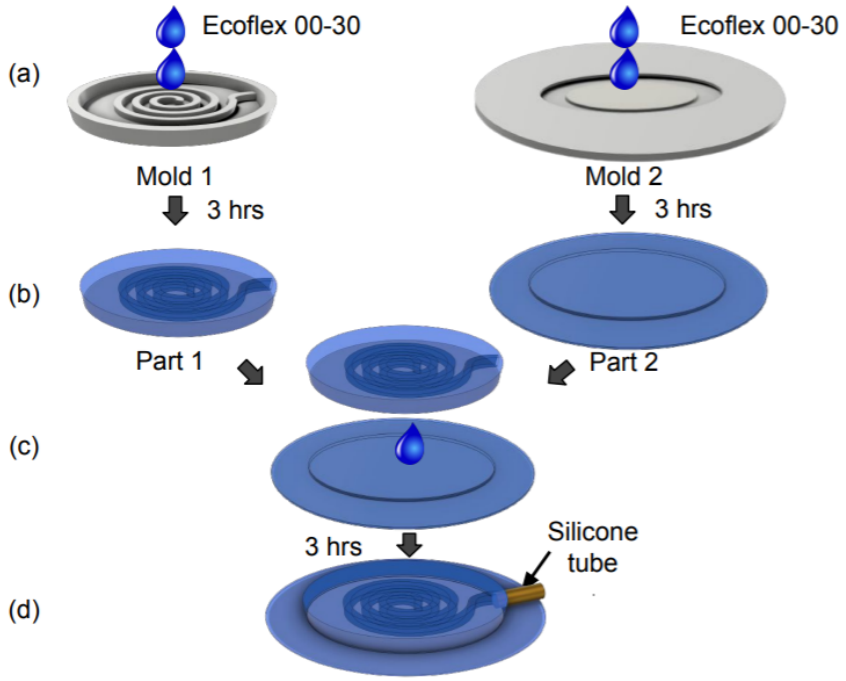


Figure 3.4. The process for fabricating a positive-pressure actuated suction cup includes (a) pouring Ecoflex into the two molds, (b) removing the two soft parts after they are cured, (c) assembling the two parts together using Ecoflex, and (d) attaching a silicone tube used for supplying air to the pneumatic channel.

3.3 Results

In this section, we present results of the optimization study, along with results from experiments evaluating the performance of the optimized design on rigid, soft, and in-vivo porcine substrates.

3.3.1 Optimization Results

The attachment force generated based on the three different pneumatic loads was analyzed for the set of studied suction cup designs. We observed three distinct behaviors, as illustrated by Design 1, Design 2, and Design 3 in Fig. 3.6. For Design 1, which is also the best performing design, the attachment force increases with the increase in pneumatic load. The attachment force produced by Design 2, on the other hand, decreases with the increase in pneumatic load. This is due to the fact that for Design 2, the suction cup's main body bends

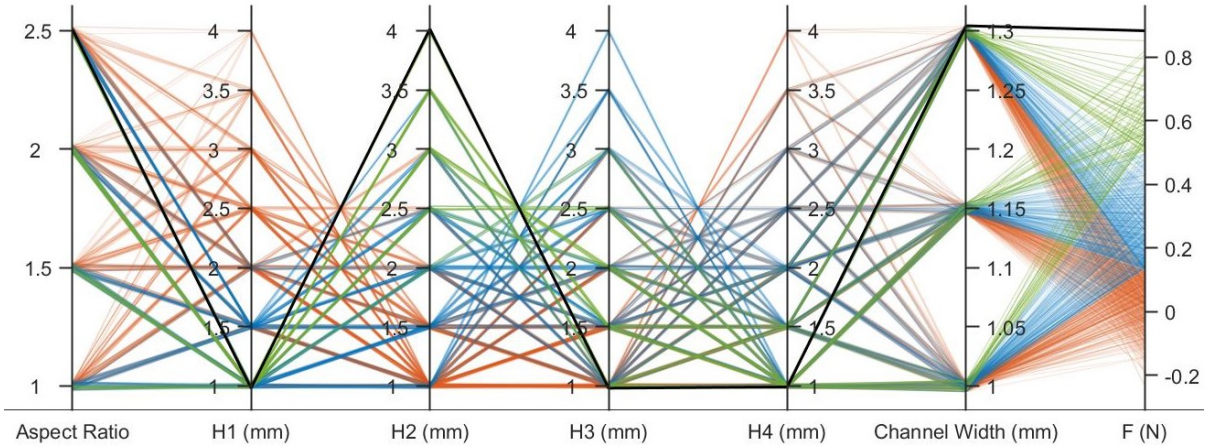


Figure 3.5. Results showing parameter dimensions and generated attachment force for 1008 designs at the pneumatic load of 16 kPa on a rigid substrate. Each design is represented by lines connecting the dimensions of individual geometric parameters and corresponding values of F. The lines are color coded based on the anchoring force F generated for the studied designs, where the best performing design is shown in black, designs producing F between 0.860 N and 0.496 N are shown in green, those producing F between 0.496 N and 0.133 N are shown in blue, and designs producing F below 0.133 N are shown in orange.

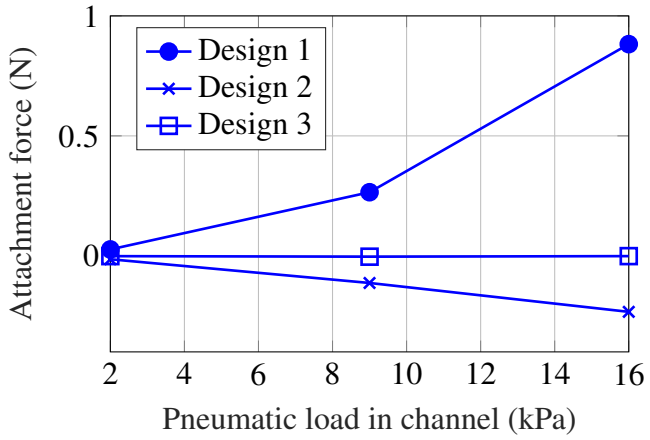


Figure 3.6. Three representative behaviors observed for the studied suction cup designs at the selected pneumatic loads. Design 1 has Aspect ratio = 2.5, H1 = 1 mm, H2 = 4 mm, H3 = 1 mm, H4 = 1 mm, and Channel width = 1.3 mm. Design 2 has Aspect ratio = 2.5, H1 = 4 mm, H2 = 1 mm, H3 = 1 mm, H4 = 1 mm, and Channel width = 1.3 mm. Design 3 has Aspect ratio = 1, H1 = 2.5 mm, H2 = 2 mm, H3 = 1 mm, H4 = 1.5 mm, and Channel width = 1 mm.

in the direction opposite to that observed in Design 1, resulting in the volume of the vacuum chamber to decrease with the increase in pneumatic load. Finally, the attachment force produced by Design 3 remains relatively unchanged across the three studied pneumatic loads because of

the inability of applied pneumatic loads to change the volume of the vacuum chamber. Since it is desirable for the suction cup to generate a large attachment force, the designs that behaved similarly to Design 2 and Design 3 — which generated attachment forces close to or less than 0 N across all three pneumatic loads — did not meet the needs of our intended applications. For the designs that exhibited behavior similar to that of Design 1, the maximum attachment force was generated at the maximum pneumatic load, enabling us to select the best design from the simulation performed at 16 kPa.

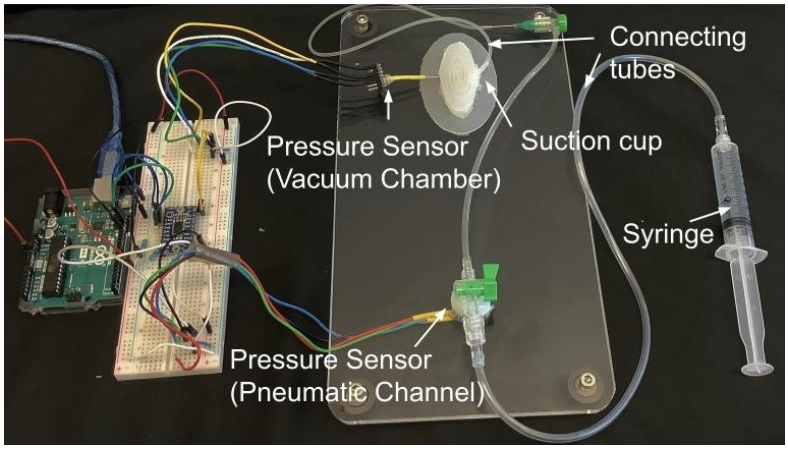
The impact of individual design parameters on the performance can be inferred from the optimization study results shown in Fig. 3.5. It can be seen that the performance improved with larger H2, or larger volume of the spiral channels. Larger values of H1 led to decreased performance, possibly due to the fact that larger values of H1 means it is more difficult for suction cups to bend away from the substrate given smaller heights of other layers. The performance also worsened with larger values of H4, and the effect of H3 is not clearly evident from the results.

The best performing design at a pneumatic load of 16 kPa had an aspect ratio of 2.5, channel width of 1.3 mm, and heights of 1 mm, 4 mm, 1 mm, and 1 mm for H1, H2, H3, and H4, respectively.

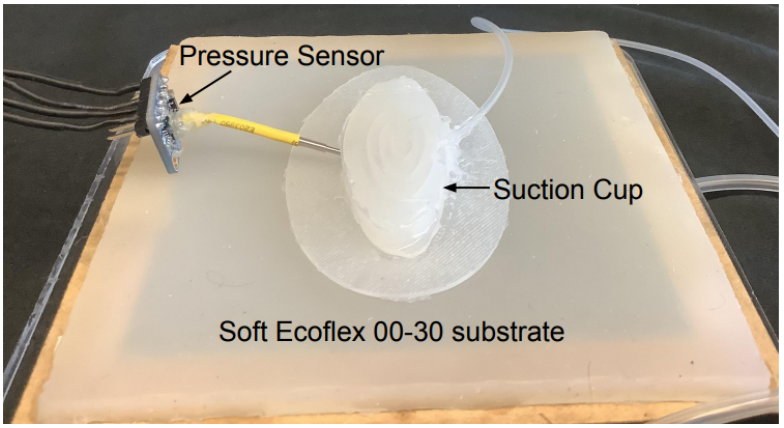
3.3.2 Model Validation on Rigid and Soft Substrates

Experimental evaluations were conducted using the setup shown in Fig. 3.7 in order to measure and compare the performance of the selected suction cup with the developed FEA model. Pressure sensors (Adafruit MRPLS) were used to measure the output pneumatic load in the vacuum chamber and the input pneumatic load, which was manually applied using a 12 mL syringe. This experiment was performed on both acrylic and Ecoflex 00-30. The Ecoflex 00-30 substrate was 120 mm $\times$ 120 mm $\times$ 5 mm and was mounted on an acrylic frame, as shown in Fig. 3.7b.

Three suction cups with the same selected parameters were fabricated, and experiments



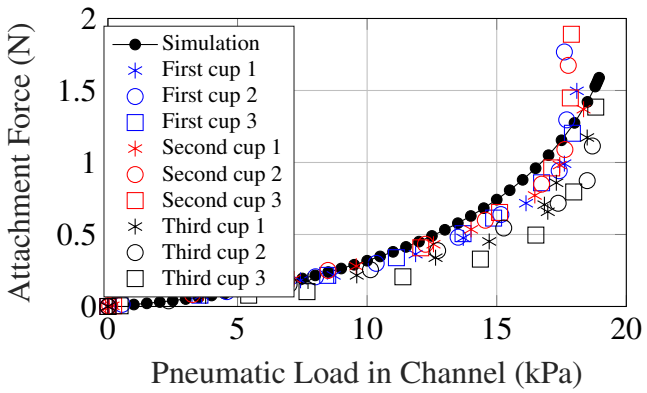
(a)



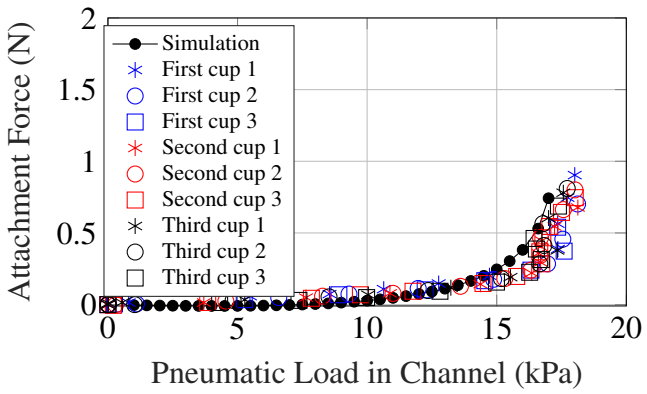
(b)

Figure 3.7. (a) Experimental setup for measuring the suction cup behavior and comparing it to that predicted by the FEA simulations on both rigid and (b) soft substrates.

were repeated three times per substrate for each suction cup. The attachment forces were then calculated based on the measured pneumatic load generated. As seen in Fig. 3.8a and 3.8b, behavior of the fabricated suction cups matched that predicted in the simulation for both the rigid and soft substrates, respectively. Although there were slight differences in behavior among the suction cups, which is expected for structures manually fabricated from soft materials, the general trends remained consistent. The attachment force generated increased almost linearly with an increase in the pneumatic load in the channel until a critical pneumatic load – approximately 17 kPa and 16 kPa for the rigid and soft substrate, respectively – was reached. Beyond this load, there was an exponential increase in the generated force, an excessive



(a)

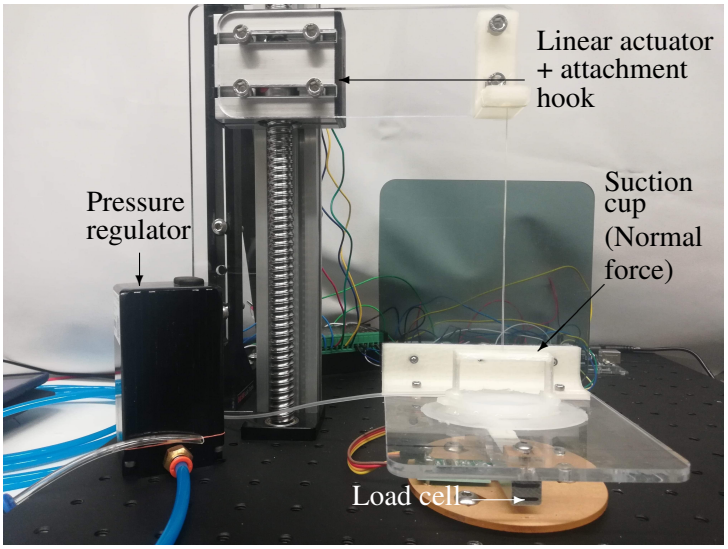


(b)

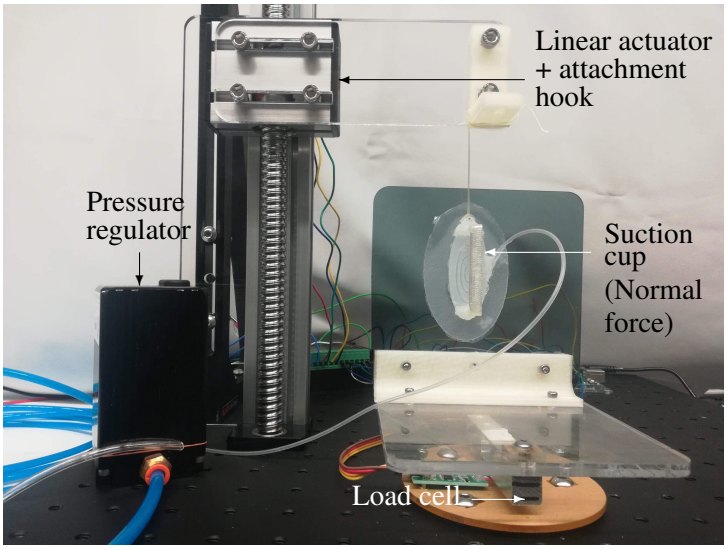
Figure 3.8. Suction cup behavior predicted by FEA simulations versus experimental results for (a) rigid and (b) soft substrates.

ballooning that could lead to structural damage, and an increase in the difficulty to control the generated force.

For the same set of initial conditions, we found that the attachment force generated on the soft substrate was smaller than that on the rigid substrate. This phenomenon can be explained by the decrease in volume in the vacuum chamber that occurs due to the deformation of the soft substrate during suctioning, as shown in Fig. 3.1. It should also be noted that if accurate material properties of tissues were known, the developed model could also be used to predict the behavior and to select the geometry that maximizes the performance on a selected soft tissue.



(a)



(b)

Figure 3.9. Experimental setup for measurement of maximum (a) normal forces and (b) shear forces that the suction cups can resist.

3.3.3 Performance Evaluation With External Loads

The goal of this experiment was to measure the maximum normal and shear forces that the suction cups could resist. As shown in Fig. 3.9, a linear actuator consisting of a stepper motor (Nema 23) and a lead screw was used to pull on the suction cups in a controlled manner. The suction cups were mounted horizontally and vertically for normal (Fig. 3.9a) and shear

(Fig. 3.9b) force measurement, respectively, on both rigid and soft substrates. The pull rate was fixed at 4 mm/s, and the pulling force was measured using a load cell (Makerhawk digital load cell with HX711 ADC module). A pressure regulator (QB1X) was used to control the pneumatic load, which was fixed at 16 kPa. Three experiments for each suction cup were performed and repeated on both the rigid and soft substrates.

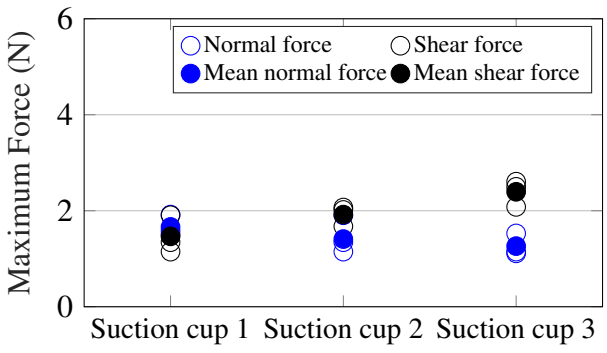
The results for the maximum normal and shear forces that the suction cups could resist are shown in Fig. 3.10. The average peak normal force that the suction cups could resist was 1.45 $\pm$ 0.28 N and 0.77 $\pm$ 0.10 N for the rigid and soft substrates, respectively. It was also observed that the seal between the suction cups and the substrates was easily disturbed when the suction cups were pulled in the normal direction, resulting in their premature failure through detachment.

The shear forces were measured along the direction of the major axis of the oval suction cups. The average peak shear forces that the suction cups could resist was 1.93 $\pm$ 0.48 N and 2.73 $\pm$ 1.02 N for the rigid and soft substrates, respectively. The seal between the suction cups and the substrates was less vulnerable to detachment when under a shear force due to friction.

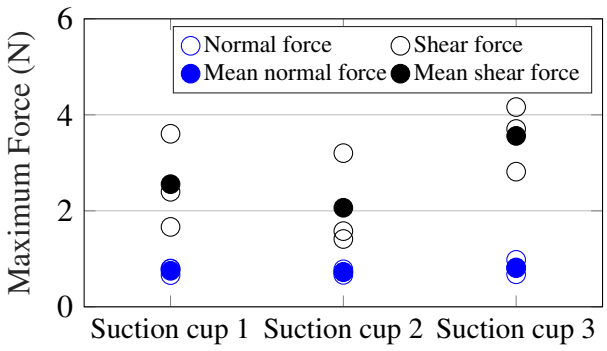
When the suction cups are pulled away from the substrate during the application of external forces (normal and shear), the volume of the vacuum chamber increases beyond the change due to the actuation mechanism itself. This increase in volume continues until the suction cups detach. The larger change in volume results in the suction cups resisting larger external forces than predicted by Eq. 3.2, which gives the attachment force in the absence of external forces.

3.3.4 In-Vivo Demonstration

Finally, the selected suction cup design was tested on live porcine tissues, namely liver and spleen, as a preliminary demonstration towards clinical evaluations. The federal and institutional guidelines for the care and use of laboratory animals were followed (IACUC protocol: S06253). A force gauge (Baoshishan Z-50N) was used to measure the forces that the



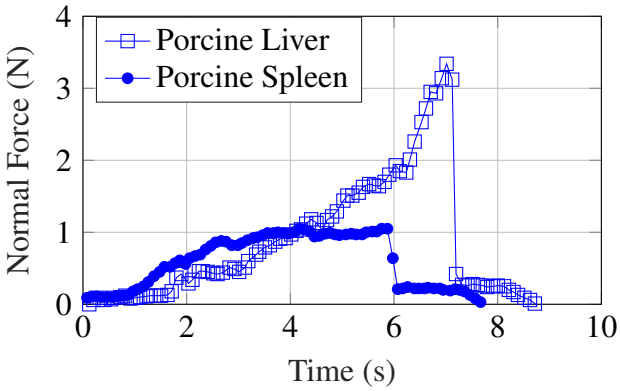
(a)



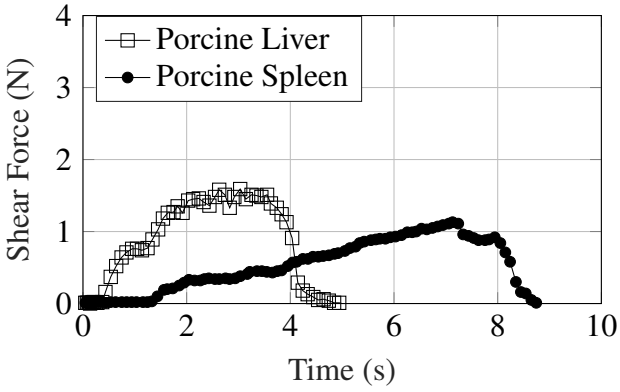
(b)

Figure 3.10. Results showing the maximum normal and shear forces resisted during each trial, along with the mean of these maximum forces, as measured on (a) a rigid substrate and (b) a soft substrate.

suction cup could resist when actuated on the tissues, for both normal and shear forces. As shown in Fig. 3.11, when placed on the liver, the suction cup could resist up to 3.34 N and 1.59 N of normal and shear forces, respectively, without experiencing the ballooning effect. Similarly, when placed on the spleen, it could resist 1.05 N and 1.13 N of normal and shear forces, respectively. The differences in performance between the two tissues may be due to differences in surface and mechanical properties of the tested tissues. For example, differences in the amount of viscous fluid present, the concavity of the tissue, and the stiffness may all play a role, and further study is required to fully characterize the possible phenomena. These preliminary tests on live tissues demonstrate the potential of the proposed positive-pressure



(a)



(b)

Figure 3.11. Results showing (a) normal forces and (b) shear forces the suction cup resisted on porcine tissues.

suction cups for anchoring to tissues during surgical procedures.

3.4 Discussion

In this chapter, an FEA model that enables the simulation of the behavior of positive-pressure actuated suction cups on both rigid and soft substrates was presented. The geometry of a positive-pressure actuated suction cup was optimized using the developed model to maximize its attachment force for use in the target application as a stabilizing unit for flexible surgical tools during surgical procedures. Experiments were conducted to successfully test the validity of the developed model and for assessing the ability of the selected suction cups to resist

external forces. An in-vivo demonstration on live porcine tissues was conducted to showcase the applicability of these suction cups as anchoring units for surgery.

As a continuation of this work, multiple units could be integrated to create a functional soft system to meet the anchoring demands of surgery. Future work could also expand the study on channel designs besides Archimedian spiral and their effects on the suction cup's performance. The suction cup design can also be modified to include features, such as micro patterns and switchable adhesives at the interface between the suction cup and the tissue, which could increase the maximum attachment force by improving the seal. The vacuum chamber design can also be improved to restrict the deformation of soft substrates in the chamber during actuation. Similarly, the effect of lip at the base, which is added to maintain proper seal, on the anchoring force achieved by a suction cup can be further studied. Since deformation of the soft substrate can be correlated to the pressure generated in the vacuum chamber, future research can exploit this ability for studying the material properties of different soft substrates.

3.5 Acknowledgments

This chapter is, in part, a reprint of material from A. Giri, C.Girerd, X. Luo, R. Broderick, and T. Morimoto, *"fModeling and design of soft, positive-pressure actuated suction cups for anchoring in minimally invasive surgery." In 2022 9th IEEE RAS/EMBS International Conference for Biomedical Robotics and Biomechatronics (BioRob), pp. 01-08. IEEE, 2022.* The dissertation author is the primary author of this paper.

Chapter 4

PneuSIC Box: Pneumatic Sequential and Independent Control Box for Scalable Pneumatic Demultiplexing

4.1 Introduction

4.1.1 Background

The inherent compliance of soft robots make them well-suited for a wide range of applications, such as medical robotics, haptics, wearable robotics [1]. Despite the variety of available actuation methods, including magnetic [45], electric [44], and thermal actuation [46, 47], pneumatic actuation largely remains the dominant choice for operating soft robots. Pneumatic actuation offers fast response times, large force output, wide accessibility of required electromechanical components, and the robots remain lightweight [48, 49, 50]. However, the need for a dedicated pressure regulator and associated electro-mechanical components [51] for each actuator makes the pneumatic control system bulky, expensive, and unsuitable for untethered applications. Therefore, simplifying pneumatic control systems for soft robots is crucial for their future commercialization and widespread adoption [43].

4.1.2 Contributions

In this chapter, we introduce PneuSIC Box, a novel pneumatic demultiplexer inspired by the music box. PneuSIC Box operates with just a single pneumatic input paired with a motor to allow independent control of a large number of outputs. Additionally, PneuSIC Box enables simultaneous control of multiple actuators while supporting pneumatic memory retention (i.e. allowing the actuators to retain their pressurization states) without any additional energy. We also introduce and experimentally validate an FEA model for guiding the design of soft kink valves, which represent the fundamental control components of PneuSIC Box.

The chapter is structured as follows. The working principle of the presented system is discussed in Section 4.2. The design of the presented proof-of-concept PneuSIC Box is detailed in Section 4.3. Section 4.4 discusses the FEA model used to estimate behaviors of soft kink valves for PneuSIC Box. In Section 4.5, we present the experimental validation of the FEA model and the results of the device characterization. Finally, in Section 4.6 we showcase the

features and applicability of PneuSIC Box by controlling an inchworm-inspired robot and a robotic hand with soft fingers.

4.2 Working Principle

The working principle of PneuSIC Box is inspired by that of a music box. A music box typically includes a rotating cylinder with rigid bumps arranged in rows and columns along its circumference, as seen in Fig. 4.1(a). A music box also features a column of metal tines that are fixed at their bases. As the inner cylinder rotates, the rigid bumps strike the adjacent metal tines, causing them to vibrate and thereby produce a pre-programmed melody. Similarly, PneuSIC Box consists of an inner rotating cylinder with sets of individual ramps and holes arranged in rows and columns. The inner cylinder is housed within a sealed outer cylinder, which features soft kink valves that are considered to be "open" when air can flow through them. The kink valves are arranged in a single column (similar to the tines in a music box), with a dedicated

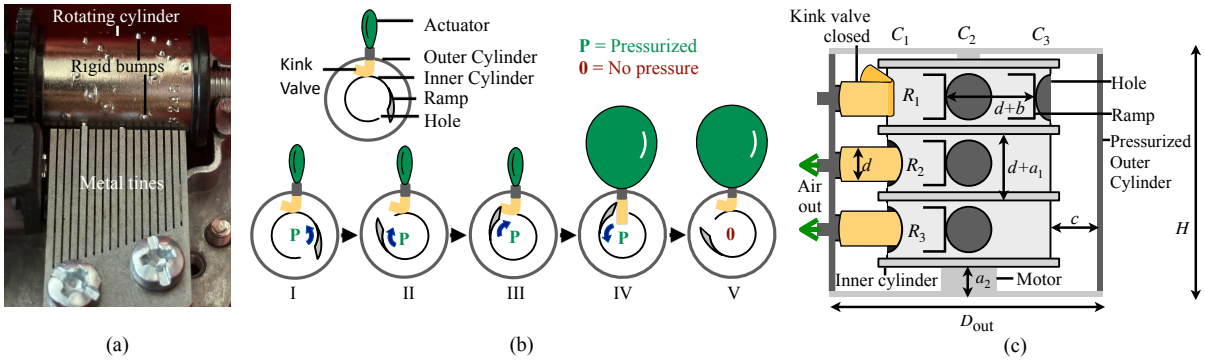


Figure 4.1. (a) The inside of a music box, which inspired the working principle of PneuSIC Box. (b) A schematic showing the top view of a single row of an inner cylinder within a sealed outer cylinder. A closed kink valve prevents airflow to the actuator (I and II). The inner cylinder can be rotated to allow the ramp's flat surface to guide the kink valve into the adjacent hole (III and IV). Air flows to the actuator (IV) when the kink valve is open. Rotating the inner cylinder in the counterclockwise direction can push the kink valve back to its closed state, preventing air from escaping the actuator regardless of the PneuSIC Box's pressure (V). (c) A schematic of a PneuSIC Box with an inner cylinder featuring three rows (R_1, R_2, R_3) and three kink valves inside a pressurized outer cylinder. Three columns (C_1, C_2, C_3) with ramps and holes are visible in the inner cylinder, which can be rotated by a motor at the base to open or close the kink valves.

kink valve for each row in the inner cylinder. When bent, or kinked, at a sharp enough angle, the kink valves are considered to be "closed" and air flow through them is blocked [131]. By controlling the state (open or closed) of a kink valve, pressurization and depressurization of an actuator attached to the fixed end of the kink valve can be controlled.

Figure 4.1(b) shows a schematic representing the top view of a single row of an inner cylinder within a sealed outer cylinder. The depicted inner cylinder contains a single ramp and hole. A closed kink valve attached to the inside of the outer cylinder blocks the airflow to the attached actuator, even if the pressure inside PneuSIC Box increases to P. Similarly, when the inner cylinder is rotated counterclockwise, the kink valve slides over the ramp and remains closed, as shown in Fig. 4.1(b)-II. As a result, the pressure inside the connected actuator remains unchanged. However, when the inner cylinder is rotated clockwise so that the ramp guides the kink valve into the hole, as shown in Fig. 4.1(b)-III, the kink valve opens. As a result, the attached actuator is pressurized, as depicted in Fig. 4.1(b)-IV. Following the pressurization of the actuator, if the inner cylinder is rotated counterclockwise, the kink valve is pushed back to its closed state. Since the kink valve prevents the air from flowing to and from the actuator, changes in pressure inside the outer cylinder do not affect the pressure inside the actuator, as seen in Fig. 4.1(b)-V. The pressure inside the actuator can only be adjusted by changing the pressure within the PneuSIC Box while the kink valve is open.

To control n actuators, n rows are needed in the inner cylinder. Similarly, if the inner cylinder has sets of ramps and holes arranged in m columns, all attached actuators can be independently controlled as long as $m>n$, and n columns feature single sets of ramps and holes. The remaining m-n columns can have multiple sets of ramps and holes, which allow simultaneous control of multiple actuators, as required by the target set of applications. Figure 4.1(c) shows a simplified schematic of PneuSIC Box with an inner cylinder featuring three rows (R_1, R_2, and R_3), three visible columns (C_1, C_2, and C_3), and three kink valves, one dedicated for each row. By aligning the kink valves with C_1 (Fig. 4.1(c)), the bottom two kink valves can be opened

to allow airflow through their respective outlets. In this configuration, the top kink valve stays closed because of the absence of a ramp or hole at R_1. Similarly, if all three kink valves must be opened simultaneously, the kink valves must be aligned with C_2. Finally, the top kink valve can be controlled independently by aligning the kink valves with C_3.

The dimensions of PneuSIC Box, specifically its outer diameter and height, depend on the diameter of the kink valves (d), as well as the parameters m and n. The height of PneuSIC Box, H, can be expressed as $H = n\ (d + a_1) + a_2$, where a_1 is a constant accounting for the clearance between the wall of the hole and the outer diameter of the kink valve, and the gap between holes in adjacent rows. a_2 is the height needed to accommodate the rotating motor. Similarly, a PneuSIC Box's outer diameter, D_{out}, can be simply expressed as $D_{\text{out}} = m\ [(d+b)/\pi] + 2c$. The minimum distance between the walls of two holes in the same row but in adjacent columns is represented by the constant b. Similarly, the constant c represents the sum of the clearance between the inner cylinder and the outer cylinder (designed to accommodate the kink valve in its closed state), and the wall thickness of the outer cylinder (selected to handle the maximum working pressure inside PneuSIC Box).

4.3 Design

Based on the working principle outlined in Section 4.2, we designed and fabricated a proof-of-concept PneuSIC Box (Fig. 5.2(a)) with five kink valves, allowing it to support five outlets. Each kink valve was made using a 25 mm long latex rubber tube with outer and inner diameters of 5.56 mm and 3.18 mm, respectively. The free end of each kink valve was cut at approximately a 20° angle to help it slide easily into the holes when guided by the ramps. The geometry and bend angle of the kink valves were empirically selected to ensure that they could block sufficiently large pressures when closed.

An inner cylinder was 3D printed using polylactic acid (PLA) filament and features a slender cylindrical extension with a 4 mm magnet attached to its tip. The angular position of

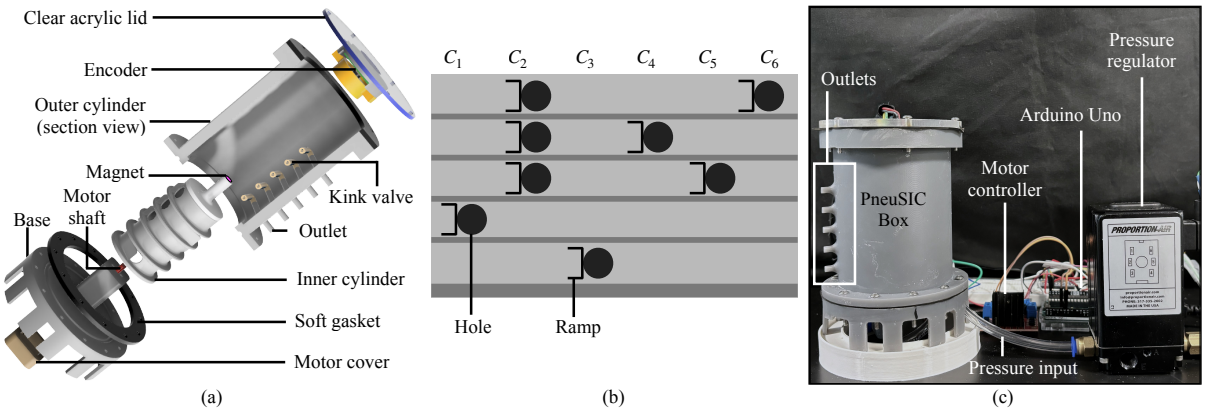


Figure 4.2. (a) Exploded view of the designed PneuSIC Box with all of its components. (b) A schematic of an inner cylinder that has been cut and rolled out, displaying the arrangement of ramps and holes in six distinct columns ($C_1 - C_6$). (c) PneuSIC Box with its supporting electronics, including a micro controller, a motor controller, and a pressure regulator.

the magnet, and thus the inner cylinder, is sensed using an AS56OO absolute encoder, which is secured to the center of a clear acrylic lid. The base of the inner cylinder is attached to the shaft of a Pololu Micro Metal Gear motor (298:1 gear ratio), which is housed inside a 3D printed base. An outer cylinder, with a wall thickness of 5 mm, was 3D printed using FormLabs Grey Pro resin. To complete the assembly, this outer cylinder was securely fastened to both the base and the lid using screws, with soft gaskets sandwiched in between.

Figure 5.2(b) shows a schematic representing the rolled out inner cylinder used in the designed PneuSIC Box. Each hole in the inner cylinder has a diameter of 8 mm, with the ramp height set at 5.56 mm, matching the outer diameter of the kink valve. Sets of ramps and holes are arranged in six evenly spaced columns (C_1 to C_6) and allows for independent control of each of five actuators, while also enabling simultaneous control of three actuators (as demonstrated in Section 4.6.1). Lastly, Fig. 5.2(c) shows PneuSIC Box with its supporting electronics, which include an Arduino Uno and an L298N motor controller for the DC motor. A QBX Series Proportional Air pressure regulator, capable of regulating pressures between 0 psi to 50 psi, served as the only pneumatic input source. The designed PneuSIC Box setup was used for performing experimental characterizations (Section 4.5) and in one of the two presented demonstrations (Section 4.6.1).

4.4 FEA Model of Kink Valves

A kink valve blocks airflow when the inside of its tubular wall presses onto itself at the kinked region, as detailed in [131]. However, a sufficiently large input pressure can deform the

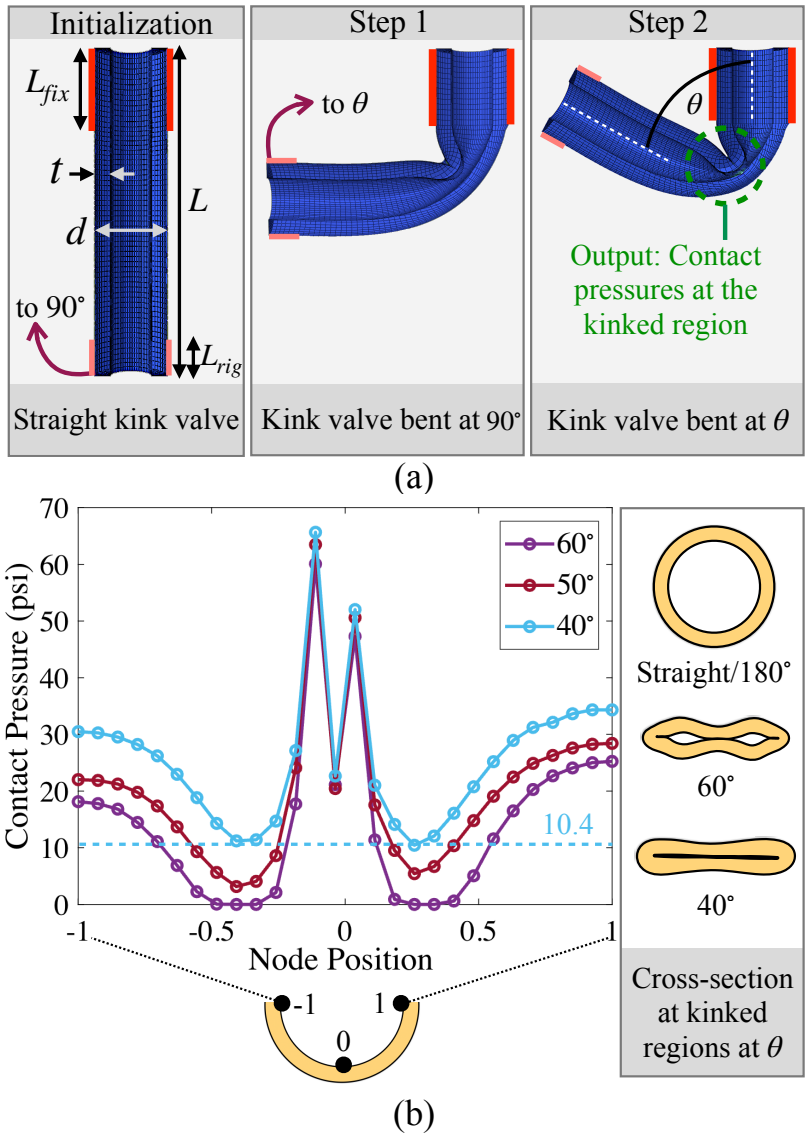


Figure 4.3. (a) The proposed workflow for using the FEA model to predict the breakthrough pressure based on the kink angle for a given kink valve. During the Initialization step, the kink valve's geometry is selected. During Step I, the kink valve is bent to an initial kink angle of 90°. During Step II, the kink valve is bent to its final kink angle (θ), and the contact pressures on the inner surface are recorded. (b) Contact pressures at different positions on the inner surface of the kink valve, along with cross-sectional views of the kinked region at three different kink angles.

material around the kinked region, causing air to leak out. The minimum pressure at which this leakage occurs is called the breakthrough pressure [131], and it represents the maximum pressure PneuSIC Box can support in the attached actuators without leakage. Breakthrough pressure is largely affected by kink valve geometry, material selection, and the angle to which the kink valve is bent. To inform the design of PneuSIC Box and the maximum pressure it can support in the attached actuators, we developed a Finite Element Analysis (FEA) model that estimates the relationship between breakthrough pressures and kink angles for any given kink valve design.

We use Abaqus 2022 to perform a multi-step FEA that starts with defining the geometric parameters of the kink valve to be studied (Fig. 4.3(a)). We use a hyperelastic Yeoh material model with parameters based on the kink valve material. The tube is fixed at its base with a zero displacement boundary condition along the length L_{fix}, which corresponds to the kink valve's attachment length to the outer cylinder. To ensure that an applied tip displacement causes the kink valve to bend rather than locally stretch, a small section (L_{rig}) located at the tip of the kink valve is made rigid. To ensure convergence, the tip is displaced in two steps. In Step 1, the kink valve is bent to 90° by applying a displacement boundary condition to the free end of the rigid part. In Step 2, the kink valve is further displaced until the desired angle (θ) is reached. The kink angle is measured as the angle between the lines passing through the centers of the kink valve's two ends.

As the kink angle decreases, the gap between the inner surfaces at the kinked region gets narrower, resulting in an increase in contact pressure. The model outputs the contact pressure at each node, which represents a corner of each individual mesh element around the kinked region. Since pressures higher than the contact pressure would cause the contact to break, allowing air to flow through, the minimum contact pressure is equal to the breakthrough pressure for that kink angle. This process can be repeated for a range of angles to establish a relationship between the final kink angles and the breakthrough pressures for a given kink valve design.

To understand the behavior of the specific soft kink valves used in PneuSIC Box (Section 4.3), we first designed a corresponding kink valve in Abaqus. The angle cut at the kink valve's tip was not modeled because it did not affect the kink valve's bending behavior. We chose a global mesh size of 0.4 mm using a hexagonal element with 4 elements along the radial direction, and used a sweep meshing technique. In addition, C3D8RH, an eight-node mesh element from the standard element library, with hybrid formulation and reduced integration, was used as the mesh element type for the kink valve, with default settings. The Yeoh parameters ($\mathbf{C}_{10}$ = 0.185164 MPa, $\mathbf{C}_{20}$ = 0.002785 MPa, and $\mathbf{C}_{30}$ = 0.000038 MPa) corresponding to latex rubber [132] were used to simulate the kink valve material. The contact pressures at three example values of θ are plotted in Fig. 4.3(b). At a kink angle of 60°, the contact pressures at the nodes surrounding the center are zero, indicating that the kink valves are not fully closed at this position, as shown in the adjacent schematic. However, as the kink angle was decreased to 40°, the minimum contact pressure, and therefore the breakthrough pressure, increased to 10.4 psi.

4.5 Experiments

In this section we present the experimental characterizations of the designed PneuSIC Box, including: validation of the FEA model, demonstration of pneumatic memory retention in attached actuators, and characterization of the actuation time required for initializing pressurization in any attached actuator.

4.5.1 Model Validation

Figure 4.4(a) shows the setup used for validating the FEA model. The setup consisted of an assembled PneuSIC Box with an overhead camera that had visibility through the clear lid. An example image showing the camera view of the top kink valve is shown in Fig. 4.4(a). Since only the top kink valve was visible, the other kink valves were removed, and their corresponding

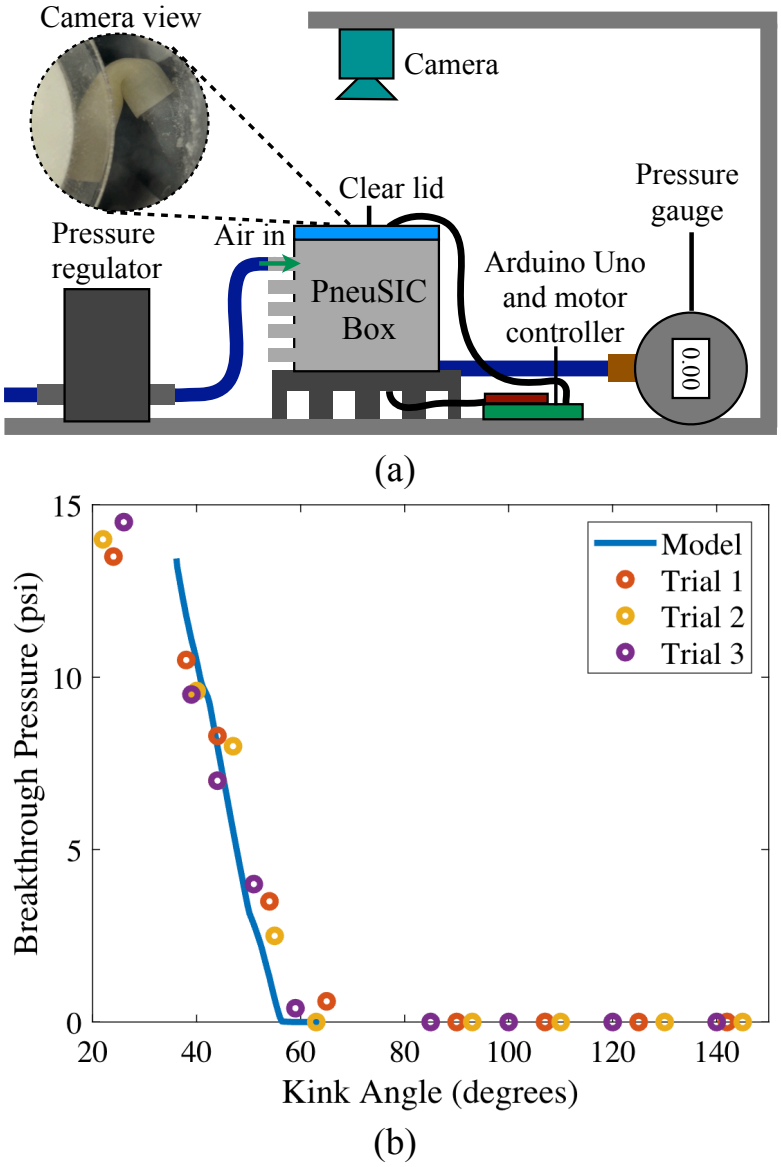


Figure 4.4. (a) Experimental setup for validating the FEA model. The setup includes an overhead camera to capture the angle of the top kink valve, which is connected to a pressure regulator at its outlet. A digital pressure regulator is connected to the inlet of the PneuSIC Box. (b) Experimentally observed breakthrough pressure versus kink angle behavior closely matches the predictions from the FEA model.

outlets were sealed. A pressure regulator supplied a known air pressure to the top outlet, simulating an attached pressurized actuator. Finally, a digital pressure gauge (SSI Technologies Inc., MGA-30-A-9V-R) was connected to PneuSIC Box's inlet.

During the experiment, the inner cylinder was first positioned so that the kink valve

was guided into a hole at an angle of approximately 140°, the largest possible angle without the kink valve falling out. The kink angle was measured using screenshots from the recorded video as the angle between the straight center lines drawn through the tip and base of the kink valve. The kink angle was then gradually decreased by changing the angular position of the inner cylinder in 10° increments until the kink valve was positioned over the ramp. At each kink angle, the supplied pressure was increased in 0.1 psi increments until the pressure gauge showed a positive reading greater than the smallest measurable pressure of 0.01 psi, indicating airflow through the kink valve. The pressure at which this reading was obtained was recorded as the breakthrough pressure for that kink angle. This process was repeated three times. The experimentally measured results, along with the model-predicted breakthrough pressures, are presented in Fig. 4.4(b).

The observed relationship between breakthrough pressures and kink angles closely matched the predictions of the FEA model, as seen in Fig. 4.4(b). The FEA model could not predict the breakthrough pressures for kink angles smaller than 36° due to convergence issues. However, it can be inferred that the breakthrough pressures at the smallest observed kink angles slightly deviated from the path of the predicted linear relationship. This may be due to differences in boundary conditions in the FEA model compared to the actual scenario when the kink valve ascends the ramp. Nonetheless, the results validate the method for modeling kink angle behavior. As seen in Fig. 4.4(b), the kink valve began to block airflow at kink angles smaller than 60°. Around a kink angle of 40°s, the angle at which the kink valve rests on the inner cylinder, the breakthrough pressure was found to average 9.8 psi, closely matching the estimated 10.4 psi. Thus, any connected actuator in the designed PneuSIC Box can accommodate a maximum pressure of around 9.8 psi without leakage through the kink valve. This information informed the selection of actuators used in the demonstrations presented in Section 4.6.

4.5.2 Actuation Time

The pressurization or depressurization of any subset of actuators is accomplished by rotating the inner cylinder to align the kink valves with the correct column. The time required to initiate control of these actuators depends on the angular distance to be rotated and the speed of the motor. To characterize the actuation time for the designed inner cylinder, the kink valves were first aligned with column C_1 (Fig. 5.2(b)). The inner cylinder was then rotated to align the kink valves with the target column. Once aligned, the inner cylinder was rotated in the opposite direction to open the targeted kink valves. The time was recorded, and this process was repeated three times for each target column from C_2 to C_6.

Figure 4.5 shows that the time required for the kink valves to open at any target column is dependent on the angular distance between that column and the kink valves. As expected, a relatively linear relationship was observed between angular distance travelled and required time, with the time to complete the process for the farthest column averaging 1.60 seconds. The time required to align any column in the inner cylinder with the kink valves was largely

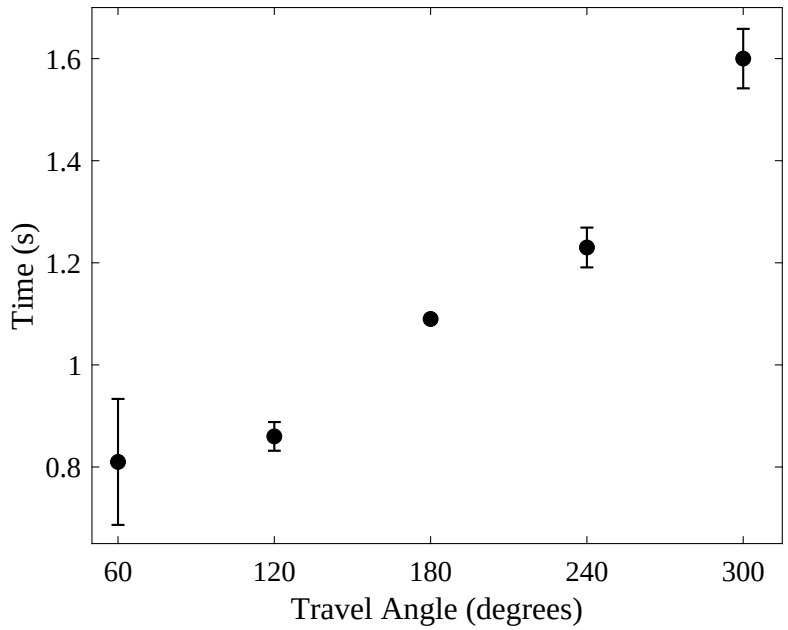


Figure 4.5. The mean and standard deviation of the time required for rotating the inner cylinder to align each of its columns with the kink valves and open them.

determined by the motor speed, which was reduced due to friction between the kink valves and the inner cylinder, and by the angular distance between two subsequent columns in the inner cylinder. Therefore, the time needed to initiate control of the target actuators could be improved by selecting a motor with higher speed and greater torque capability, or by reducing the size of gaps between subsequent columns.

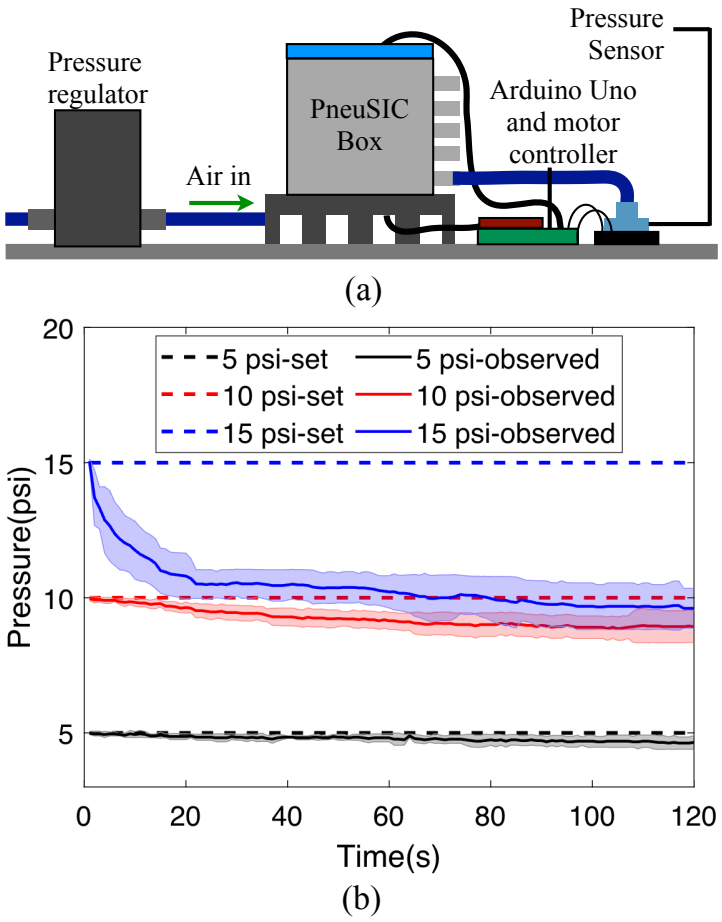


Figure 4.6. (a) Experimental setup used for measuring the memory retention capabilities. The setup includes a pressure regulator connected to the inlet of PneuSIC Box and a pressure sensor connected to an outlet. (b) At set pressures of 5 psi and 10 psi, the pressure readings remain fairly stable with minimal decay over 120 s. At a set pressure of 15 psi, the readings initially drop sharply to the breakthrough pressure before stabilizing with slight decay thereafter.

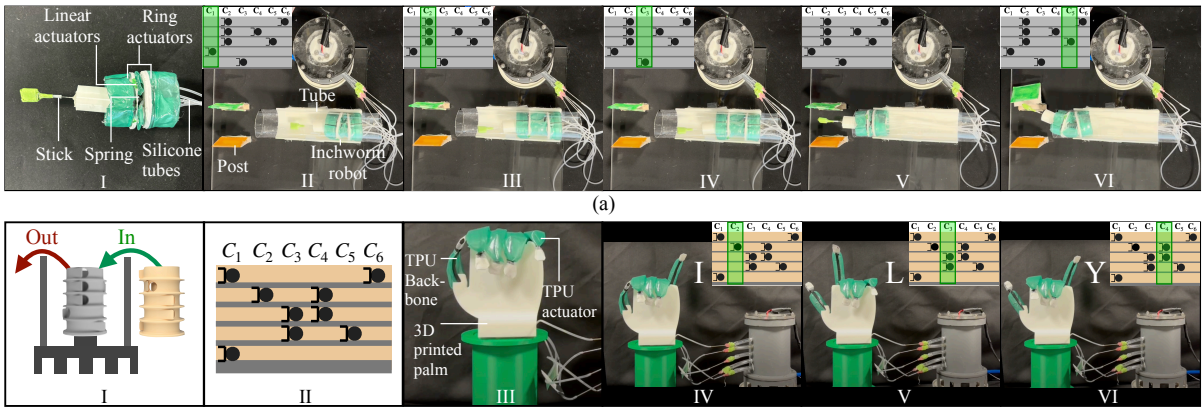


Figure 4.7. (a) Demonstration of PneuSIC Box controling an inchworm-inspired robot (I). The robot starts at the base of a clear tube (II). PneuSIC Box enables inchworm-like movement by first pressurizing the bottom ring actuator (III), followed by the linear actuators (IV), and then the top ring actuator, in sequence, until the robot reaches the end of the tube (V). Subsequently, one of the three linear actuators is pressurized to steer the robot to strike a randomly selected post (VI). (b) PneuSIC Box controls a mock hand with soft fingers. For this demonstration, a new inner cylinder (I) with a revised arrangement of ramps and holes (II) is used. PneuSIC Box allows the mock hand (III) to form the characters "I" (IV), "L" (V), and "Y" (VI) in American Sign Language, sequentially.

4.5.3 Pneumatic Memory Retention

PneuSIC Box can actively control pressures in target actuators, while other actuators retain their pneumatic memory without external energy or input. This ability enables the presented demultiplexer to operate with a single pneumatic input. To experimentally validate the device's pneumatic memory retention capability, the setup shown in Fig. 4.6(a) was used. A proportional air pressure regulator (QBX series, 0 psi-50 psi) was connected to the inlet of the PneuSIC Box, and a Tru-Stability pressure sensor was used to record the pressures at each outlet (one at a time). For each trial, the inner cylinder was first rotated open the kink valve. The pressure inside PneuSIC Box was then set to a desired value, and the inner cylinder was rotated to close the kink valve. The pressure inside PneuSIC Box was then reduced to zero, and the resulting pressure was recorded for the next 120 seconds. The process was repeated for 5 psi, 10 psi, and 15 psi, where 10 psi approximately equalled the breakthrough pressure and 15 psi was known to be above the breakthrough pressure. Five trials were conducted for each pressure,

with the pressure sensor connected to a different outlet for each trial.

As seen in the Fig. 4.6(b), the pressure readings remained fairly consistent, with a minor, steady pressure decay for the set pressures of 5 psi and 10 psi. After 120 seconds, the average readings decreased to 92.8% and 88.8% of the set pressures for 5 psi and 10 psi, respectively. As expected, at 15 psi the pressure first dropped to an average of 10.53 psi, matching closely with the kink valve's estimated breakthrough pressure of 10.4 psi. Subsequently, it decreased steadily to 9.61 psi (91.3% of 10.53 psi) by the end of 120 seconds. The observed small and steady pressure decay likely stemmed from minor leaks in the experimental setup, specifically at the connection interfaces between PneuSIC Box and the pressure sensor. We note that any pressure loss over a long period can be compensated with closed-loop control of the actuators. However, the observed pneumatic memory retention is expected to be sufficient for most soft robots, including the two demonstrated in Section VI, as they do not require the actuators to hold pressure for extended durations.

4.6 Demonstrations

In this section, we demonstrate the ability of PneuSIC Box to actuate soft robots with multiple actuators using only one pneumatic input and a motor. In our first demonstration, the designed PneuSIC Box is used to control a soft inchworm-inspired robot, highlighting its ability to execute a pre-programmed gait sequence, pneumatic memory retention of the attached actuators, independent control of any actuator during its operation, and regulation of pressure in the actuators. In the second demonstration, the designed PneuSIC Box is used to control five soft fingers in a mock hand, highlighting the interchangeability of the inner cylinder to enable simultaneous control of a new set of actuators.

4.6.1 Inchworm Robot

PneuSIC Box was first used to control a soft inchworm-inspired robot, referred to as the Inchworm (Fig. 4.7(a)-I), which resembles other soft inchworm-inspired robots designed for minimally invasive surgical applications [133, 34]. The inchworm was positioned at one end of a tube, selected to represent a tubular environment, such as a pipe or the colon. PneuSIC Box was then used to control pressures in the Inchworm's five actuators. PneuSIC Box first facilitated the robot's translation through the tube, using an inchworm-like gait. It then enabled the Inchworm to steer and strike a randomly selected target (orange or green post).

The Inchworm was fabricated using five thermoplastic polyurethane (TPU) actuators arranged around a 3D printed structure. Two of these actuators are ring-shaped, wrapping around 3D printed cylinders at the top and bottom of the robot. When pressurized, these ring actuators expand radially and anchor the robot inside the tubular environment. Sandwiched between the the ring actuators are three equally spaced TPU linear actuators. Simultaneous actuation of all three linear actuators results in the Inchworm's elongation, while actuation of a subset of the three linear actuators allows steering. At the center of the three linear actuators is a stainless steel spring that restores the Inchworm to its original length when actuators are depressurized. Finally, a thin stick with a 3D printed cylindrical base is attached to the Inchworm's tip.

The robot's inchworm-like gait begins by pressurizing the bottom ring actuator, corresponding to kink valves in C_1, to 8 psi. The three linear actuators are then simultaneously pressurized (kink valves in C_2) at 6 psi, while the bottom ring actuator retains its pneumatic memory, ensuring forward elongation (Fig. 4.7(a)-IV). Subsequently, the top ring actuator is pressurized at 8 psi (kink valves in C_2). All actuators are then depressurized in sequence by aligning the kink valves with C_1, C_2, and C_3 in the inner cylinder, with pressure reduced to zero inside PneuSIC Box. Sequential repetition of this gait results in the Inchworm traversing the length of the clear tube (see Fig. 4.7(a)-V). The Inchworm's forward motion was made possible by the ability of PneuSIC Box to control the sequential actuation of the actuators and to retain

pneumatic memory.

After the Inchworm reached the end of the clear tube, a simple MATLAB program randomly selected the green post to be knocked over. The linear actuator responsible for steering the Inchworm towards the green post was then commanded on-the-fly to be pressurized at 6 psi (kink valves in C_5), causing the green post to be struck down (Fig. 4.7(a)-VI). The pressurization of a random linear actuator successfully demonstrated the PneuSIC Box's ability to control any individual actuator in real-time during operation.

4.6.2 Mock Hand for American Sign Language

In American Sign Language (ASL), accurately displaying characters can require simultaneous positioning of multiple fingers into their correct configurations. We fabricated a mock hand with soft fingers that was designed to display "I", "L", "Y", an abbreviation for "I Love You." The mock hand, as shown in Fig. 4.7(b)-III, consisted of two main components: a rigid palm and a set of soft fingers. The palm was 3D printed using PLA, while each of the five fingers was made from a soft TPU actuator with a curved rigid backbone, 3D printed using TPU. When pressurized, each TPU actuator inflates into a straight cylinder, simulating the raising of a finger. The rigid backbone ensures that the fingers return to their curved positions when depressurized. In addition, the original inner cylinder of PneuSIC Box was replaced with the one shown in Fig. 4.7(b)-I and Fig. 4.7(b)-II, customized for this demonstration. The new inner cylinder was specifically designed with columns that enable simultaneous pressurization of multiple fingers necessary to display the characters "I", "L", and "Y".

The new inner cylinder was sequentially rotated to align the kink valves with columns C_2, C_3, and C_4, in that order. For each step in the sequence, the pressure in PneuSIC Box was increased to 4 psi for 5 seconds before being depressurized, allowing the mock hand to sequentially display the target characters (Fig. 4.7(b)). This demonstration successfully highlighted a key feature of PneuSIC Box: the ability to easily swap the inner cylinder to enable simultaneous control of new sets of actuators.

4.7 Discussion

PneuSIC Box is a novel pneumatic demultiplexer that enables independent control of multiple actuators using just one pneumatic input paired with a motor. We presented and validated an FEA model of the soft kink valves, a key-component of PneuSIC Box, that can be used to guide the design for target applications. Furthermore, we characterized the pneumatic memory retention and the dependency of actuation time on the angular position of the kink valves with respect to the target column in the inner cylinder. Finally, we demonstrated the ability of PneuSIC Box to control an inchworm-inspired robot and a robotic hand with soft fingers.

In addition to the many desirable features of PneuSIC Box, we also note a few properties inherent to its architecture. First, while PneuSIC Box can theoretically control an unlimited number of pneumatic outputs, achieving independent control of a large number of actuators would require increasing its size and weight, which could pose practical challenges. Furthermore, using a single pressure source prevents simultaneously controlled actuators from acquiring different pressures. Additionally, PneuSIC Box's rigid construction makes it unsuitable for applications requiring a fully soft system. Finally, to make PneuSIC Box extremely compact, for instance for untethered applications, the kink valves would need to be scaled down, reducing the flow rate and slowing any attached robot. Several limitations could be addressed through design improvements. For instance, custom-designed kink valves with small diameters and optimized cross-sections could achieve high breakthrough pressures at any given kink angle. Such custom kink valves could significantly reduce the size of PneuSIC Box while greatly increasing the number of outlets. Additionally, enhancing the manufacturing process could make the device lighter and more robust. Further studies could also explore the operation of PneuSIC Box using vacuum pressure or using other working fluids. These advancements would further enhance the ability of PneuSIC Box to control numerous actuators with a single input and enable lightweight, untethered operation.

4.8 Acknowledgments

This chapter is, in part, a reprint of material from A. Giri, A.Rivas, R. Yeerella, S. Cai, and T. Morimoto, *"PneuSIC Box: Pneumatic Sequential and Independent Control Box for Scalable Demultiplexing"* The source material has been submitted for publication. The dissertation author is the primary author of this paper.

Chapter 5

Hapstick: A Soft Flexible Joystick for Stiffness Rendering via Fiber Jamming

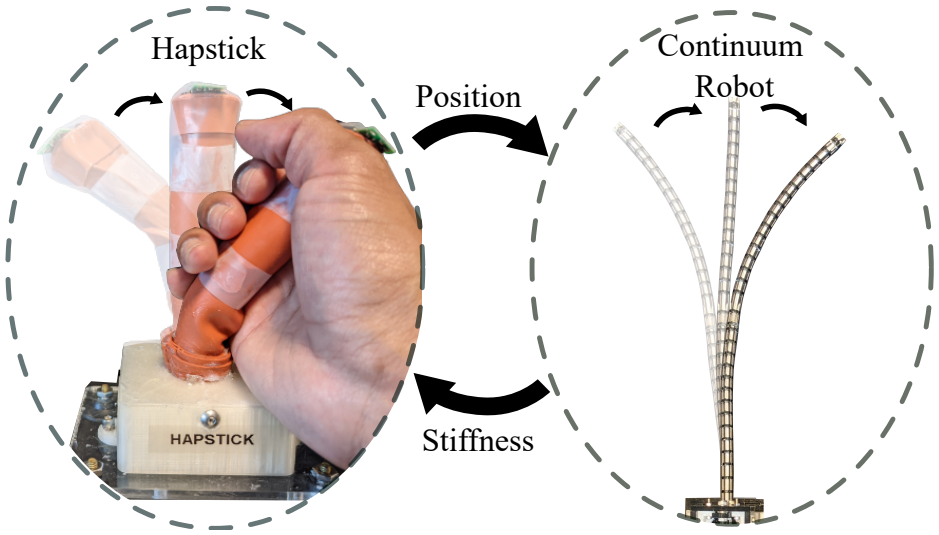


Figure 5.1. Hapstick (left) is used to teleoperate a continuum robot (right). Hapstick acts as the leader device and its configuration, i.e curvature and angle of the plane containing the curvature, is directly mapped to that of the robot's distal segment. Hapstick can also display information about the stiffness of the robot's environment to the users by modulating its stiffness via fiber jamming.

5.1 Introduction

5.1.1 Background

Continuum robots are long, slender robots that can adjust their shape at any point along their length, similar to octopus tentacles and elephant trunks [134]. These robots offer many potential benefits for applications in highly sensitive and constrained environments, such as minimally invasive surgery, due to their inherent compliance and ability to navigate through curved paths [135]. These robots are typically controlled using a human-in-the-loop teleoperation scheme. However, the degree-of-freedom mismatch and kinematic dissimilarity between conventional input devices and continuum robots can result in less intuitive control [136] and introduce the need for complex mappings between the input devices and teleoperated robots [99]. In addition, many input devices lack the ability to provide users with haptic feedback, which can make certain tasks, such as tissue palpation, particularly difficult.

5.1.2 Contributions

In this work, we present Hapstick (Fig. 5.1) — a soft, flexible haptic interface based on fiber jamming and designed to render stiffness information to users teleoperating a continuum robot. Jamming is a method of stiffening a system comprised of an external membrane and fillers, by collapsing the membrane onto the fillers, thereby increasing the density of the entire system [137]. To date, jamming-based interfaces have been shown to be lightweight, have low inertia, and provide passive stability [138]. Although various types of jamming materials have been proposed, in order for an input interface to be kinematically similar to continuum robots, it must be slender in structure. Granular jamming based slender structures cannot withstand large flexural loads [139], preventing them from acquiring configurations similar to flexible continuum robots. Similarly, layer jamming-based devices can only be bent in the direction perpendicular to the sheets, which limits such devices to allowing motion and generating forces in just a single direction [140]. Unlike granular jamming and layer jamming-based devices, fiber jamming-based interfaces can be bent in any direction and can also withstand large flexural loads [139]. While previous works ([139] and [141]) performed detailed analyses of fiber jamming technology, these studies mostly focused on material selection, modeling, and design optimization. The ability of fiber jamming-based devices to provide haptic feedback in the form of tunable stiffness has yet to be explored.

The contributions of this work are as follows. (1) Hapstick is the first fiber jamming-based input interface that can provide tunable stiffness feedback to the user. In addition to the ability to provide haptic feedback in any direction, the fiber jamming mechanism also allows Hapstick to have a kinematically similar structure to continuum robots, enabling potentially more intuitive control. (2) We present results showing the effect of the number of fibers on the ability of the device to provide uniform feedback to the users, as well as results characterizing the relationship between the applied vacuum load and the device stiffness. (3) We present a detailed user study performed to measure the just noticeable difference (JND) in the stiffness information

that the users can perceive while using Hapstick. (4) We demonstrate Hapstick's applicability as a bidirectional interface with tunable stiffness for teleoperating a tendon-driven continuum robot in order to identify tumor positions and their development stages during colorectal cancer screening. Overall, Hapstick demonstrates the potential of jamming-based mechanisms as novel input interfaces that can provide effective haptic feedback to users.

5.2 System Design

In this section, we detail the working principles of Hapstick as a stiffness rendering device and as an input interface. We then present its design, fabrication, and overall workflow.

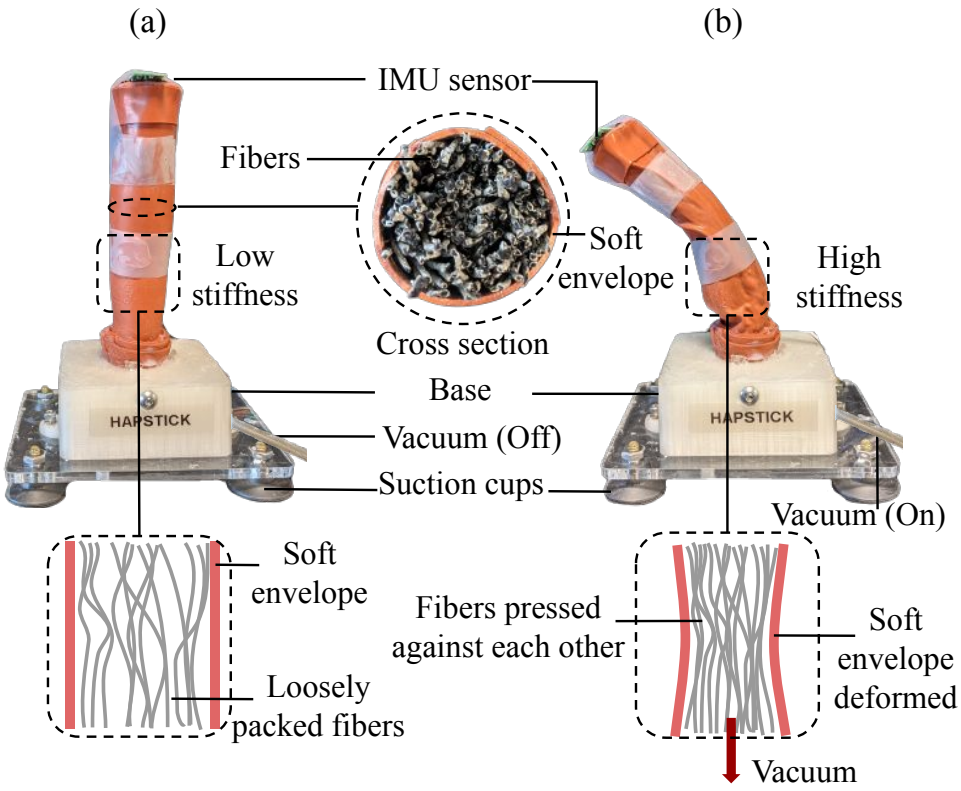


Figure 5.2. Hapstick consists of a soft tubular envelope filled with flexible fibers and can be bent in any direction like a joystick. (a) When no vacuum load is applied, the fibers are loosely packed, and Hapstick is in a low stiffness state. (b) When a vacuum load is applied, the fibers are pressed tightly against each other, and the stiffness of Hapstick increases.

5.2.1 Working Principle

Hapstick is a fiber jamming-based device. Like other fiber jamming mechanisms, it consists of a soft tubular envelope that encloses flexible fibers that have a high coefficient of friction during mutual contact [141, 139]. When a vacuum load is applied inside Hapstick, its soft tube deforms inwards. The deformation compresses the fibers in the radial direction as shown in Fig 5.2, resulting in an increase in the friction force between the fibers. This increase in the friction force causes the fiber jamming-based structure to stiffen [139], and the resultant stiffness is dependent on the applied vacuum load. Users hold Hapstick with a power grip and as they bend it, they can feel the changes in Hapstick's stiffness as the vacuum levels are varied.

5.2.2 Design and Fabrication

Hapstick consists of a soft silicone sheet enveloping a set of abrasive, infill fibers. The silicone sheet is 0.80 mm thick and is first rolled into a tube with an outer diameter of 25 mm and a height of 110 mm. The outer diameter was selected to ensure it was within the range recommended for ergonomic cylindrical handles [142], and the height allows Hapstick to be comfortably bent into a single curve. A known number of abrasive fibers are then filled inside the silicone tube, running along the entire length. Mitchell abrasive fibers (aluminum oxide 180 grit, 0.76 mm diameter) are selected since they have previously been shown to provide a large flexural stiffness to slender structures when subjected to large vacuum loads [139]. The two open ends of the joystick are then sealed with circular silicone discs using a silicone adhesive (Smooth-on Sil-poxy). Hapstick's fabricated body is then inserted 10 mm into a 3D printed base that is rigidly attached to a rectangular acrylic sheet. The acrylic sheet has four suction cups, which help stabilize the setup. Finally, a tube is routed through the 3D-printed base and attached to the bottom of Hapstick to supply the fiber jamming-based device with a vacuum load. An IMU (Pololu MinIMU-9 v5) sensor is then mounted on top of the fabricated Hapstick and is used to map Hapstick's tip orientation to the teleoperated robot's configuration as detailed in

the subsequent section. A Proportional Air (QBX Series) vacuum regulator, which is capable of regulating 0 kPa to -100 kPa, is used to provide the vacuum load to Hapstick. An Arduino Uno and a computer are used to control both Hapstick's input and feedback capabilities. Fig 5.2 shows a fabricated and assembled Hapstick in the unjammed and jammed states.

5.2.3 System Workflow

The overall system workflow is illustrated in Fig 5.3a. Without any vacuum load, Hapstick has a low bending stiffness. It can therefore be easily bent in any direction to mimic a segment of a continuum robot, physical or virtual. When a user bends Hapstick, Euler angles representing the tip orientation can be tracked using the IMU. Assuming constant curvature bending, the orientation information can be converted into the curvature (κ_H) and the angle of the plane containing the curvature (ϕ_H) [143], as shown in Fig 5.3b, in order to obtain its configuration.

Hapstick's configuration is then mapped to the desired configuration of a follower continuum robot as follows: $\kappa_R = \alpha\kappa_H$ and $\phi_R = \phi_H$, where κ_R is the distal segment of the continuum robot, α is a scaling factor selected to accommodate for length differences between Hapstick and the robot, and ϕ_R is the angle of the plane containing the robot's curvature. Alternative mappings for coupling Hapstick with other continuum robots, such as tip extending

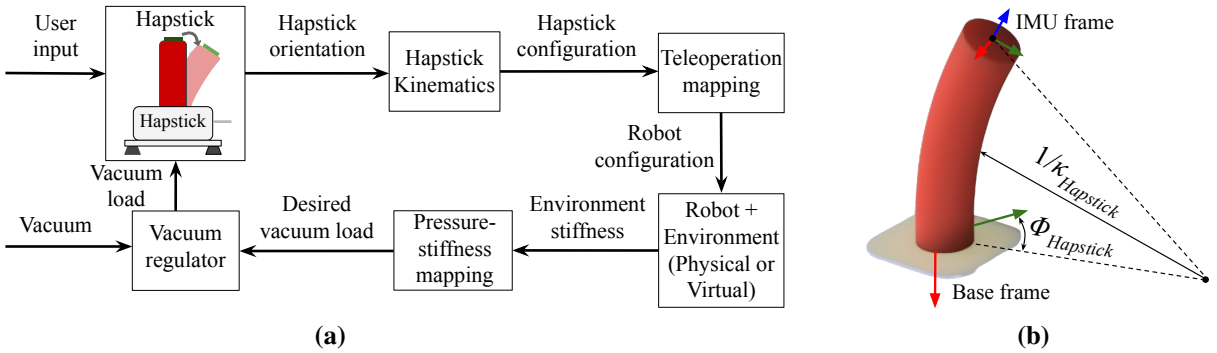


Figure 5.3. (a) Schematic showing the workflow for teleoperating a robot and rendering stiffness feedback using Hapstick. (b) Schematic of Hapstick in a bent configuration with the geometric parameters, κ_H and ϕ_H, used in the employed mapping technique.

robots and concentric tube robots, can be explored.

Based on the interaction — physical or virtual — of the teleoperated robot with the environment, stiffness information can then be conveyed to the user via Hapstick. This stiffness information can be obtained using robots that are equipped with sensors capable of measuring stiffness [144], or by robots operating within virtual environments [145]. The vacuum load required for Hapstick to achieve the desired stiffness is obtained using results from Section 5.3.2. This desired vacuum load is fed into the vacuum regulator as a digital signal, and the regulator then controls the vacuum load being drawn from Hapstick. Hapstick's stiffness varies depending on the level of vacuum being drawn, resulting in changes in its ability to resist motion. The user can perceive the stiffness of the environment through this resistance to motion, which is analogous to the resistance experienced by the teleoperated robot when interacting with the environment.

5.3 Device Characterization

The range of stiffnesses that Hapstick can achieve is dependent on its physical design parameters (i.e. diameter, fiber material, number of fibers, etc.) and the applied vacuum load. In this section, the effect of the number of fibers on Hapstick's mechanical behavior, specifically the force versus deflection behavior during bending, is presented. The results of the study help to inform the number of fibers required to provide uniform stiffness feedback to the users regardless of Hapstick configuration. In addition, the relationship between the applied vacuum and the resulting stiffness of the final Hapstick design is characterized in order to facilitate the design of controllers and haptic rendering algorithms. It should be noted that although fiber-jamming based structures have been shown to have motion hysteresis in their force versus deflection behavior [141], only loading (and not unloading) conditions are considered for the following experiments and characterization, based on previous studies [146] and [147]. These studies have shown that humans may detect stiffness during only the pushing motion, which

corresponds to the loading of Hapstick.

5.3.1 Effects of Fiber Number

It has been shown that the fibers in fiber jamming-based structures, similar to Hapstick, experience slipping with respect to each other when subjected to large deflections. This phenomenon occurs because of the inability of the friction forces between the fibers to hold their relative motion [141]. Using cantilever loading, a force versus deflection curve can be generated and its slope can be measured to observe the slipping transition [141, 139]. After the slipping transition, the slope of this curve decreases, which causes the stiffness of the bent fiber jamming-based structure to significantly drop when deflected further [139]. It is also to be noted that when a fiber jamming-based structure is subjected to a smaller vacuum load, the slipping transition occurs at a smaller deflection [139].

For a given vacuum load, Hapstick would ideally be able to render uniform stiffness to the users regardless of its configuration, i.e. its state of deflection. The desired uniformity in rendered stiffness can be achieved by minimizing the effects of the slipping transition between the fibers for a large range of deflections, even at small vacuum loads. In [139], the FEA-based

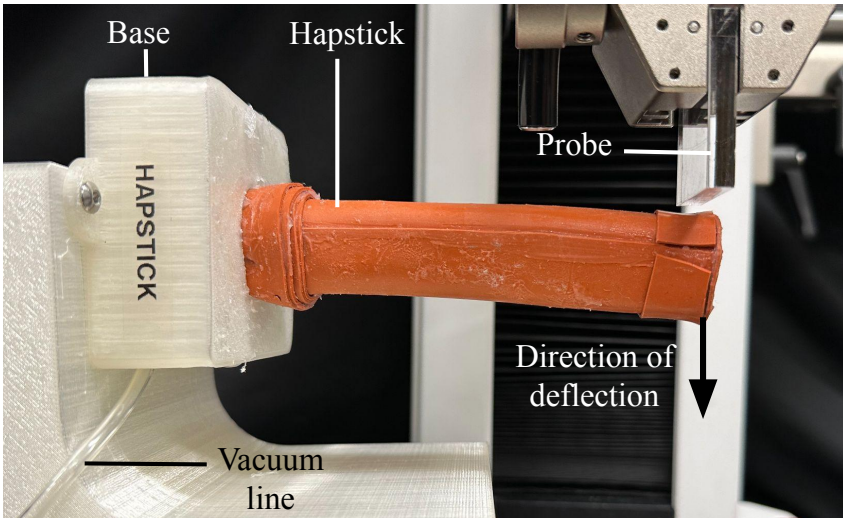


Figure 5.4. Hapstick in a cantilever beam configuration for the characterization study of its force versus deflection behavior.

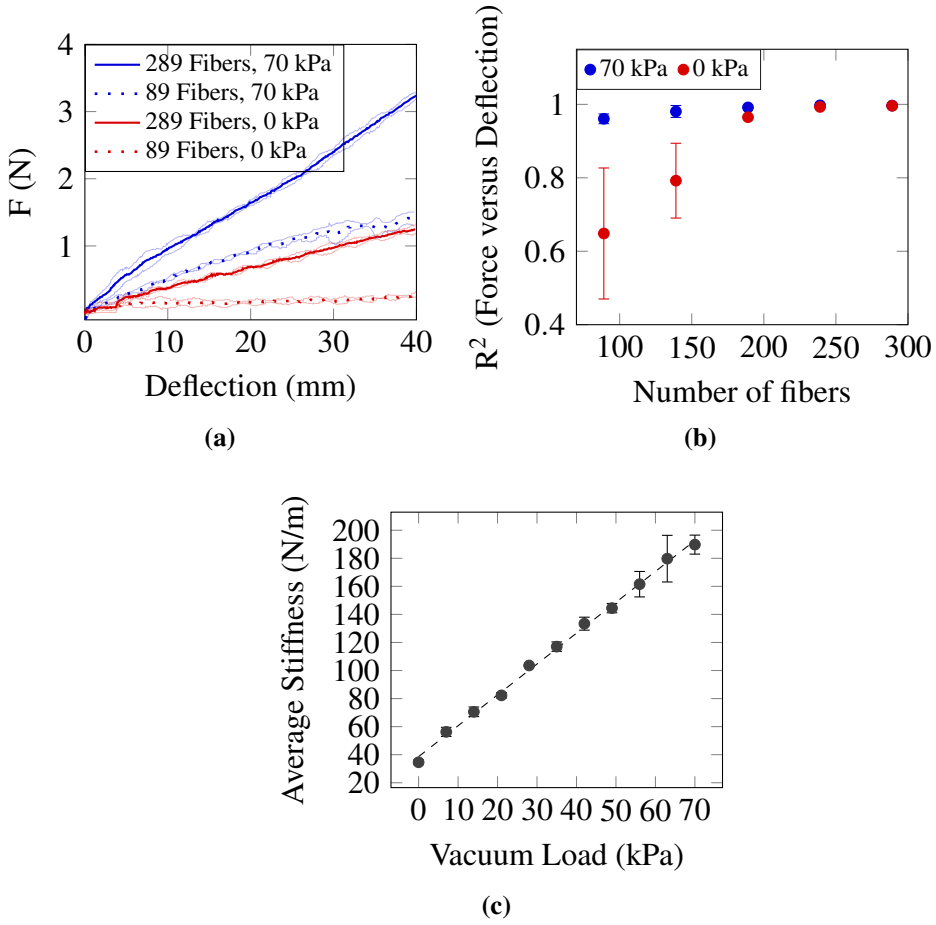


Figure 5.5. (a) Force versus deflection plots with their standard deviations generated for Hapstick with the largest and the smallest studied number of fibers, 289 and 89 respectively, at a large vacuum load (70 kPa) and no vacuum load (0 kPa). For Hapstick with 289 fibers, the slopes of the obtained plots are consistent for tip deflections between 0 mm and 40 mm.(b) Average R^2 values calculated from the obtained force versus deflection plots for Hapsticks with different numbers of fibers at the vacuum loads of 70 kPa and 0 KPa. R^2 values generally increased with the increase in the number of fibers. (c) The obtained linear relationship between the applied vacuum load and average Hapstick stiffness for the final Hapstick design with 289 fibers.

model that is presented to predict the force required for the slipping transition suggests that by sufficiently increasing the area moment of inertia of a fiber jamming structure, its slipping transitions can be avoided for large deflections. One way to increase the area moment of inertia of a fiber jamming-based structure of a given dimension is to increase the number of equally dimensioned fibers.

In this study, we perform an experiment to find the number of fibers required to obtain a

linear force versus deflection curve, which signals minimal slipping, at least up to the studied maximum deflection. Five different amounts of fibers — namely 89, 139, 189, 239, and 289 fibers — were studied under two vacuum loads, 0 kPa and 70 kPa. The largest number of fibers used in the study represents the maximum possible number of fibers that could fit inside the soft silicone envelope. Similarly, 70 kPa was the largest vacuum load that could be obtained using the vacuum pump employed in this study. A Mark-10 tensile tester with an acrylic probe was used to deflect the tip of Hapstick, which was positioned in a cantilever beam configuration as seen in Fig 5.4. Cantilever loading is a simple representation of the loading case that Hapstick is subjected to during its usage. Hapstick was deflected up to 40 mm, which is the largest deflection at which the probe consistently remained in contact with the Hapstick tip, at the rate of 2 mm/s. The forces and deflections measured using the tensile tester were recorded, and the corresponding force versus deflection curves, such as those in Fig 5.5a, were generated. Three trials were run for each fiber count at each vacuum load.

Fig 5.5b shows the results of the average R^2 values observed in the generated force versus deflection plots. The force versus deflection curves for Hapsticks with the studied number of fibers were fairly linear when Hapsticks were subjected to large vacuum loads. However, for Hapsticks without any vacuum load, the linearity of the force versus deflection plots substantially improved with an increase in the number of fibers. The pre-stretch in the soft envelope, when filled with a large number of fibers, may have contributed to the linear force-deflection behavior, even without any vacuum load. At the largest studied number of fibers, the R^2 values for the force versus deflection plots at both 0 kPa and 70 kPa were ~ 0.99. Therefore, when the number of fibers in the designed Hapstick is maintained at 289, the slipping transition has negligible effects on Hapstick's stiffness for up to at least 40 mm of tip deflection for any vacuum load between 0 kPa and 70 kPa. We note that one downside of using a larger number of fibers is that the base stiffness of Hapstick (i.e the stiffness when the vacuum load is absent) is increased, meaning that the lowest stiffness value that can be rendered is also increased. Ultimately, we

selected to use the maximum number of fibers in the final design to ensure that, for a given vacuum load, it can display uniform stiffness to the users regardless of its configuration.

5.3.2 Stiffness Characterization

After fabricating a Hapstick with 289 fibers, we performed an experiment using the same setup as that used in Section 5.3.1 to calculate the stiffness of the final Hapstick design when it is subjected to vacuum loads of 0 kPa to 70 kPa in step sizes of 7 kPa. The goal of the study was to characterize the physical stiffnesses that the fabricated Hapstick can acquire when different vacuum loads are applied. An established relationship between Hapstick stiffness and applied vacuum load can facilitate the design of appropriate haptic rendering algorithms and controllers. Three trials were run at each vacuum load, and the resulting stiffness values were calculated by measuring the slopes generated from the obtained force versus deflection plots. In order to respect the criteria of force acting perpendicularly at the tip of the cantilever beam during the measurements, deflections up to only 8.75 mm, which corresponds to the deflection angle of 5°, were considered during these stiffness calculations. The mean stiffness values and standard deviations are plotted in Fig 5.5c for each vacuum load. A linear relationship is observed between the Hapstick stiffness (K_{H}) and the applied vacuum load (P) as given by:

$$K_{\mathrm{H}} = 2.20 \cdot P + 38.63. \tag{5.1}$$

Stiffnesses corresponding to any vacuum loads between 0 kPa and 70 kPa can be interpolated using the obtained relationship, given by Eq. (5.1). Based on these results, the Hapstick stiffness when no vacuum load is applied is 38.63 N/m and the stiffness measured at the vacuum load of 70 kPa is 192.63 N/m. Therefore, the maximum jamming ratio, defined as the stiffness at the maximum vacuum load divided by the stiffness when no vacuum load is applied, is 4.99.

5.4 Psychophysical Study and Stiffness Perception

A psychophysical experiment was conducted to obtain the just noticeable difference (JND) in stiffness that users can perceive using Hapstick, given any reference stiffness. Measurements were obtained from users bending Hapstick in leftward and rightward directions to observe potential differences in user perception when using the device during pronation and supination of the wrist. This experimentally obtained JND for the chosen reference stimulus is used to compute the constant Weber Fraction (WF). According to Weber's Law, the WF is a constant ratio between the JND and a reference input stimulus [148]. The linear relationship given by the WF thus allows for estimating the JND for any reference stiffnesses displayed by Hapstick (i.e. JND $=$ WF $\times K_{\text{ref}}$).

5.4.1 Participants

Twelve participants aged 18-29 were recruited for the study (6 female and 6 male). Out of the twelve users, eleven were right-hand-dominant, and five reported having had prior experience with haptic devices. All participants gave informed consent, and the experiment was approved by the University of California, San Diego, Institutional Review Board.

5.4.2 Methods

To obtain the JND at a reference stimulus, the method of constant stimuli was used, whereby a set of comparison stimuli are compared against a reference stimulus [149]. A two-alternative forced-choice (2AFC) procedure was used, where users responded yes or no to the question "was the second stiffness greater than the first stiffness?"

Before beginning the study, all participants were trained on how to interact with Hapstick. Users were instructed to grasp the device using a power grip and were asked to displace it left or right until it stiffened. Once the device stiffened, users were instructed to palpate the stiffened Hapstick within a 20 mm region, in order to simulate a tissue palpation task. All participants

were given 2 minutes to familiarize themselves with the device. They then completed a training session that consisted of 14 trials that were conducted identically to those in the actual study, except that they were notified of the correct response after each training trial.

During each trial, participants stood in front of Hapstick and were provided with a sequence of instructions via the Arduino serial monitor. Users were required to center Hapstick for 3 seconds, then were instructed to bend the device either left or right. After bending Hapstick such that its tip was displaced more than 20 mm, a reference stiffness of 104.8 N/m (corresponding to 30 kPa applied vacuum load) was provided. Users were given 5 seconds to palpate the device in order to perceive its stiffness. After palpating, users were instructed to return Hapstick back to its center for 3 seconds. Subjects then repeated the above sequence but were instead given one of the following comparison stiffness values: 60.7, 82.7, 104.7, 126.8, 148.8, 170.9, or 192.9 N/m. The order and direction in which these comparison stimuli were provided were randomly pre-generated and presented to all users. All participants performed 70 total trials, 5 times per comparison stimulus in leftward and rightward directions. Users recorded their responses into the Arduino serial monitor by entering "y" to indicate that the second stimulus was stiffer than the first, or "n" otherwise. Additionally, participants wore

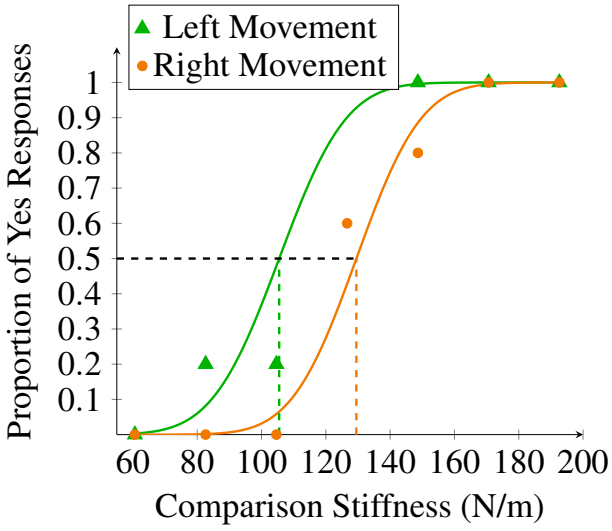


Figure 5.6. Representative psychometric curves obtained for one participant for movement in both the left and right directions.

active noise-canceling headphones playing white noise in order to prevent them from hearing any relative difference in noise generated by the vacuum regulator.

5.4.3 Results and Discussion

Representative psychometric curves are shown in Fig. 5.6 for leftward and rightward movement. These curves were generated using the Psignifit toolbox for MATLAB [150]. The toolbox plots the proportion of "yes" responses against the corresponding comparison stiffness values and fits a psychometric curve to the data points. The point of subjective equality (PSE) (i.e. the comparison value that over a large number of trials is perceived by users to be equivalent to the reference [149]), along with the 25th and 75th percentile comparison values, are obtained from the psychometric curve. The JND is computed using the PSE as well as the 25th and 75th percentile comparison values (P_{25} and P_{75}) as follows:

$$\text{JND} = \frac{(P_{75} - \text{PSE}) + (\text{PSE} - P_{25})}{2}. \tag{5.2}$$

The Weber Fraction is estimated using the empirically determined JND and PSE measures as follows:

$$\text{WF} = \frac{\text{JND}}{\text{PSE}}. \tag{5.3}$$

A summary of the experimental results is shown in Table 5.1. An outlier detection test was used to identify anomalies in the psychometric data, which can often occur in psychophysical studies due to the study design or instruction, or due to participants becoming bored or fatigued [151]. The method used to identify these outliers was S_n [152], as it was shown to be suitable for detecting outliers in data obtained from psychometric experiments [151]. The method was performed on the PSE values because these measurements provide an indication of the constant error, or the error between what users perceive to be the reference stimulus and the true reference stimulus [149]. Out of the twelve initial users, three users were classified as outliers. Psychophysical studies relating to haptic perception tend to be lengthy [149], and it

is suspected that the lengthy nature of this study caused these users to become fatigued or to become distracted.

Given a reference input stimulus of 104.75 N/m, the average JND was 64.1 N/m for leftward movement and 59.8 N/m for rightward movement. The Weber Fractions obtained for leftward and rightward movements were 51.6% and 55.9%, respectively. Although previous studies have shown that WFs related to stiffness discrimination typically range from 15-28% [153, 154], studies investigating the WF for the moment of inertia have shown significantly higher values, ranging from 10-113% [155] [156]. Given that the stimuli provided by Hapstick involve changes in both the stiffness and moment of inertia, the resulting WFs seem reasonable.

User responses were taken for movements in leftward and rightward bending directions to observe potential differences in stiffness perception. A Shapiro-Wilk test (5% significance level) was used to verify that the PSE measurements in both directions were normally distributed.

Table 5.1. Summary of results obtained from the performed psychophysical study for a reference stimulus of 104.63 N/m.

	Left Movement			Right Movement		
	PSE	JND	WF	PSE	JND	WF
Subject	(N/m)	(N/m)	(%)	(N/m)	(N/m)	(%)
1	105.6	49.7	47.1	129.7	49.4	38.1
2	120.4	70.8	58.9	136.4	77.5	56.8
3	134.6	70.7	52.5	119.8	72.9	60.9
4	114.7	50.5	44.0	90.3	47.3	52.4
5	143.5	95.1	66.3	95.0	79.7	83.9
6	120.6	46.8	38.8	93.7	46.2	49.3
7	129.0	59.6	46.2	103.7	49.7	47.9
8	96.4	64.5	66.9	91.4	63.4	69.4
9	159.0	69.0	43.4	116.9	51.8	44.3
Mean	124.9	64.1	51.6	108.5	59.8	55.9
STD	19.2	14.9	10.3	17.6	13.7	14.0

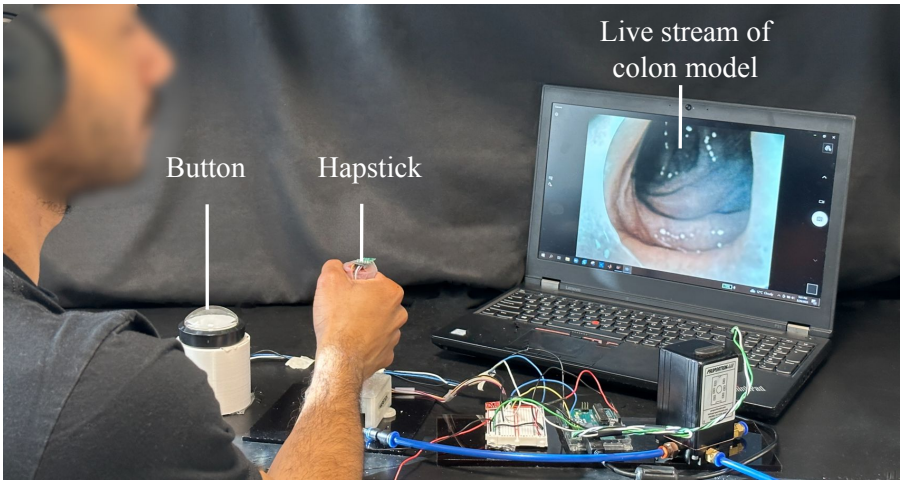
A two-sample t-test (5% significance level) revealed that there was no statistical difference in PSE measurements for the leftward and rightward movement. This result implies that users are able to perceive the stiffnesses generated by Hapstick equivalently in both directions.

5.5 Demonstrated Tumor Identification Task and Results

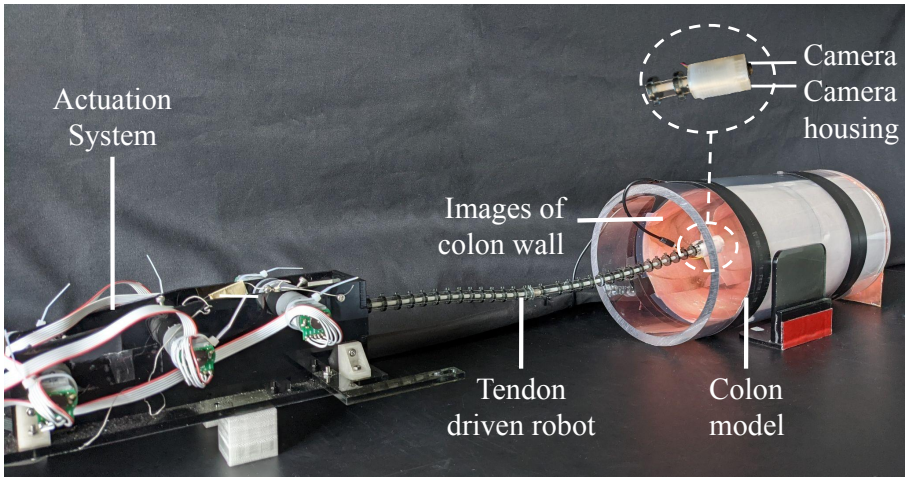
In this section, we demonstrate the ability of Hapstick to be used as a haptic interface for teleoperating a continuum robot and its ability to provide tunable stiffness feedback in multiple directions. We focus here on colorectal cancer screening, where the inside of the colon tissue is palpated to identify cancerous tissues, which are stiffer than their non-cancerous counterparts [157]. In particular, users are asked to identify three development stages of colon tumors, namely T2, T3, and T4, since their correct evaluation influences surgical and therapeutic approaches taken for treatment of colorectal cancer [158].

5.5.1 Setup

Users sit facing Hapstick and are asked to wear noise-canceling headphones. Their interactions with Hapstick are measured and mapped to the movements of a two-segment tendon-driven robot. κ_H is mapped to κ_R after being scaled by a factor of 0.2 and ϕ_H is mapped directly to ϕ_R, as described in Section 5.2.3. The robot is centered inside an acrylic tube, designed to mimic a section of a colon. The colon model itself is lined with images of the colon wall, however, cancerous tissues cannot be visually identified. When the robot's tip position, computed using the forward-kinematics, coincides with the known position of the wall of the colon model, Hapstick's stiffness is changed based on the tissue to be rendered in that region. In the future, a probe with a force sensor, such as the one presented in [144], could be attached at the tip of the follower continuum robot for real-time tissue stiffness measurement. Finally, an Accfly Mini Pinhole 3.6 mm camera is mounted to the tip of the robot and is used to capture real-time video inside the colon model during the task. The setup consisting of the robot and



(a)



(b)

Figure 5.7. (a) During a simulated colorectal cancer screening task, the surgeon-side interface consists of Hapstick and a screen for viewing real-time video streaming from a camera at the tip of the robot. (b) The patient-side setup consists of a tendon-driven continuum robot inside a colon model.

colon model shown in Fig 5.7b is hidden from the user, who can only view Hapstick, the button, and the video stream as shown in Fig 5.7a.

5.5.2 Procedure and Results

Three right-handed users, who were all previously trained to use Hapstick (either through pilot studies or the previously described JND study) were recruited for this demonstration. The participants were trained to identify the three studied tumor stages and to teleoperate the tendon-

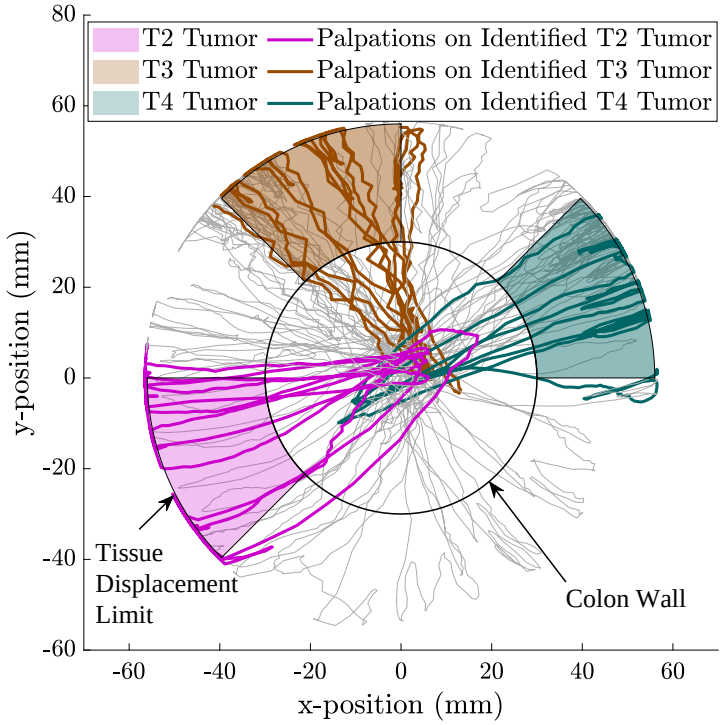


Figure 5.8. A representative trajectory of the tendon-driven robot's tip over one trial. Grey lines indicate the trajectory of the robot's tip during exploratory palpations, and colored lines show the trajectory as the robot palpates on identified tumors, for the duration the button is pressed.

driven robot, whose tip motion could be observed via real-time video displayed on the computer screen. Regions representing T2, T3, and T4 tumors were randomly positioned, with the only constraints being that there should not be tumor regions directly adjacent to one another and each tumor should span a 45° interval, as shown in Fig. 5.8. The stiffnesses displayed by Hapstick for the cancerous tumors are selected such that they fall within the range of stiffnesses that can be displayed by the final Hapstick design, as described in Section 5.3.2. These stiffness values are proportional to the median elastic moduli of the cancerous tumors at the given development stages, as presented in [157]. The stiffness values displayed by Hapstick for T2, T3, and T4 tumors are therefore 44 N/m, 113 N/m, and 177 N/m, respectively. For non-cancerous tissue regions, stiffness was not actively displayed, and users simply felt Hapstick's implicit stiffness of 38.63 N/m.

During the task, users were told to first palpate the tendon-driven robot clockwise

around the circumference of the entire model. Users were then allowed to freely explore the environment to identity the tumor regions and the corresponding development stages. Once users were ready to report their responses, they were instructed to palpate clockwise around the colon model as before, and to press and hold a button in the regions where they encountered a tumor. As users entered into these regions, they were also instructed to verbally report whether they were feeling a T2, T3, or T4 tumor. It should be noted that the robot's tip could not actually move past the colon model's rigid wall, due to the physical constraint. However, the user could still use Hapstick to teleoperate a virtual representation of the robot tip up until the tissue displacement limit, shown in Fig 5.8, to simulate pushing against a deformable tissue.

Three users performed three trials of the task. A representative trajectory of the tendon-driven robot's tip position over one trial is shown in Fig. 5.8. Participants were able to successfully identify the position and the development stage of the cancerous tumors with 92.6% accuracy (i.e 25 out of 27 responses were correct) using the stiffness feedback displayed by Hapstick. One user misidentified T3 as T4, and vice versa. This can be attributed to the JND being larger for larger stiffnesses corresponding to T3 and T4 tumors, as determined by the WF. Despite the small difference in stiffnesses between T2 tumors and non-cancerous tissue, T2 tumors were correctly identified in all trials. The cutaneous feedback resulting from deformation of the soft envelope, along with kinesthetic feedback, could have potentially aided this distinction.

5.6 Discussion

In this chapter, we proposed and characterized Hapstick, a flexible input device that can provide tunable stiffness feedback via fiber jamming. We found that by increasing the number of fibers, Hapstick could display a more uniform stiffness feedback even at small vacuum loads and large deflections. Hapstick's final design exhibited a linear relationship between the achieved stiffnesses and the applied vacuum loads. The final Hapstick design can acquire any

stiffness between 38.63 N/m and 192.63 N/m. Users' ability to perceive the stiffnesses that can be displayed by Hapstick was also characterized in the Just Noticeable Difference (JND) study. The average Weber Fraction (WF) was found to be 51.9% $\pm$ 10.3% during the leftward movement and 55.9% $\pm$ 14.0% during the rightward movement. JND at any reference stimulus can be calculated using the obtained WF. Finally, the applicability of Hapstick for teleoperating a tendon-driven robot for colorectal cancer screening was demonstrated. Users could correctly identify the cancerous regions along with their development stages with 92.6% accuracy.

As a continuation of this work, improvements in the device design, along with extensions to the performed studies, can be completed to further enhance Hapstick's capabilities. For example, given that the abrasive coating on the fibers can wear off after repeated usage, the device durability can be characterized and possibly improved. Future work can include the investigation of alternative fibers that enable fiber jamming-based devices to attain large stiffnesses even after repeated usage. Similarly, Hapstick's design can be refined to be more ergonomic in order to enable ease of motion regardless of the bending direction. As an extension of the performed psychophysical study, the JND can also be characterized for directions other than the already studied left and right directions. Finally, future studies can investigate the effectiveness of novel mapping techniques for teleoperating other types of continuum robots for a range of applications. Overall, Hapstick has illustrated the potential of jamming-based mechanisms as bidirectional interfaces capable of providing effective haptic feedback.

5.7 Acknowledgements

This chapter is, in part, a reprint of material from A. Giri*, R.Bloom*, and T. Morimoto, *"Hapstick: A Soft Flexible Joystick for Stiffness Rendering via Fiber Jamming. IEEE Robotics and Automation Letters, 8(7), 4163-4170."* The dissertation author contributed equally to this paper, alongside R. Bloom.

Chapter 6

Conclusions

6.1 Summary

This dissertation introduced four novel robotic systems designed to address the challenges of using soft robots in minimally invasive surgeries (MIS). Chapter 2 introduced the InchIGRAB, a novel soft robot designed to enable steering and retraction of vine robots, or growing robots, for colonoscopy. The chapter detailed the design, modeling, fabrication, and experiments showcasing the robot's capabilities. The presented system was demonstrated to successfully traverse the entire length of the colon during both forward motion and retraction, while minimizing interaction with the delicate colon environment. Therefore, the InchIGRAB has the potential to facilitate safe colonoscopy by minimizing the normal and shear forces exerted by the vine robot on the delicate colon environment. Similarly, Chapter 3 presented an FEA model and the design of a positive pressure suction cup, developed to anchor soft and flexible robots during MIS applications. The designed suction cup was demonstrated to be capable of resisting over 3 N of normal force and more than 1.5 N of shear force on in-vivo porcine tissues. The anchoring capability of the presented positive pressure suction cup can enable soft continuum robots to perform tasks like tissue manipulation, where exerting significant forces at the robot's distal end is essential. Chapter 4 introduced PneuSIC Box, a novel pneumatic demultiplexer inspired by the working principle of a music box. PneuSIC Box enabled independent control of multiple pneumatic actuators using just a single pneumatic input and a motor. PneuSIC Box was demonstrated to control an inchworm-inspired robot, similar to the InchIGRAB, as well as a soft robotic hand. The presented pneumatic demultiplexer greatly simplifies the control hardware for pneumatically actuated soft robots, including those used in minimally invasive surgical applications. Finally, Chapter 5 presented the Hapstick, a soft and intuitive joystick that was kinematically similar to a single-section soft continuum robot. The Hapstick was also able to convey stiffness information about the teleoperated robot's environment using fiber jamming. In addition, the Hapstick was demonstrated to allow users to identify the position and stage of cancerous tumors during a mock colorectal cancer screening task. Therefore, the Hapstick

presents an approach to enable intuitive control of soft continuum robots during MIS, while conveying useful information about the surgical environment to surgeons.

6.2 Future Work

As a direct continuation of the work presented in this dissertation, robust sensing and control methods need to be integrated to enable closed-loop control of the presented systems. The integration of appropriate sensors that can monitor the states of the InchIGRAB and the surrounding colon environment could enable the InchIGRAB to operate effectively within a colon in-vivo without prior knowledge of the environment. The use of pressure sensors for closed-loop control would also allow the positive-pressure suction cup to provide consistent anchoring forces during operation. Similarly, closed-loop control of the pressures in the actuators attached to the PneuSIC Box would enable these actuators to precisely reach and maintain the target pressures. Additionally, the Hapstick would benefit from closed-loop control of its vacuum load, allowing it to consistently maintain the target stiffnesses. Subsequently, the mechanisms presented in Chapters 2 through Chapter 5 could be integrated to develop a comprehensive soft robotic system for MIS applications. Such a comprehensive robotic system could provide patients with enhanced safety through a soft surgical robot actuated using simplified control hardware, along with offering surgeons intuitive control of the robot.

6.3 Broader Impact

This dissertation addressed several often-overlooked challenges, including the design of soft robots based on anatomical and procedural needs of the taget MIS application, stabilizing soft robots during tasks such as tissue manipulation, simplifying the control hardware for complex pneumatically actuated soft robots proposed for MIS, and developing intuitive input interfaces for controlling these robots. The presented approaches, combined with advancements in well-established areas of soft robotics such as control and sensing, manufacturing, actuation,

and material science, can help fully realize the potential of soft robots for MIS applications.

Furthermore, although the robot described in Chapter 2 was specifically designed for colonoscopy, a similar design approach — one that carefully considers anatomical and procedural requirements — could be adapted for other MIS applications, such as bronchoscopy and endoscopy. The positive-pressure suction cup, PneuSIC Box, and Hapstick would need only minor modifications to be suited for different MIS procedures. Additionally, PneuSIC Box and the Hapstick, with only minor modifications, are also capable of enabling the operation of general soft robots and continuum robots, respectively.

Overall, we hope the methods and approaches presented in this dissertation will inspire new ideas that will propel efforts to advance soft robots for MIS applications and enable safer and simpler surgical procedures.

ACKNOWLEDGEMENTS

Chapter 2 is, in part, a reprint of material from A. Giri, C. Girerd, J. Cervera-Torralba, M.T. Tolley, and T.K. Morimoto, *"InchIGRAB: An Inchworm-Inspired Guided Retraction and Bending Device for Vine Robots during Colonoscopy."* The material has been submitted for publication. The dissertation author is the primary author of this paper.

Chapter 3 is, in part, a reprint of material from A. Giri, C.Girerd, X. Luo, R. Broderick, and T.K. Morimoto, *"Modeling and design of soft, positive-pressure actuated suction cups for anchoring in minimally invasive surgery." In 2022 9th IEEE RAS/EMBS International Conference for Biomedical Robotics and Biomechatronics (BioRob), pp. 01-08. IEEE, 2022.* The dissertation author is the primary author of this paper.

Chapter 4 is, in part, a reprint of material from A. Giri, A.Rivas, R. Yeerella, S. Cai, and T.K. Morimoto, *"PneuSIC Box: Pneumatic Sequential and Independent Control Box for Scalable Demultiplexing"* The material has been submitted for publication. The dissertation author is the primary author of this paper.

Chapter 5 is, in part, a reprint of material from A. Giri*, R. Bloom*, and T.K. Morimoto, *"Hapstick: A Soft Flexible Joystick for Stiffness Rendering via Fiber Jamming. IEEE Robotics and Automation Letters, 8(7), 4163-4170."* The dissertation author contributed equally to this paper, alongside R. Bloom.

Bibliography

[1] Daniela Rus and Michael T Tolley. Design, fabrication and control of soft robots. *Nature*, 521(7553):467–475, 2015.

[2] Hongbo Wang, Massimo Totaro, and Lucia Beccai. Toward perceptive soft robots: Progress and challenges. *Advanced Science*, 5(9):1800541, 2018.

[3] Chidanand Hegde, Jiangtao Su, Joel Ming Rui Tan, Ke He, Xiaodong Chen, and Shlomo Magdassi. Sensing in soft robotics. *ACS nano*, 17(16):15277–15307, 2023.

[4] Pinar Boyraz, Gundula Runge, and Annika Raatz. An overview of novel actuators for soft robotics. In *Actuators*, volume 7, page 48. MDPI, 2018.

[5] Meng Li, Aniket Pal, Amirreza Aghakhani, Abdon Pena-Francesch, and Metin Sitti. Soft actuators for real-world applications. *Nature Reviews Materials*, 7(3):235–249, 2022.

[6] Lindsey Hines, Kirstin Petersen, Guo Zhan Lum, and Metin Sitti. Soft actuators for small-scale robotics. *Advanced materials*, 29(13):1603483, 2017.

[7] Cosimo Della Santina, Christian Duriez, and Daniela Rus. Model-based control of soft robots: A survey of the state of the art and open challenges. *IEEE Control Systems Magazine*, 43(3):30–65, 2023.

[8] Pierre Schegg and Christian Duriez. Review on generic methods for mechanical modeling, simulation and control of soft robots. *Plos one*, 17(1):e0251059, 2022.

[9] Yoonho Kim and Xuanhe Zhao. Magnetic soft materials and robots. *Chemical reviews*, 122(5):5317–5364, 2022.

[10] Narendra Gariya and Pushpendra Kumar. A review on soft materials utilized for the manufacturing of soft robots. *Materials Today: Proceedings*, 46:11177–11181, 2021.

[11] François Schmitt, Olivier Piccin, Laurent Barbé, and Bernard Bayle. Soft robots manufacturing: A review. *Frontiers in Robotics and AI*, 5:84, 2018.

[12] Gianni Stano and Gianluca Percoco. Additive manufacturing aimed to soft robots fabrication: A review. *Extreme Mechanics Letters*, 42:101079, 2021.

[13] Simona Aracri, Francesco Giorgio-Serchi, Giuseppe Suaria, Mohammed E Sayed, Markus P Nemitz, Stephen Mahon, and Adam A Stokes. Soft robots for ocean exploration and offshore operations: A perspective. *Soft Robotics*, 8(6):625–639, 2021.

[14] Pascal Auf der Maur, Betim Djambazi, Yves Haberthür, Patricia Hörmann, Alexander Kübler, Michael Lustenberger, Samuel Sigrist, Oda Vigen, Julian Förster, Florian Achermann, et al. Roboa: Construction and evaluation of a steerable vine robot for search and rescue applications. In *2021 IEEE 4th International Conference on Soft Robotics (RoboSoft)*, pages 15–20. IEEE, 2021.

[15] Tao Wen, Junfeng Hu, Jun Zhang, Xian Li, Sheng Kang, and Ning Zhang. Design, performance analysis, and experiments of a soft robot for rescue. *Journal of Mechanisms and Robotics*, 16(7), 2024.

[16] Min Pan, Chenggang Yuan, Xianrong Liang, Tianyun Dong, Tao Liu, Junhui Zhang, Jun Zou, Huayong Yang, and Chris Bowen. Soft actuators and robotic devices for rehabilitation and assistance. *Advanced Intelligent Systems*, 4(4):2100140, 2022.

[17] Chia-Ye Chu and Rita M Patterson. Soft robotic devices for hand rehabilitation and assistance: a narrative review. *Journal of neuroengineering and rehabilitation*, 15:1–14, 2018.

[18] Ka-Wai Kwok, Helge Wurdemann, Alberto Arezzo, Arianna Menciassi, and Kaspar Althoefer. Soft robot-assisted minimally invasive surgery and interventions: Advances and outlook. *Proceedings of the IEEE*, 110(7):871–892, 2022.

[19] Jiaqi Zhu, Liangxiong Lyu, Yi Xu, Huageng Liang, Xiaoping Zhang, Han Ding, and Zhigang Wu. Intelligent soft surgical robots for next-generation minimally invasive surgery. *Advanced Intelligent Systems*, 3(5):2100011, 2021.

[20] Rajni V Patel, S Farokh Atashzar, and Mahdi Tavakoli. Haptic feedback and force-based teleoperation in surgical robotics. *Proceedings of the IEEE*, 110(7):1012–1027, 2022.

[21] Hesheng Wang, Runxi Zhang, Weidong Chen, Xiaozhou Wang, and Rolf Pfeifer. A cable-driven soft robot surgical system for cardiothoracic endoscopic surgery: preclinical tests in animals. *Surgical endoscopy*, 31:3152–3158, 2017.

[22] Tommaso Ranzani, Matteo Cianchetti, Giada Gerboni, Iris De Falco, and Arianna Menciassi. A soft modular manipulator for minimally invasive surgery: Design and characterization of a single module. *IEEE Transactions on Robotics*, 32(1):187–200, 2016.

[23] Pierre Berthet-Rayne, SM Hadi Sadati, Georgios Petrou, Neel Patel, Stamatia Giannarou, Daniel Richard Leff, and Christos Bergeles. Mammobot: A miniature steerable soft growing robot for early breast cancer detection. *IEEE Robotics and Automation Letters*, 6(3):5056–5063, 2021.

[24] Max McCandless, Alexander Perry, Nicholas DiFilippo, Ashlyn Carroll, Ehab Billatos, and Sheila Russo. A soft robot for peripheral lung cancer diagnosis and therapy. *Soft Robotics*, 9(4):754–766, 2022.

[25] Tomas Amadeo, Daniel Van Lewen, Taylor Janke, Tommaso Ranzani, Anand Devaiah, Urvashi Upadhyay, and Sheila Russo. Soft robotic deployable origami actuators for neurosurgical brain retraction. *Frontiers in Robotics and AI*, 8:731010, 2022.

[26] Luigi Manfredi, Elisabetta Capoccia, Gastone Ciuti, and Alfred Cuschieri. A soft pneumatic inchworm double balloon (spid) for colonoscopy. *Scientific reports*, 9(1):1–9, 2019.

[27] Yu Huan, Xuyang Ren, Andrea Firrincieli, Luigi Manfredi, Matteo Cianchetti, Alberto Arezzo, Edoardo Sinibaldi, and Gastone Ciuti. Flexible over-the-tube device for soft-tethered colonoscopy. *IEEE/ASME Transactions on Mechatronics*, pages 1–11, 2023.

[28] Julius E Bernth, Guokai Zhang, Dionysios Malas, George Abrahams, Bu Hayee, and Hongbin Liu. Morphgi: A self-propelling soft robotic endoscope through morphing shape. *Soft Robotics*, 2024.

[29] Kundong Wang, Jiayi Ma, Feng Wang, Zhiwu Wang, Guozheng Yan, and Yilu Zhou. Full-driving soft robotic colonoscope in compliant colon tissue. *Journal of medical engineering & technology*, 41(8):662–669, 2017.

[30] Lasse Pedersen, Nina Sorensen, Karen Lindorff-Larsen, Charlotte Green Carlsen, Nina Wensel, Christian Torp-Pedersen, and Inge Bernstein. Colonoscopy adverse events: are we getting the full picture? *Scandinavian Journal of Gastroenterology*, 55(8):979–987, 2020.

[31] Matteo Cianchetti, Cecilia Laschi, Arianna Menciassi, and Paolo Dario. Biomedical applications of soft robotics. *Nature Reviews Materials*, 3(6):143–153, 2018.

[32] Tommaso Ranzani, Sheila Russo, F Schwab, Conor J Walsh, and Robert J Wood. Deployable stabilization mechanisms for endoscopic procedures. In *2017 IEEE International Conference on Robotics and Automation (ICRA)*, pages 1125–1131. IEEE, 2017.

[33] Truman Cheng, Xue Zhang, Calvin Sze Hang Ng, Philip Wai Yan Chiu, and Zheng Li. Design and evaluation of a soft-bodied magnetic anchored and guided endoscope. *Journal of Medical Robotics Research*, 3(03n04):1841007, 2018.

[34] Luigi Manfredi, Elisabetta Capoccia, Gastone Ciuti, and Alfred Cuschieri. As oft p neumatic i nchworm d ouble balloon (spid) for colonoscopy. *Scientific reports*, 9(1):1–9, 2019.

[35] Hironori Yamamoto, Christian Ell, Hirito Kita, and Andrea May. Double-balloon endoscopy. *Video Capsule Endoscopy*, pages 113–118, 2014.

[36] Diana Rolniak and Douglas G Adler. Complications of small bowel endoscopy. *Techniques in Gastrointestinal Endoscopy*, 14(2):117–122, 2012.

[37] Satoshi Ohno, Junichi Tachikawa, and Wenwei Yu. Development of a micro mobile robot in the abdominal cavity. In *2009 IEEE/RSJ International Conference on Intelligent Robots and Systems*, pages 4707–4711. IEEE, 2009.

[38] Manuela Eugster, Melanie Oliveira Barros, Philippe C Cattin, and Georg Rauter. Design evaluation of a stabilized, walking endoscope tip. In *International Workshop on Medical and Service Robots*, pages 127–135. Springer, 2020.

[39] Sina Sareh, Kaspar Althoefer, Min Li, Yohan Noh, Francesca Tramacere, Pooya Sareh, Barbara Mazzolai, and Mirko Kovac. Anchoring like octopus: biologically inspired soft artificial sucker. *Journal of the royal society interface*, 14(135):20170395, 2017.

[40] Evan S Dellon, James S Hawk, Ian S Grimm, and Nicholas J Shaheen. The use of carbon dioxide for insufflation during gi endoscopy: a systematic review. *Gastrointestinal endoscopy*, 69(4):843–849, 2009.

[41] WG Mouton, JR Bessell, KT Otten, and GJ Maddern. Pain after laparoscopy. *Surgical endoscopy*, 13(5):445–448, 1999.

[42] Yichao Tang, Qiuting Zhang, Gaojian Lin, and Jie Yin. Switchable adhesion actuator for amphibious climbing soft robot. *Soft robotics*, 5(5):592–600, 2018.

[43] James Walker, Thomas Zidek, Cory Harbel, Sanghyun Yoon, F Sterling Strickland, Srinivas Kumar, and Minchul Shin. Soft robotics: A review of recent developments of pneumatic soft actuators. In *Actuators*, volume 9, page 3. MDPI, 2020.

[44] Zhaoqi Ma and Dan Sameoto. A review of electrically driven soft actuators for soft robotics. *Micromachines*, 13(11):1881, 2022.

[45] Nafiseh Ebrahimi, Chenghao Bi, David J Cappelleri, Gastone Ciuti, Andrew T Conn, Damien Faivre, Neda Habibi, Alexander Hošovskỳ, Veronica Iacovacci, Islam SM Khalil, et al. Magnetic actuation methods in bio/soft robotics. *Advanced Functional Materials*, 31(11):2005137, 2021.

[46] Fei Zhai, Yiyu Feng, Zeyu Li, Yuxin Xie, Jing Ge, Hui Wang, Wei Qiu, and Wei Feng. 4d-printed untethered self-propelling soft robot with tactile perception: Rolling, racing, and exploring. *Matter*, 4(10):3313–3326, 2021.

[47] Tian Chen, Osama R Bilal, Kristina Shea, and Chiara Daraio. Harnessing bistability for directional propulsion of soft, untethered robots. *Proceedings of the National Academy of Sciences*, 115(22):5698–5702, 2018.

[48] Weiqiang Dou, Guoliang Zhong, Jinglin Cao, Zhun Shi, Bowen Peng, and Liangzhong Jiang. Soft robotic manipulators: Designs, actuation, stiffness tuning, and sensing. *Advanced Materials Technologies*, 6(9):2100018, 2021.

[49] George M Whitesides. Soft robotics. *Angewandte Chemie International Edition*, 57(16):4258–4273, 2018.

[50] Matheus S Xavier, Charbel D Tawk, Ali Zolfagharian, Joshua Pinskier, David Howard, Taylor Young, Jiewen Lai, Simon M Harrison, Yuen K Yong, Mahdi Bodaghi, et al. Soft pneumatic actuators: A review of design, fabrication, modeling, sensing, control and applications. *IEEE Access*, 10:59442–59485, 2022.

[51] Dónal P Holland, Evelyn J Park, Panagiotis Polygerinos, Gareth J Bennett, and Conor J Walsh. The soft robotics toolkit: Shared resources for research and design. *Soft Robotics*, 1(3):224–230, 2014.

[52] N Vasios, AJ Gross, S Soifer, JT Overvelde, and K Bertoldi. Harnessing viscous flow to simplify the actuation of fluidic soft robots. soft robot. 7, 1–9, 2018.

[53] Daniel J Preston, Haihui Joy Jiang, Vanessa Sanchez, Philipp Rothemund, Jeff Rawson, Markus P Nemitz, Won-Kyu Lee, Zhigang Suo, Conor J Walsh, and George M Whitesides. A soft ring oscillator. *Science Robotics*, 4(31):eaaw5496, 2019.

[54] Daniel J Preston, Philipp Rothemund, Haihui Joy Jiang, Markus P Nemitz, Jeff Rawson, Zhigang Suo, and George M Whitesides. Digital logic for soft devices. *Proceedings of the National Academy of Sciences*, 116(16):7750–7759, 2019.

[55] Dylan Drotman, Saurabh Jadhav, David Sharp, Christian Chan, and Michael T Tolley. Electronics-free pneumatic circuits for controlling soft-legged robots. science robotics 6, 51 (2021), eaay2627, 2021.

[56] Philipp Rothemund, Alar Ainla, Lee Belding, Daniel J Preston, Sarah Kurihara, Zhigang Suo, and George M Whitesides. A soft, bistable valve for autonomous control of soft actuators. *Science Robotics*, 3(16):eaar7986, 2018.

[57] Stefan Conrad, Joscha Teichmann, Philipp Auth, N Knorr, K Ulrich, D Bellin, Thomas Speck, and Falk J Tauber. 3d-printed digital pneumatic logic for the control of soft robotic actuators. *Science Robotics*, 9(86):eadh4060, 2024.

[58] Yichen Zhai, Albert De Boer, Jiayao Yan, Benjamin Shih, Martin Faber, Joshua Speros, Rohini Gupta, and Michael T Tolley. Desktop fabrication of monolithic soft robotic devices with embedded fluidic control circuits. *Science Robotics*, 8(79):eadg3792, 2023.

[59] Nicholas W Bartlett, Kaitlyn P Becker, and Robert J Wood. A fluidic demultiplexer for controlling large arrays of soft actuators. *Soft matter*, 16(25):5871–5877, 2020.

[60] Shane Hoang, Konstantinos Karydis, Philip Brisk, and William H Grover. A pneumatic random-access memory for controlling soft robots. *Plos one*, 16(7):e0254524, 2021.

[61] Kentaro Kawai, Kenta Arima, Mizuho Morita, and Shuichi Shoji. Microfluidic valve array control system integrating a fluid demultiplexer circuit. *Journal of Micromechanics and Microengineering*, 25(6):065016, 2015.

[62] Saurabh Jadhav, Paul E Glick, Michael Ishida, Christian Chan, Iman Adibnazari, Jurgen P Schulze, Nick Gravish, and Michael T Tolley. Scalable fluidic matrix circuits for controlling large arrays of individually addressable actuators. *Advanced Intelligent Systems*, 5(8):2300011, 2023.

[63] Zhongdong Jiao, Zhenhan Hu, Zeyu Dong, Wei Tang, Huayong Yang, and Jun Zou. Reprogrammable metamaterial processors for soft machines. *Advanced Science*, 11(11):2305501, 2024.

[64] Ryan Scott, Apoorva Kapadia, and Ian Walker. Intuitive interfaces for teleoperation of continuum robots. In *Advances in Human Factors in Robots and Unmanned Systems: Proceedings of the AHFE 2018 International Conference on Human Factors in Robots and Unmanned Systems, July 21-25, 2018, Loews Sapphire Falls Resort at Universal Studios, Orlando, Florida, USA 9*, pages 77–89. Springer, 2019.

[65] Matthew Csencsits, Bryan A Jones, William McMahan, Vikram Iyengar, and Ian D Walker. User interfaces for continuum robot arms. In *2005 IEEE/RSJ International Conference on Intelligent Robots and Systems*, pages 3123–3130. IEEE, 2005.

[66] Chase G Frazelle, Apoorva D Kapadia, Katelyn E Fry, and Ian D Walker. Teleoperation mappings from rigid link robots to their extensible continuum counterparts. In *2016 IEEE International Conference on Robotics and Automation (ICRA)*, pages 4093–4100. IEEE, 2016.

[67] Hyun-Soo Yoon and Byung-Ju Yi. Design of a master device for controlling multi-moduled continuum robots. *Proceedings of the Institution of Mechanical Engineers, Part C: Journal of Mechanical Engineering Science*, 231(10):1921–1931, 2017.

[68] Haitham El-Hussieny, Usman Mehmood, Zain Mehdi, Sang-Goo Jeong, Muhammad Usman, Elliot W. Hawkes, Allison M. Okarnura, and Jee-Hwan Ryu. Development and evaluation of an intuitive flexible interface for teleoperating soft growing robots. In *2018 IEEE/RSJ International Conference on Intelligent Robots and Systems (IROS)*, pages 4995–5002, 2018.

[69] Chase G Frazelle, Apoorva D Kapadia, and Ian D Walker. A haptic continuum interface for the teleoperation of extensible continuum manipulators. *IEEE Robotics and Automation Letters*, 5(2):1875–1882, 2020.

[70] Gastone Ciuti, Karolina Skonieczna-Żydecka, Wojciech Marlicz, Veronica Iacovacci, Hongbin Liu, Danail Stoyanov, Alberto Arezzo, Marcello Chiurazzi, Ervin Toth, Henrik Thorlacius, et al. Frontiers of robotic colonoscopy: a comprehensive review of robotic colonoscopes and technologies. *Journal of clinical medicine*, 9(6):1648, 2020.

[71] Peiqi Wang, Tim Xu, Saowanee Ngamruengphong, Martin A Makary, Anthony Kalloo, and Susan Hutfless. Rates of infection after colonoscopy and osophagogastroduodenoscopy in ambulatory surgery centres in the usa. *Gut*, 67(9):1626–1636, 2018.

[72] Arjo J Loeve, Paul Fockens, and Paul Breedveld. Mechanical analysis of insertion problems and pain during colonoscopy: why highly skill-dependent colonoscopy routines are necessary in the first place... and how they may be avoided. *Canadian Journal of Gastroenterology*, 27(5):293–302, 2013.

[73] Moshe Shike, Zvi Fireman, Rami Eliakim, Ori Segol, Alan Sloyer, Lawrence B Cohen, Sharon Goldfarb-Albak, and Alessandro Repici. Sightline colonosight system for a disposable, power-assisted, non-fiber-optic colonoscopy (with video). *Gastrointestinal endoscopy*, 68(4):701–710, 2008.

[74] Shabana F Pasha, M Edwyn Harrison, Ananya Das, Carolyn M Corrado, Kristine N Arnell, and Jonathan A Leighton. Utility of double-balloon colonoscopy for completion of colon examination after incomplete colonoscopy with conventional colonoscope. *Gastrointestinal endoscopy*, 65(6):848–853, 2007.

[75] Robertson Alexander R, Koulaouzidis Anastasios, Yung Diana E, Fraser Christopher, Nemeth Artur, Trimble Kenneth, Toth Ervin, Plevris John N, and Wurm Johansson Gabriele. Balloon-assisted colonoscopy after incomplete conventional colonoscopy—experience from two european centres with a comprehensive review of the literature. *Journal of Clinical Medicine*, 9(9):2981, 2020.

[76] Gavriel Iddan, Gavriel Meron, Arkady Glukhovsky, and Paul Swain. Wireless capsule endoscopy. *Nature*, 405(6785):417–417, 2000.

[77] Jonathan Belsey, Cristiano Crosta, Owen Epstein, Wolfgang Fischbach, Peter Layer, Fabrizio Parente, and Marc Halphen. Meta-analysis: efficacy of small bowel preparation for small bowel video capsule endoscopy. *Current medical research and opinion*, 28(12):1883–1890, 2012.

[78] Ana-Maria Singeap, Carol Stanciu, and Anca Trifan. Capsule endoscopy: the road ahead. *World journal of gastroenterology*, 22(1):369, 2016.

[79] James W Martin, Bruno Scaglioni, Joseph C Norton, Venkataraman Subramanian, Alberto Arezzo, Keith L Obstein, and Pietro Valdastri. Enabling the future of colonoscopy with intelligent and autonomous magnetic manipulation. *Nature machine intelligence*, 2(10):595–606, 2020.

[80] Federico Bianchi, Gastone Ciuti, Anastasios Koulaouzidis, Alberto Arezzo, Danail Stoyanov, Sebastian Schostek, Calogero Maria Oddo, Arianna Menciassi, and Paolo Dario. An innovative robotic platform for magnetically-driven painless colonoscopy. *Annals of translational medicine*, 5(21), 2017.

[81] Laura H Blumenschein, Margaret M Coad, David A Haggerty, Allison M Okamura, and Elliot W Hawkes. Design, modeling, control, and application of everting vine robots. *Frontiers in Robotics and AI*, 7:548266, 2020.

[82] David A Haggerty, Nicholas D Naclerio, and Elliot W Hawkes. Characterizing environmental interactions for soft growing robots. In *2019 IEEE/RSJ International Conference on Intelligent Robots and Systems (IROS)*, pages 3335–3342. IEEE, 2019.

[83] Joseph D Greer, Tania K Morimoto, Allison M Okamura, and Elliot W Hawkes. A soft, steerable continuum robot that grows via tip extension. *Soft robotics*, 6(1):95–108, 2019.

[84] Nicholas D Naclerio and Elliot W Hawkes. Simple, low-hysteresis, foldable, fabric pneumatic artificial muscle. *IEEE Robotics and Automation Letters*, 5(2):3406–3413, 2020.

[85] Alexander M Kübler, Sebastián Urdaneta Rivera, Frances B Raphael, Julian Förster, Roland Siegwart, and Allison M Okamura. A multi-segment, soft growing robot with selective steering. In *2023 IEEE International Conference on Soft Robotics (RoboSoft)*, pages 1–7. IEEE, 2023.

[86] David A Haggerty, Nicholas D Naclerio, and Elliot W Hawkes. Hybrid vine robot with internal steering-reeling mechanism enhances system-level capabilities. *IEEE Robotics and Automation Letters*, 6(3):5437–5444, 2021.

[87] Margaret M Coad, Laura H Blumenschein, Sadie Cutler, Javier A Reyna Zepeda, Nicholas D Naclerio, Haitham El-Hussieny, Usman Mehmood, Jee-Hwan Ryu, Elliot W Hawkes, and Allison M Okamura. Vine robots: Design, teleoperation, and deployment for navigation and exploration. *IEEE Robotics & Automation Magazine*, 27(3):120–132, 2019.

[88] Laura H Blumenschein, Allison M Okamura, and Elliot W Hawkes. Modeling of bioinspired apical extension in a soft robot. In *Conference on Biomimetic and Biohybrid Systems*, pages 522–531. Springer, 2017.

[89] Xinyi Pi, Isabella A Szczech, and Lin Cao. A retractable soft growing robot with a flexible backbone. In *2023 IEEE/RSJ International Conference on Intelligent Robots and Systems (IROS)*, pages 2477–2484. IEEE, 2023.

[90] Margaret M Coad, Rachel P Thomasson, Laura H Blumenschein, Nathan S Usevitch, Elliot W Hawkes, and Allison M Okamura. Retraction of soft growing robots without buckling. *IEEE Robotics and Automation Letters*, 5(2):2115–2122, 2020.

[91] Nam Gyun Kim, Dongoh Seo, Shinwoo Park, and Jee-Hwan Ryu. Self-retractable soft growing robots for reliable and fast retraction while preserving their inherent advantages. *IEEE Robotics and Automation Letters*, 2023.

[92] William E. Heap, Nicholas D. Naclerio, Margaret M. Coad, Sang-Goo Jeong, and Elliot W. Hawkes. Soft retraction device and internal camera mount for everting vine robots. In *2021 IEEE/RSJ International Conference on Intelligent Robots and Systems (IROS)*, pages 4982–4988, 2021.

[93] Pellegrino Crafa and Salvador J Diaz-Cano. Changes in colonic structure and mucosal inflammation. In *Colonic Diverticular Disease*, pages 41–61. Springer, 2022.

[94] Tomoya Takahashi, Masahiro Watanabe, Kenjiro Tadakuma, Masashi Konyo, and Satoshi Tadokoro. Retraction mechanism of soft torus robot with a hydrostatic skeleton. *IEEE Robotics and Automation Letters*, 5(4):6900–6907, 2020.

[95] A Alazmani, A Hood, D Jayne, A Neville, and P Culmer. Quantitative assessment of colorectal morphology: Implications for robotic colonoscopy. *Medical engineering & physics*, 38(2):148–154, 2016.

[96] Elliot W. Hawkes, David L. Christensen, and Allison M. Okamura. Design and implementation of a 300In *2016 IEEE International Conference on Robotics and Automation (ICRA)*, pages 4022–4029, 2016.

[97] Liu Xiaomin, Wang Yiqiang, Geng Dexu, Zhang Jintao, and Zhao Yunwei. Mechanical characteristics analysis on pam with elongation and torsion. In *2011 International Conference on Mechatronic Science, Electric Engineering and Computer (MEC)*, pages 613–616. IEEE, 2011.

[98] Alan N Gent. On the relation between indentation hardness and young's modulus. *Rubber Chemistry and Technology*, 31(4):896–906, 1958.

[99] Robert J Webster III and Bryan A Jones. Design and kinematic modeling of constant curvature continuum robots: A review. *The International Journal of Robotics Research*, 29(13):1661–1683, 2010.

[100] Michael A Bell, Kaitlyn P Becker, and Robert J Wood. Injection molding of soft robots. *Advanced Materials Technologies*, 7(1):2100605, 2022.

[101] Vishy Mahadevan. Anatomy of the caecum, appendix and colon. *Surgery (Oxford)*, 38(1):1–6, 2020.

[102] Herbert F Helander and Lars Fändriks. Surface area of the digestive tract–revisited. *Scandinavian journal of gastroenterology*, 49(6):681–689, 2014.

[103] Slawomir Wozniak, Aleksander Pawlus, Joanna Grzelak, Slawomir Chobotow, Friedrich Paulsen, Cyprian Olchowy, and Urszula Zaleska-Dorobisz. Acute colonic flexures: the basis for developing an artificial intelligence-based tool for predicting the course of colonoscopy. *Anatomical Science International*, 98(1):136–142, 2023.

[104] ZM Xue, CG Wang, JT Kang, and HF Tan. Buckling analysis of an inflated arch including wrinkling based on pseudo curved beam model. *Thin-Walled Structures*, 131:336–346, 2018.

[105] Yang Liu and Farshid Alambeigi. Impact of generic tendon routing on tension loss of tendon-driven continuum manipulators with planar deformation. *IEEE Robotics and Automation Letters*, 7(2):3624–3631, 2022.

[106] Dezheng Hua, Xinhua Liu, He Lu, Shuaishuai Sun, Miguel Angel Sotelo, Zhixiong Li, and Weihua Li. Design, fabrication, and testing of a novel ferrofluid soft capsule robot. *IEEE/ASME Transactions on Mechatronics*, 27(3):1403–1413, 2021.

[107] Sinan Sadalla, Andrea Lisotti, Lorenzo Fuccio, and Pietro Fusaroli. Colonoscopy-related colonic ischemia. *World Journal of Gastroenterology*, 27(42):7299, 2021.

[108] Behnam Bahr, Yingjie Li, and Mahmoud Najafi. Design and suction cup analysis of a wall climbing robot. *Computers & electrical engineering*, 22(3):193–209, 1996.

[109] Yu Yoshida and Shugen Ma. Design of a wall-climbing robot with passive suction cups. In *2010 IEEE International Conference on Robotics and Biomimetics*, pages 1513–1518. IEEE, 2010.

[110] Haruna Iwasaki, Flavien Lefevre, Dana D Damian, Eiji Iwase, and Shuhei Miyashita. Autonomous and reversible adhesion using elastomeric suction cups for in-vivo medical treatments. *IEEE Robotics and Automation Letters*, 5(2):2015–2022, 2020.

[111] Anastasia Koivikko, Dirk-Michael Drotlef, Metin Sitti, and Veikko Sariola. Magnetically switchable soft suction grippers. *Extreme Mechanics Letters*, 44:101263, 2021.

[112] Sukho Song, Dirk-Michael Drotlef, Donghoon Son, Anastasia Koivikko, and Metin Sitti. Adaptive self-sealing suction-based soft robotic gripper. *Advanced science*, 8(17):2100641, 2021.

[113] Dingxin Ge, Takahiro Matsuno, Yi Sun, Chao Ren, Yongchen Tang, and Shugen Ma. Quantitative study on the attachment and detachment of a passive suction cup. *Vacuum*, 116:13–20, 2015.

[114] M Follador, F Tramacere, and B Mazzolai. Dielectric elastomer actuators for octopus inspired suction cups. *Bioinspiration & biomimetics*, 9(4):046002, 2014.

[115] S-M Kirsch, F Welsch, M Schmidt, P Motzki, and S Seelecke. Bistable sma vacuum suction cup. In *ACTUATOR 2018; 16th International Conference on New Actuators*, pages 1–4. VDE, 2018.

[116] Peilin Cheng, Yuze Ye, Jiangming Jia, Chuanyu Wu, and Qizhi Xie. Design of cylindrical soft vacuum actuator for soft robots. *Smart Materials and Structures*, 30(4):045020, 2021.

[117] Zhenishbek Zhakypov, Florian Heremans, Aude Billard, and Jamie Paik. An origami-inspired reconfigurable suction gripper for picking objects with variable shape and size. *IEEE Robotics and Automation Letters*, 3(4):2894–2901, 2018.

[118] Abhishek Bamotra, Pushpinder Walia, Avataram Venkatavaradan Prituja, and Hongliang Ren. Fabrication and characterization of novel soft compliant robotic end-effectors with negative pressure and mechanical advantages. In *2018 3rd International Conference on Advanced Robotics and Mechatronics (ICARM)*, pages 369–374. IEEE, 2018.

[119] Enguang Guan, Yunhao Ge, Jihao Liu, Weixin Yan, and Yanzheng Zhao. Piezoelectric micro-pump suction cup design and research on the optimal static driving characteristics. In *International Conference on Intelligent Robotics and Applications*, pages 26–38. Springer, 2017.

[120] H Tsukagoshi and Y Osada. Soft hybrid suction cup capable of sticking to various objects and environments. actuators 2021, 10, 50, 2021.

[121] Jessica A Sandoval, Saurabh Jadhav, Haocheng Quan, Dimitri D Deheyn, and Michael T Tolley. Reversible adhesion to rough surfaces both in and out of water, inspired by the clingfish suction disc. *Bioinspiration & biomimetics*, 14(6):066016, 2019.

[122] Moon Kee Choi, Ok Kyu Park, Changsoon Choi, Shutao Qiao, Roozbeh Ghaffari, Jaemin Kim, Dong Jun Lee, Myungbin Kim, Wonji Hyun, Seok Joo Kim, et al. Cephalopod-inspired miniaturized suction cups for smart medical skin. *Advanced healthcare materials*, 5(1):80–87, 2016.

[123] Charbel Tawk and Gursel Alici. Finite element modeling in the design process of 3d printed pneumatic soft actuators and sensors. *Robotics*, 9(3):52, 2020.

[124] Daniel Steck, Jian Qu, S Baghbani Kordmahale, Daniel Tscharnuter, Anastasia Muliana, and Jun Kameoka. Mechanical responses of ecoflex silicone rubber: Compressible and incompressible behaviors. *Journal of Applied Polymer Science*, 136(5):47025, 2019.

[125] Young-Doo Kwon, Soon-Bum Kwon, Xiaozhe Lu, and Hyun-Wook Kwon. A finite element procedure with poisson iteration method adopting pattern approach technique for near-incompressible rubber problems. *Advances in Mechanical Engineering*, 6:272574, 2014.

[126] Kevin Lister, Zhan Gao, and Jaydev P Desai. Development of in vivo constitutive models for liver: Application to surgical simulation. *Annals of biomedical engineering*, 39(3):1060–1073, 2011.

[127] Jessica L Sparks, Nicholas A Vavalle, Krysten E Kasting, Benjamin Long, Martin L Tanaka, Phillip A Sanger, Karen Schnell, and Teresa A Conner-Kerr. Use of silicone materials to simulate tissue biomechanics as related to deep tissue injury. *Advances in skin & wound care*, 28(2):59–68, 2015.

[128] Anzhu Gao, Ning Liu, Mali Shen, Mohamed EMK Abdelaziz, Burak Temelkuran, and Guang-Zhong Yang. Laser-profiled continuum robot with integrated tension sensing for simultaneous shape and tip force estimation. *Soft Robotics*, 7(4):421–443, 2020.

[129] Ziwen Wang, Teng Wang, Baoliang Zhao, Yucheng He, Ying Hu, Bing Li, Peng Zhang, and Max Q-H Meng. Hybrid adaptive control strategy for continuum surgical robot under external load. *IEEE Robotics and Automation Letters*, 6(2):1407–1414, 2021.

[130] Yahya Elsayed, Augusto Vincensi, Constantina Lekakou, Tao Geng, CM Saaj, Tommaso Ranzani, Matteo Cianchetti, and Arianna Menciassi. Finite element analysis and design optimization of a pneumatically actuating silicone module for robotic surgery applications. *Soft Robotics*, 1(4):255–262, 2014.

[131] Kai Luo, Philipp Rothemund, George M Whitesides, and Zhigang Suo. Soft kink valves. *Journal of the Mechanics and Physics of Solids*, 131:230–239, 2019.

[132] Claudio Bustos, Claudio García Herrera, Diego Celentano, Daming Chen, and Marcela Cruchaga. Numerical simulation and experimental validation of the inflation test of latex balloons. *Latin American Journal of Solids and Structures*, 13(14):2657–2678, 2016.

[133] Jinyan Chen, Jianlin Yang, Feng Qian, Qing Lu, Yu Guo, Zhijun Sun, and Chao Chen. A novel inchworm-inspired soft robotic colonoscope based on a rubber bellows. *Micromachines*, 13(4):635, 2022.

[134] Graham Robinson and J Bruce C Davies. Continuum robots-a state of the art. In *Proceedings 1999 IEEE international conference on robotics and automation (Cat. No. 99CH36288C)*, volume 4, pages 2849–2854. IEEE, 1999.

[135] Jessica Burgner-Kahrs, D Caleb Rucker, and Howie Choset. Continuum robots for medical applications: A survey. *IEEE Transactions on Robotics*, 31(6):1261–1280, 2015.

[136] Ryan Scott, Apoorva Kapadia, and Ian Walker. Intuitive interfaces for teleoperation of continuum robots. In *International Conference on Applied Human Factors and Ergonomics*, pages 77–89. Springer, 2018.

[137] Mariangela Manti, Vito Cacucciolo, and Matteo Cianchetti. Stiffening in soft robotics: A review of the state of the art. *IEEE Robotics Automation Magazine*, 23(3):93–106, 2016.

[138] Igor Zubrycki and Grzegorz Granosik. Novel haptic glove-based interface using jamming principle. In *2015 10th International Workshop on Robot Motion and Control (RoMoCo)*, pages 46–51, 2015.

[139] Saurabh Jadhav, Mohamad Ramzi Abdul Majit, Benjamin Shih, Jürgen P Schulze, and Michael T Tolley. Variable stiffness devices using fiber jamming for application in soft robotics and wearable haptics. *Soft Robotics*, 9(1):173–186, 2022.

[140] Igor Zubrycki and Grzegorz Granosik. Novel haptic device using jamming principle for providing kinaesthetic feedback in glove-based control interface. *Journal of Intelligent & Robotic Systems*, 85(3):413–429, 2017.

[141] Margherita Brancadoro, Mariangela Manti, Selene Tognarelli, and Matteo Cianchetti. Fiber jamming transition as a stiffening mechanism for soft robotics. *Soft robotics*, 7(6):663–674, 2020.

[142] Gregor Harih and Bojan Dolšak. Comparison of subjective comfort ratings between anatomically shaped and cylindrical handles. *Applied ergonomics*, 45(4):943–954, 2014.

[143] Robert J Webster III and Bryan A Jones. Design and kinematic modeling of constant curvature continuum robots: A review. *The International Journal of Robotics Research*, 29(13):1661–1683, 2010.

[144] Tatsuho Nagatomo and Norihisa Miki. Three-axis capacitive force sensor with liquid metal electrodes for endoscopic palpation. *Micro & Nano Letters*, 12(8):564–568, 2017.

[145] Kenneth Salisbury, David Brock, Thomas Massie, Nick Swarup, and Craig Zilles. Haptic rendering: Programming touch interaction with virtual objects. In *Proceedings of the 1995 symposium on Interactive 3D graphics*, pages 123–130, 1995.

[146] Assaf Pressman, Leah J Welty, Amir Karniel, and Ferdinando A Mussa-Ivaldi. Perception of delayed stiffness. *The International Journal of Robotics Research*, 26(11-12):1191–1203, 2007.

[147] Netta Gurari, Katherine J Kuchenbecker, and Allison M Okamura. Perception of springs with visual and proprioceptive motion cues: Implications for prosthetics. *IEEE Transactions on Human-Machine Systems*, 43(1):102–114, 2012.

[148] George A Gescheider. *Psychophysics: the fundamentals*. Psychology Press, 2013.

[149] Lynette A Jones and Hong Z Tan. Application of psychophysical techniques to haptic research. *IEEE transactions on haptics*, 6(3):268–284, 2012.

[150] I Fründ, N V Haenel, and F A Wichmann. Inference for psychometric functions in the presence of nonstationary behavior. *Journal of Vision*, 11(6), May 2011.

[151] Pete R Jones. A note on detecting statistical outliers in psychophysical data. *Attention, Perception, & Psychophysics*, 81(5):1189–1196, 2019.

[152] Peter J Rousseeuw and Christophe Croux. Alternatives to the median absolute deviation. *Journal of the American Statistical association*, 88(424):1273–1283, 1993.

[153] Wouter M Bergmann Tiest and Astrid ML Kappers. Cues for haptic perception of compliance. *IEEE transactions on haptics*, 2(4):189–199, 2009.

[154] Lynette A Jones and Ian W Hunter. A perceptual analysis of stiffness. *Experimental Brain Research*, 79(1):150–156, 1990.

[155] John G Kreifeldt and Ming-Chuen Chuang. Moment of inertia: Psychophysical study of an overlooked sensation. *Science*, 206(4418):588–590, 1979.

[156] HE Ross and AJ Benson. The weber fraction for moment of inertia. *Fechner Day*, 86:71–76, 1986.

[157] Shingo Kawano, Motohiro Kojima, Yoichi Higuchi, Motokazu Sugimoto, Koji Ikeda, Naoki Sakuyama, Shinichiro Takahashi, Ryuichi Hayashi, Atsushi Ochiai, and Norio Saito. Assessment of elasticity of colorectal cancer tissue, clinical utility, pathological and phenotypical relevance. *Cancer science*, 106(9):1232–1239, 2015.

[158] Pier Paolo Mainenti, Delfina Iodice, Sabrina Segreto, Giovanni Storto, Mario Magliulo, Giovanni Domenico De Palma, Marco Salvatore, and Leonardo Pace. Colorectal cancer and 18fdg-pet/ct: what about adding the t to the n parameter in loco-regional staging? *World Journal of Gastroenterology: WJG*, 17(11):1427, 2011.